LA-UR -90-1996

TITLE: SHOCK WAVES IN CONDENSED MEDIA: THEIR PROPERTIES AND THE
EQUATIONS OF STATE OF MATERIALS DERIVED FROM THEM

AUTHOR(S): R. G. MCQUEEN, M-6

MASTER

Los Alamos
Los Alamos National Laboratory
Los Alamos, New Mexico 87545

SHOCK WAVES IN CONDENSED MEDIA:
THEIR PROPERTIES AND THE EQUATION OF STATE
OF MATERIALS DERIVED FROM THEM

I. INTRODUCTION

It was almost a half century ago that shock waves were first used to obtain equation-of-state (EOS) data for solids at pressures over 10 GPa. To my knowledge the first work was done at the Los Alamos National Laboratory and probably concurrently by the Russians. Heretofore, the impetus for studying the EOS at what were then considered ultra-high pressures, was mostly for scientific reasons with perhaps some thought for some high-pressure alchemy. With the development of atomic weapons, such research became imperative. The basic conservation equations for shock properties had been developed just over 100 years ago, so the first experimenters knew what to expect if they could make the appropriate measurements. The fact that this paper is being written attests to their success.

To provide an overall perspective and some understanding of what is involved in the shock-wave process, we first develop the basic conservation equations and some hydrodynamic flow properties that affect the experimental measurements. These are almost entirely restricted to one-dimensional plane flow, which is quite appropriate because almost all EOS data are obtained in a similar situation. The bulk of the thermodynamics needed for calculations to supplement the EOS data, or to calculate other thermodynamic quantities, such as the specific heat, when additional data are obtained, is presented next. Phase changes and elastic-plastic flow are then considered. A limited set of experimental techniques is given next, with one or two examples of typical records or results. These types of experiments are of primary importance in understanding the state of matter at high pressure. Because of a certain unique property of the shock-wave EOS of solids, a short section is devoted to the consequences of its properties followed by brief summaries of the results of many experiments. Finally, we consider the shock-wave EOS of the earth, undoubtedly the largest shock-wave recovery laboratory we have, which after a lot of study by seismologists, has revealed quite a bit about itself. On the basis of that work and some results presented here, an EOS for the earth is derived.

It should be realized that many of the examples used to illustrate certain features or properties have been taken from Los Alamos data or publications primarily because this was least difficult to me. I regret that it was not convenient to use as examples more

1

of the excellent work reported by other investigators especially in the Soviet Union. The bibliography is somewhat limited but should be adequate as a beginning point for the casual reader.

TABLE OF CONTENTS

The following notation is used throughout the text.

H – Hugoniot refers to states on the Hugoniot; sometimes used as subscript

U_s – Shock-wave velocity

U_d – Driver-plate velocity

U_p – Particle velocity behind the shock wave

U_r – Particle velocity due to the rarefaction wave

U_{fs} – Free-surface velocity $= U_p + U_r$

X – Eulerian space coordinate

x – Lagrangian space coordinate

t – Time

P – Pressure

V – Specific volume

ρ – Density

E – Specific internal energy

S – Entropy

P'_s – Slope of the isentrope $\partial P / \partial V\,]_s$

P'_H – Slope of the Hugoniot $\partial P / \partial V\,|_H$

K_s – Isentropic bulk modulus $= -V P'_s$

C – Sound velocity $= \partial P / \partial \rho)_s^{1/2}$

s – Slope of the U_s-U_p data fits

q – Quadratic coefficient of the U_s-U_p data fits

L – Lagrangian sound velocity

II. ISENTROPIC FLOW AND SHOCK WAVES

The developments in the next sections are based on the assumption that the material being studied is subjected to a plane one-dimensional shock and that any subsequent mo-

4

tion is also of that nature. Moreover, it is assumed that the material is in thermodynamic equilibrium and free from any anisotropic stresses. The former assumption presents no conceptual problems, nor does the latter when considering materials in the liquid state. However, when a plane shock passes through a solid, it is obvious that the lattice cannot deform in one dimension only (a few exceptions will be mentioned later), as it will develop tremendous shear stresses. The lattice comes to equilibrium by motion, on the microscale through dislocation motion resulting in slip-twinning and/or other mechanisms. How close it comes to an equilibrium state has not been well studied at high pressures because of the experimental difficulties. There appears to be sufficient evidence to believe the residual stresses are small compared to the pressures involved. This residual stress is called the deviatoric stress, and when it is zero the Hugoniot is often referred to as the equilibrium Hugoniot or sometimes the hydrostat. The problems associated with the one-dimensional nature of the experiments are classified as elastic-plastic and will be discussed briefly later.

In this section we shall first develop the governing equations for continuous flow, and then the shock-wave conservation equations. Although we are interested primarily in shock waves, there are a few other concepts immersed in the development for continuous flow that we will require later.

A. The Conservation Equations for Continuous Flow

The flow equations were developed by Euler in 1755. In addition to formulating the equation of motion for fluid flow from Newton's laws, he introduced the concept of the conservation of mass. A few hundred years ago compressible flow was limited to gases, so it was convenient and logical to think of flow through tubes or the equivalent. Instead of watching a particular mass element, we watch the material flow through a section of pipe of uniform unit cross section, $A = 1$ as shown in Fig. II.1. The length of the tube is ΔX, the material enters at X and comes out at $X + \Delta X$. The mass entering from the left in unit time dt is the density times the velocity

5

$$\Delta X$$

$$\rho + \frac{\partial \rho}{\partial X}\Delta X \ dt$$

$$A\rho \ U \ dt$$

$$U + \frac{\partial U}{\partial X}\Delta Xdt$$

$$X \qquad\qquad X + \Delta X$$
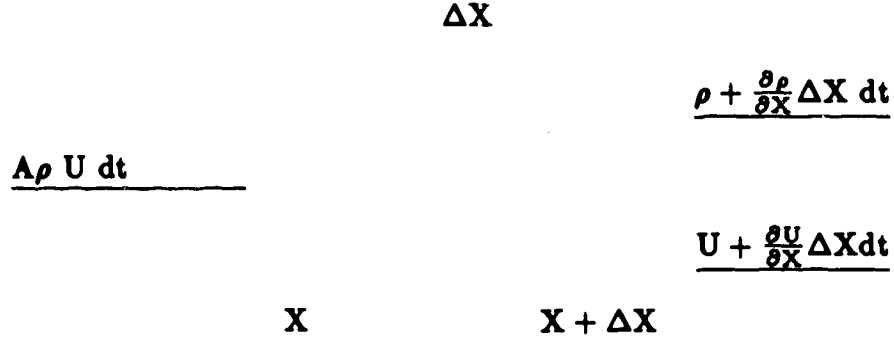
Figure II.1

As the material passes through the tube, both its velocity and its density can change, so the material leaving from the right in unit time is

$$A\left[\rho U + \left(\rho \frac{\partial U}{\partial X} + U\frac{\partial \rho}{\partial X}\right)dX\right]dt \quad ,$$

where higher order terms have been dropped. If the mass out and mass in are not equal, the density in the cylinder must be changing. The change in mass per unit time is expressed by

$$A\frac{\partial \rho}{\partial t}\Delta Xdt \quad ,$$

which must equal the difference between the flux in and out:

$$\frac{\partial \rho}{\partial t}\Delta Xdt = \rho Udt - (\rho U)dt - \rho\frac{\partial U}{\partial V}dXdt - U\frac{\partial \rho}{\partial X}dXdt \tag{II.1}$$

or

$$\frac{\partial \rho}{\partial t} = -\rho\frac{\partial U}{\partial X} - U\frac{\partial \rho}{\partial X} = -\frac{\partial(U\rho)}{\partial X} \quad . \tag{II.2}$$

This is the equation of conservation of mass in one-dimensional continuous flow.

The equation of motion is derived similarly (Fig. II.2). The force on the left minus the force on the right gives the difference, $-(\partial P/\partial X)\Delta X$, which is the force to the right operating on the mass in the element $\rho\Delta X$.

$$\Delta X$$

$$\underline{P(X)} \quad\quad\quad\quad \underline{P(X) + \frac{\partial P}{\partial X}}$$

$$X \quad\quad\quad\quad X + \Delta X$$
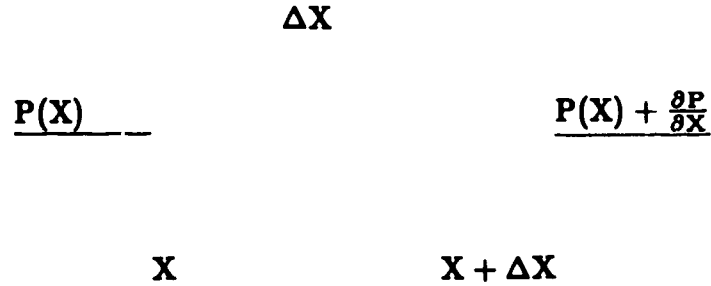
Figure II.2

The acceleration is

$$\frac{dU}{dt} = U\frac{\partial U}{\partial X} + \frac{\partial U}{\partial t} \quad , \tag{II.3}$$

so from Newton's second law,

$$-\frac{\partial P}{\partial X}\Delta X = \rho\Delta X\left(\frac{dU}{at}\right) \tag{II.4}$$

or

$$-\frac{\partial P}{\partial X} = \rho\frac{\partial U}{\partial t} + \rho U\frac{\partial U}{\partial X} \tag{II.5}$$

gives the equation of motion in Eulerian form.

For one-dimensional flow it is particularly useful to develop the conservation equations by watching a particular mass element, the Lagrangian system, rather than watching the material streaming by a fixed reference point, the Eulerian form. Here and later, we are following the treatment given by von Mises [1958].

7

$$\Delta X$$

t $\rho(t)$

$\underline{\quad X \quad}$ $\underline{X + \Delta X}$

$t + \Delta t$ $\rho(\cdot + \Delta t)$

$\underline{X + U(X)\Delta t}$ $\underline{X + \Delta X + U(X + \Delta X)\Delta t}$

Figure II.3

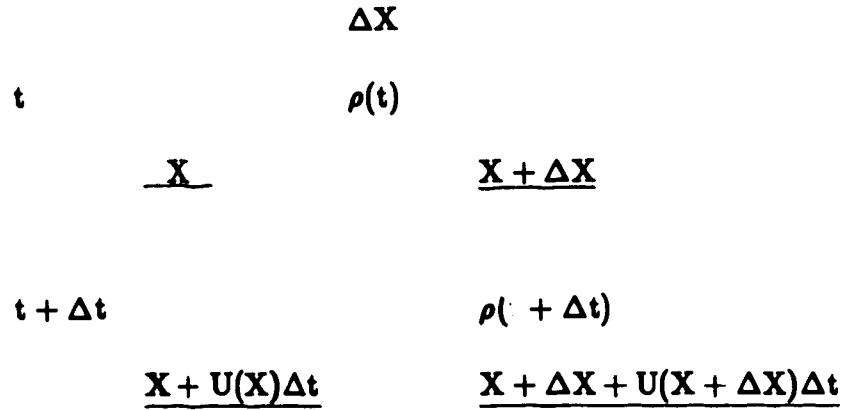Here ρ is the density, X the space coordinate, and U the material velocity. Since the mass is the product of the area A, density, and thickness and is constant in time, then

$$A\rho(t)\Delta X = A\rho(t + \Delta t)\{\Delta X + [U(X + \Delta X) - U(X)]\Delta t\} \quad , \tag{II.6}$$

which becomes after rewriting,

$$\frac{\rho(t) - \rho(t + \Delta t)}{\Delta t} = \frac{\rho(t + \Delta t)[U(X + \Delta X) - U(X)]}{\Delta X} \quad . \tag{II.7}$$

As $\Delta t \to 0$ and $\Delta X \to 0$, the differential form of the conservation of mass is obtained:

$$\frac{d\rho}{dt} = -\rho\frac{\partial U}{\partial X} \quad . \tag{II.8}$$

The equation of motion is obtained by equating the time rate of change of momentum, UM, of the mass element to the force on it. In the figure below,
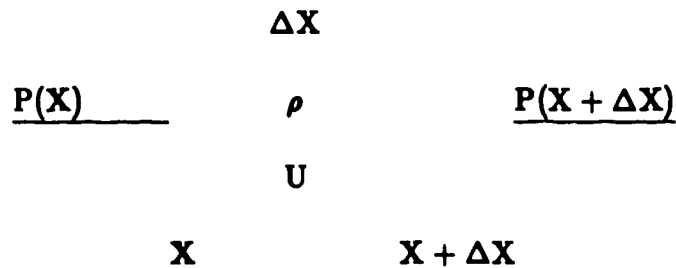
$$\Delta X$$

$\underline{P(X) \quad\quad}$ ρ $\underline{P(X + \Delta X)}$

U

X $X + \Delta X$

Figure II.4

8

P is the pressure, and from Newton's law, we have

$$-A[P(X + \Delta X) - P(X)] = \frac{d(UM)}{dt} = A\rho\Delta X\frac{dU}{dt} \quad . \tag{II.9}$$

Rewriting and taking the limit gives the differential form of the equation of motion,

$$\rho\frac{dU}{dt} = -\frac{\partial P}{\partial X} \quad . \tag{II.10}$$

The equation for the conservation of energy can be determined as before by considering the power input per unit area, $\underline{UP}(X)$ or $U(X)P(X)$, into the mass element.

$$\Delta X$$

$$\rho$$

$$\underline{UP(X)} \qquad U^2/2 \qquad \underline{UP(X + \Delta X)}$$

$$E$$

$$X \qquad X + \Delta X$$
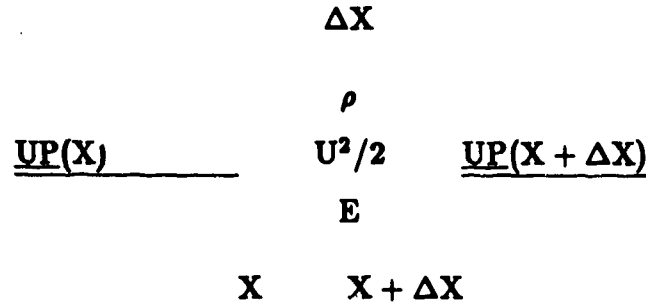
Figure II.5.

Here E represents the specific internal energy per gram and $U^2/2$ the kinetic energy per gram. Then the time rate of change of energy of the mass, M, is

$$A\rho\Delta X(d/dt)(E + U^2/2) = A[\underline{UP}(X) - \underline{UP}(X + \Delta X)] \quad , \tag{II.11}$$

which becomes

$$\rho\frac{d}{dt}\left(E + \frac{U^2}{2}\right) = \frac{-\partial(\underline{UP})}{\partial X}. \quad . \tag{II.12}$$

Expanding the right-hand side of Eq. (II.12) and substituting from Eqs. (II.8) and (II.10), we have

$$P\frac{\partial U}{\partial X} + U\frac{\partial P}{\partial X} = \frac{P}{\rho}\frac{d\rho}{dt} - \rho U\frac{dU}{dt} \quad , \tag{II.13}$$

which when replaced in Eq. (II.12) gives the conservation for the internal energy

$$\frac{dE}{dt} = \frac{P}{\rho^2}\frac{d\rho}{dt} \quad . \tag{II.14}$$

9

If ρ^{-1} is replaced by the specific volume, V, Eq. (II.14) becomes

$$\frac{dE}{dt} = -P\frac{dV}{dt} \quad . \tag{II.15}$$

It is important to note that the energy equation cannot be used to determine the flow, as this equation can actually be derived from the other conservation equations. The question arises as to the usefulness of the energy conservation law. The answer, of course, is that it tells us that the flow formulated here must be isentropic, since Eq. (II.15) is the time derivative of the first law of thermodynamics with $dS = 0$. However, for shock waves it is well known that the entropy increases, so some mechanism must be introduced to allow it to do so. Thus a stress, σ_x, is defined, which is the viscous force in the direction of propagation acting on a unit area of surface normal to that direction. The total stress σ is defined by

$$\sigma = P - \sigma_x \quad , \tag{II.16}$$

where P is still the pressure associated with the equation of state. It is reasonable to believe that what is needed is a force that resists rapid deformation. For the problem considered, the deformation rate is dp/dt, so we assume that

$$\sigma_x \sim dp/dt \quad , \tag{II.17}$$

which can be rewritten by use of the conservation of mass as

$$\sigma_x = \mu(\partial U/\partial X) \quad . \tag{II.18}$$

This puts the stress in the usual form of a velocity-gradient dependent variable, with μ, the ordinary coefficient of viscosity, as the factor of proportionality. The previous conservation equations are rigorous; but the only justification for equation (II.18) is that something is needed, and it seems to serve well.

Now P must be replaced in the conservation equations by σ. The conservation of mass, Eq. (II.7), is not changed but the equation of motion, Eq. (II.9), becomes

$$\rho\frac{dU}{dt} = \frac{\partial P}{\partial X} + \mu\frac{\partial^2 U}{\partial X^2} \quad . \tag{II.19}$$

Since we are interested in the internal energy, the same substitution is made in Eq. (II.14), obtaining

$$\frac{dE}{dt} = \frac{P}{\rho^2}\frac{d\rho}{dt} - \frac{\mu}{\rho^2}\frac{\partial U}{\partial X}\frac{d\rho}{dt} \quad , \tag{II.20}$$

10

which from Eqs. (II.15) and (II.8) gives

$$\frac{dE}{dt} = -P\frac{dV}{dt} + \frac{\mu}{\rho}\left(\frac{\partial U}{\partial X}\right)^2 \quad . \tag{II.21}$$

This is the desired form. If μ is chosen to be positive, then the second term on the right-hand side of the previous equation is positive and hence always increases the internal energy.

B. Characteristics

When the flow consists only of a simple rarefaction wave, the problem is readily solved by the method of characteristics. To put the equations into a form suitable for this type of solution, we first substitute the sound speed, $C^2 = (\partial P/\partial\rho)_s$, into Eq. (II.10) to obtain

$$\rho U_t = C^2(\rho/\rho_o)\rho_x \quad , \tag{II.22}$$

where the subscripts here and elsewhere represent partial differentiation with respect to that variable. The coefficient (ρ/ρ_o) represents the current thickness. Multiplying Eq. (II.8) by an undetermined parameter λ and adding and subtracting Eq. (II.22) gives the following equations:

$$\lambda\rho_t + C^2(\rho/\rho_o)\rho_x + \rho U_t + \lambda\rho(\rho/\rho_o)U_x = 0 \tag{II.23}$$

and

$$\lambda\rho_t - C^2(\rho/\rho_o)\rho_x - \rho U_t + \lambda\rho(\rho/\rho_o)U_x = 0 \quad . \tag{II.24}$$

To put the equations in the desired form we require that $\lambda = C$. The equations then become

$$C[\rho_t + C(\rho/\rho_o)\rho_x] + \rho[U_t + C(\rho/\rho_o)U_x] = 0 \tag{II.25}$$

and

$$C[\rho_t - C(\rho/\rho_o)\rho_x] - \rho[U_t + C(\rho/\rho_o)U_x] = 0 \quad . \tag{II.26}$$

Since in general for any function $F(x,t)$, $dF = F_x dx + F_t dt$, Eq. (II.25) implies that

$$C\,d\rho = -\rho\,dU \text{ along } dx/dt = C(\rho/\rho_o) \tag{II.27}$$

and Eq. (II.26) implies that

$$C\,d\rho = \rho\,dU \text{ along } dx/dt = -C(\rho/\rho_o) \quad . \tag{II.28}$$

11

The left-hand pair of equations in Eqs. (II.27) and (II.28) are called the characteristic equations from which velocities can be calculated, and the right-hand pair are called characteristics. When the flow is adjacent to a region of constant state, the flow is described as a simple wave and one set of characteristics is straight lines.

The above results are quite important, as the concepts and equations can be used to solve a class of problems that occur frequently — in fact, must occur in some form or other — in shock-wave experiments or related phenomena. These are pressure-release waves called simple centered waves. To illustrate this type of flow problem, consider what happens if a thin plate driver collides with a somewhat thicker plate target. For this example the plates need not be made of the same material, but it simplifies the illustration if they are. At some time the shock in the driver will reach the back surface of the target and sometime later, because of the configuration, the shock in the other plate will reach the front surface of the target plate. When either shock reaches the free surface, the pressure will drop to zero, if done in a vacuum, and a pressure release wave will propagate back into the material. A schematic of this effect is illustrated in Fig. I.6. We note first that the two shock waves labeled S are drawn as straight lines, because the materials are uniform in all respects. At the time when the shock reaches the free surface there are drawn two straight lines headed in the opposite direction. From the previous development the upper of these rays are linear with a slope.

$$\frac{dx}{dt} = \pm C(\rho/\rho_o) = \pm C^L \quad . \tag{II.29}$$

Here C is the local velocity of sound at that pressure, and ρ/ρ_o represents the shorter path length in the compressed material. In the figure no compression is indicated and represents the system in Lagrangian coordinates. C^L in the previous equation is called the Lagrangian sound velocity. These straight lines are called the lead characteristics and their slope is governed by the state of the material behind the shock wave and its EOS. There is a second ray drawn, its shape is governed by the state of the material at zero pressure, if there is no other material in the system. From the geometry it can be seen that at some reference point or line on the x axis (the dashed line), the time from the first characteristic to cross the line to the next continues to increase with time. This means that the rarefaction release wave becomes less steep or disperses as it goes through the material. Thus, as shocks become steep as they develop rarefaction waves spread out in time. There is a characteristic for any point between the two drawn, and with a little arithmetic the actual shape of the release wave can easily be calculated. Its shape depends on the geometry and the EOS. Where the characteristics cross, the pressure at the head

of the waves decreases, and as drawn will develop into a tension wave. The interaction of the two rarefaction waves are not simple centered waves and the flow is more tedious to calculate.

From the above we see how we could calculate pressures and densities in the rarefaction zone, but there is an additional quantity that can be calculated in a straightforward manner; that is the material velocity in the zone. Returning to the characteristic Eq. (II.28), integrating along the characteristic gives

$$U = \int C \frac{d\rho}{\rho} \tag{II.30}$$

and after substituting $(dP/\partial\rho)^{1/2}$ for C gives the material velocity increase between any states:

$$U = \int_{P_1}^{P_2} \left|\frac{\partial P}{\partial \rho}\right|_s^{1/2} = \int_{P_1}^{P_2} -\left(\frac{\partial V}{\partial P}\right)_s^{1/2} dP \quad . \tag{II.31}$$

When the integral is evaluated between the shock state pressure and zero pressure the velocity is called the rarefaction velocity, U_r.

Although we stated that we would restrict these lectures to one-dimensional flow, we are always faced problems associated with the finite size of the samples used in the experiments. This can usually be handled by making the lateral dimensions of the samples much larger than the thickness. This of course is wasteful and it is desirable to design experiments so that the samples be investigated can be as thick as possible for the space available. Fortunately, the position where lateral flow perturbs the one-dimensional nature of the flow can easily be found by using characteristics just describe if some EOS properties of the material are known.

Imagine a rectangular block of material impacted on one face by a flat plate. A plane-shock wave will propagate upward from the interface and at the same time a rarefaction wave will propagate into the sample from the edge. The problem to be solved is to find the locus of points where a rarefaction wave from the side interacts with the shock wave traveling through a sample.

Since the sample has been shocked the head of the rarefaction wave will propagate at the local sound velocity C. There will be curve equivalent to the lead characteristic just discussed, and since it is moving into a region of constant state it will be linear. In Fig. II.7 we have a sample of thickness, Y and we are going to locate the distance, X, that

13

the rarefaction wave has gone into the sample. T is the time for the shock wave to reach the top of the sample and is given by

$$T = Y/U_s \quad . \tag{II.32}$$

If we define the hypoteneus of the little rectangle by H we have

$$H^2 = X^2 + Y_2^2 \quad . \tag{II.33}$$

At time T the sample has been compressed to a thickness $Y_2 = Y \cdot \rho_o/\rho$ and the length of H is $T \cdot C$. After making the appropriate substitutions II.33 becomes

$$\left(\frac{Y}{U_s} \cdot C\right)^2 = X^2 + \left(Y\frac{\rho_o}{\rho}\right)^2 \quad . \tag{II.34}$$

Since the angle given by X/Y is what we are interested in we have

$$\left(\frac{X}{Y}\right) = \left[\left(\frac{C}{U_s}\right)^2 - \left(\frac{\rho_o}{\rho}\right)^2\right]^{1/2} \quad . \tag{II.35}$$

The question might be asked what good is Eq. (II.35) if we do not know the sound velocity or the compression. The answer is that the designer will soon know what kind of compression will be associated with the various experiments, but what is more important we have found that the bulk sound velocity is very nearly equal to the shock velocity, which means that the angle is approximately a function only of the compression. The above approximation is for the bulk sound velocity. However, for solids the head of the rarefaction wave travels at the longitudinal sound velocity so the C/U_s ratio should be replaced by the ratio, C_L/C_B. This ratio can be found from ultrasonic measurements at $P = 0$ and since it changes very slowly with pressure it can also be considered constant for this application.

It would appear that one could use (II.35) to determine C by measuring the X/Y ratio. This has been attempted but the results have been disappointing, because the leading wave travels at the longitudinal velocity, C_L, but its amplitude is relatively small and it is difficult to detect its arrival precisely, but it is large enough to make the velocity of the bulk wave difficult to measure. The arrivals of these waves do not have sharp well-defined break, but rather appear as curves that blend into the flat section of the unattenuated shock wave. I feel that this technique for measuring sound velocities behind the shock front deserves further development.

C. The Shock Wave Conservation Equations

14

It was recognized in the second half of the 19th century that the conservation equations as derived were not adequate for all types of flow. In 1869 Rankine [1] showed that there was no steady adiabatic process in which pressure forces alone could describe the changes from one constant state to another by a continuous change. He proposed that the process be adiabatic in that the systems receive no external heat, but that on the microscale, or locally, heat could be exchanged. This agrees with the principle of the conservation of energy. However, Hugoniot in 1887 [2] was the first to correctly describe the relationship of energy and entropy involved in continuous and discontinuous flow. He showed that ideal continuous flow implied conservation of entropy, and that an increase in entropy must occur across a shock. From the above he described the conservation of energy relationship as ordinarily seen.

Before developing the conservation relations it might be useful to review some of the history involved in making EOS measurements. To our knowledge, the first reports of this work were published in 1955 by Goranson, Bancroft, Burton, Blechar, Houston, Gittings, and Landeen [3], Walsh and Christian [4], Minshall [5], and Mallory [6]. By using various explosives in contact with metal plates, they increased the pressure range to almost 500 kbar in dense materials like copper. The Los Alamos group reported on shock-wave data for 27 metallic elements in 1957 [7]. However, even earlier, Shreffler and Deal [8] had shown that high explosives could accelerate thin metal plates to high velocities, but it was several years before these rapidly moving plates were used as drivers to produce measured strong shock waves in other materials. In 1958 Al'tshuler, Vrupnikov, Ledenen, Zhuchikhin, and Brazhnik [9] reported extensive data on iron to shock pressure of about 5 mbar. The Soviet investigators [10] subsequently reported data for eight metallic elements to about the same pressure. They extended the pressure to about 9 Mbar in 1962 [11]. McQueen and Marsh [12] reported data for nineteen elements in 1960. Explosively-driven metal plates were used to generate the high pressures in the latter experiments [9–12]. The initial high pressure is obviously produced by the collision, but the following high pressure is regarded as a direct result of shock waves formed. Again we will limit the discussion to plane one-dimensional flow, a situation easily obtainable in the experiments simply by making the lateral dimensions of the plates large compared to the thickness of the material under investigation. In the impact experiments, the shock front would initially be infinitely steep if the surfaces were perfectly flat and parallel. It would then rapidly disperse to its equilibrium shape, which for a hydrodynamic material is probably less than a few nanometers thick for a strong shock. For the present, we assume that the shock front is steady and reasonably steep. The experiment can then be described

schematically as in Fig. II.8, where U_d and U_s are subject to measurement.

To proceed further, we note that if the driver and target are the same material and in the same thermodynamic state, then symmetry requires that the particle velocity after the shock be exactly half the driver velocity:

$$U_p = U_d/2 \quad .$$

(II.36)

By use of the conservation of mass, momentum, and energy, the compression, pressure, and energy behind a shock wave can be expressed in terms of initial conditions and the measured shock-wave and material velocities. These relationships are usually obtained by considering the flow through a stationary shock front; however, it is probably more informative to develop the conservation equations more or less directly from the experimental geometry. Figure II.7 represents schematically a thin plate of thickness, d, moving with velocity, U_d, that collides with a stationary target plate at time zero. The desired relations can be obtained by considering the configuration at collision time and at some later time, t, after the material has been shocked. For convenience t is chosen as the time when the shock wave has just propagated through the driver, or

$$t = d/U_s \quad .$$

(II.37)

No loss in generality has occurred, since the thickness of the driver is arbitrary. As shown, the target must be at least as thick as the driver. During time t the back side of the driver moves a distance

$$\Delta X = tU_d \quad ,$$

(II.38)

so the compression can be written

$$\frac{V_o - V}{V} = \frac{\Delta X}{2d} = \frac{tU_d}{2tU_s} = \frac{U_p}{U_s}$$

(II.39)

as a direct consequence of the conservation of mass. The conservation of momentum requires that the force, $(P - P_o)A$, (A is cross-sectional area) must be equal to the time rate of change of momentum, $d(MU_p)/dt$. In time, t, the mass, $\rho_o Ad$, suffers a change in velocity, U_p; hence

$$A(P - P_0) = (\rho_o Ad)U_p/t \quad \text{or} \quad P - P_o = \rho_o U_p U_s \quad .$$

(II.40)

16

The sum of the changes in the internal energy, $2(E-E_o)\rho_o Ad$, and kinetic energy, $(U_p^2 - U)$, must be equal to any external work, $P_0(AtU_d)$, done on the system during the passage of the shock wave.

$$2(E - E_0)\rho_o Ad + (U_p^2 - U_d^2/2)poAd = P_0(AtU_d) \quad . \tag{II.41}$$

After making appropriate substitutions, we can see that the increase in the specific internal energy arising from the shock wave is

$$E - E_0 = U_p^2/2 + P_0 V_0 U_p/U_s \quad . \tag{II.42}$$

Equations (II.39) and (II.40) can be combined to give

$$U_s = V_0[(P - P_0)/(V_0 - V)]^{1/2} \tag{II.43}$$

and

$$U_p = [(P - P_0)(V_0 - V)]^{1/2} \quad . \tag{II.44}$$

Substitution of Eqs. (II.43) and (II.44) in Eq. (II.42) gives the well-known Hugoniot energy equation

$$E - E_0 = (P + P_0)(V_0 - V)/2 \quad . \tag{II.45}$$

For a given steady-state shock wave all the quantities $(P, V, E, U_p, U_s,)$ are defined. The locus of any pair of these parameters is called the Hugoniot curve in the corresponding plane, or often simply the Hugoniot.

In this development the usual restrictions of steady-state flow and hydrostatic equilibrium are required. The effect of material rigidity will be discussed later. If the shape of the shock front is not independent of time, several difficulties arise. One is that a true shock-wave velocity can not be measured; the apparent measured velocity is dependent on what part (amplitude) of the wave is used to determine a transit time (see Fig. II.9). Even more serious, it is usually considered that the steady-state assumption necessary for deriving the shock-wave relationships is no longer valid. However, this is really of no great consequence, since if by some quirk of nature the EOS of the material were such that the pressure wave dispersed with time, there simply would be no shock wave to worry about. The low-pressure EOS of fused quartz is of this nature. The thermodynamic states and velocity distributions must be known in order to set up the conservation relationships that

17

previously were quite simple. Unpublished data of Taylor and Rice indicate that steady-state shocks exist for some solid materials at pressures as low as 5 GPa. This helps to establish the validity of high-pressure shock-wave data since shock fronts tend to become more stable at higher pressures.

C. Comparing Isentropes and Hugoniots

We have just derived the conservation relationships for shock waves, but we have not demonstrated mathematically that shock waves even exist. To do so, we compare the consequences of the similar set of equations for continuous flow, where the dimensions of interest are large compared to the microstructure of the material of interest, e.g., the lattice parameters of a solid or the particle size of a heterogeneous mixture. The concept of continuous flow implies the lack of discontinuities, such as the shock waves just discussed. As before, the equation of motion is simply based on Newton's laws of motion, but the continuity equation is developed by considering the flow through a small volume element, as is usually done for shock waves. For our applications the flow can be described by one space dimension, which of course implies that areas involved in the experiment are free from influences from edges, e.g., the central region of an impactor on a sabot accelerated in some kind of gun. In the following we restrict ourselves to two types of flow or compression, isentropic and shock compression. Isentropic compression can be envisioned by considering a piston moving slowly in a thermally-insulated cylinder and compressing a gas, for example. Here the temperature will increase, but the process is done at constant entropy with no heat flow. The resulting P-V relationship is called an isentrope. If the system were operated in such a manner that the temperature remained constant, the resulting curve would be designated as an isotherm; most static compression data are obtained isothermally. From other flow relationships it appears that the shock or Hugoniot EOS and isentropic EOS are quite similar, both being adiabatic (no heat flow). For this and later work we will need to refer to the mathematical statement of the first law of thermodynamics:

$$dE = TdS - PdV \quad . \tag{II.48}$$

In the following we will compare the two EOSs for a normal material. The pressure on an isentrope for a normal material increases with compression or heating

$$\partial P/\partial V|_s < 0 \tag{II.49}$$

$$\partial \Gamma/\partial S|_v > 0 \tag{II.50}$$

18

and $\partial P / \partial V|_s$ becomes stiffer with increasing compression

$$\partial^2 P / \partial V^2|_s > 0 \quad . \tag{II.51}$$

We have seen from the conservation equations that the Hugoniot and isentrope differ only in the entropy. To examine this difference more closely we will differentiate the Hugoniot energy Eq. (II.45) with respect to volume and substitute the appropriate differentials in mathematical formulation of the first laws, Eq. (II.48):

$$T \frac{dS}{dV} = \frac{dE}{dV} + P \quad , \tag{II.52}$$

where the terms are written as total differentials since we are evaluating them along the Hugoniot. The differentials are:

$$\frac{dE}{dV} = \frac{(V_o - V)}{2} \frac{dP}{dV} - \frac{(P + P_o)}{2} \quad , \tag{II.53}$$

$$\frac{d^2E}{dV^2} = \frac{(V_o - V)}{2} \frac{d^2P}{dV^2} - \frac{dP}{dV} \quad , \tag{II.54}$$

and

$$\frac{d^3E}{dV^3} = \frac{(V_o - V)}{2} \frac{d^3P}{dV^3} - \frac{d^2P}{dV^2} \quad . \tag{II.55}$$

Substituting Eq. (II.53) in Eq. (II.52) and further differentiation gives the following equation:

$$\frac{TdS}{dV} = \frac{(V_o - V)}{2} \frac{dP}{dV} + \frac{1}{2}(P - P_o) \tag{II.56}$$

$$T \frac{d^2S}{dV^2} + \frac{dT}{dV} \frac{dS}{dV} = \frac{d^2E}{dV^2} + \frac{dP}{dV} = \frac{(V_o - V)}{2} \frac{d^2P}{dV^2} \tag{II.57}$$

$$\frac{d^2T}{dV^2} \frac{dS}{dV} + \frac{dT}{dV} \frac{d^2S}{dV^2} + \frac{dT}{dV} \frac{d^2S}{dV^2} + T \frac{d^3S}{dV^3} = \frac{(V_o - V)}{2} \frac{d^3P}{dV^3} - \frac{1}{2} \frac{d^2P}{dV^2} \tag{II.58}$$

or

$$T \frac{d^3S}{dV} + 2 \frac{dT}{dV} \frac{d^2S}{dV^2} + \frac{d^2T}{dV^2} \frac{dS}{dV} = \frac{(V_o - V)}{2} \frac{d^3P}{dV^3} - \frac{1}{2} \frac{d^2P}{dV^2} \quad . \tag{II.59}$$

At the beginning of the Hugoniot, where $P = P_o$ and $V = V_o$, the equations simplify to the following:

$$T \frac{dS}{dV} = 0 \quad , \tag{II.60}$$

$$T \frac{d^2S}{dV^2} = 0 \quad , \tag{II.61}$$

19

and

$$\tau \frac{d^3S}{dV^3} = -\frac{1}{2}\frac{d^2P}{dV^2} \quad . \tag{II.62}$$

This shows that the entropy increase on the Hugoniot is of third order. However, if the change in entropy is zero for second-order increase in shock strength, it implies that the isentrope and Hugoniot have the same first and second pressure-volume derivatives at the initial state. To see this, take the pressure derivative on the Hugoniot and differentiate again, giving

$$\frac{dP}{dV} = \left.\frac{\partial P}{\partial V}\right|_S + \left.\frac{\partial P}{\partial S}\right|_V \frac{dS}{dV} \tag{II.63}$$

$$\frac{d^2P}{dV^2} = \left.\frac{\partial^2 P}{\partial V^2}\right|_S + \left.\frac{\partial P}{\partial V}\right|_S \left.\frac{\partial P}{\partial S}\right|_V \frac{dS}{dV} \tag{II.64}$$

$$+\left.\frac{\partial P}{\partial S}\right|_V \left.\frac{\partial P}{\partial V}\right|_S \frac{dS}{dV} + \left.\frac{\partial P}{\partial S}\right|_V \frac{dS}{dV}\frac{dS}{dV} + \frac{\partial P}{\partial S}\frac{d^2S}{dV^2}$$

$$\frac{d^2P}{dV^2} = \left.\frac{\partial^2 P}{\partial V^2}\right|_S + 2\frac{\partial^2 P}{\partial VS}\frac{dS}{dV} + \left.\frac{\partial^2 P}{\partial S^2}\right|\left(\frac{dS}{dV}\right)^2 + \frac{\partial P}{\partial S}\frac{d^2S}{dV^2} \quad . \tag{II.65}$$

At the initial point, using the previous results, we obtain the very important relationships

$$\left.\frac{dP}{dV}\right|_H = \left.\frac{\partial P}{\partial V}\right|_S \tag{II.66}$$

and

$$\left.\frac{d^2P}{dV^2}\right|_H = \left.\frac{\partial^2 P}{\partial V^2}\right|_S \quad . \tag{II.67}$$

Thus, not only is the slope of the Hugoniot the same as that of the isentrope, meaning that the zero-pressure shock velocity is the same as the ultrasonic sound velocity, but their next derivatives are also the same. One other important relationship is needed, namely, the sound velocity or the slope of an isentrope, $\partial P/\partial V]_S$, at $P \neq 0$ with respect to the Hugoniot. To find this we will need the thermodynamic Grüneisen parameter,

$$\gamma = V(\partial P/\partial E)_V \quad . \tag{II.68}$$

As indicated, γ is assumed to be only a function of volume, and for some applications it is assumed to satisfy the relationship

$$\rho\gamma = \rho_o\gamma_o \quad . \tag{II.69}$$

Additional discussion of γ and C_V are given in later sections. What is required is to relate the energy on the Hugoniot, $E_H(V)$, which is determined by the density, to an energy state

off the Hugoniot. Here we are interested in the velocity of sound, which propagates at constant entropy, so we need to prescribe an $E(V, S)$ equation of state. We will relate the difference in energy between these states (at the same density) with the energy calculated from the difference in pressure and γ. From the definition of γ (II.68) we have

$$E_H - E = (P_H - P)\left(\frac{V}{\gamma}\right) \quad . \tag{II.70}$$

This gives, on differentiation,

$$\frac{dE}{dV}\bigg|_H = \frac{\partial E}{\partial V}\bigg|_s + (P_H - P)\frac{d(V/\gamma)}{dV} + \left(\frac{dP_H}{dV} - \frac{\partial P}{\partial V}\right)\left(\frac{V}{\gamma}\right) \quad . \tag{II.71}$$

We also need the differential of the Hugoniot Eq. (II.45):

$$\frac{dE}{dV}\bigg|_H = \frac{(V_o - V)}{2}\frac{dP}{dV}\bigg|_H - \frac{(P_o + P_H)}{2} \quad . \tag{II.72}$$

Equating (II.71) and (II.72) and solving for the slope of the isentrope gives

$$\frac{\partial P}{\partial V}\bigg|_s = \frac{\gamma}{V}\left[\frac{\partial E}{\partial V}\bigg|_s + (P_H - P)\frac{d(V/\gamma)}{dV} + \frac{V}{\gamma}\frac{dP_H}{dV} - \frac{(V_o - V)}{2}\frac{dP_H}{dV} + \frac{(P_o + P_H)}{2}\right] \quad . \tag{II.73}$$

After simplifying and using

$$\frac{\partial E}{\partial V}\bigg|_s = -P \quad . \tag{II.74}$$

Equation (II.73), we find from the slope along an isentrope

$$\frac{\partial P}{\partial V}\bigg|_s = \left[1 - \left(\frac{\gamma}{V}\right)\frac{(V_o - V)}{2}\right]\frac{dP_H}{dV} + \frac{\gamma}{V}\frac{(P_o + P_H)}{2} + \frac{\gamma}{V}(P_H - P)\frac{d(V/\gamma)}{dV} \quad . \tag{II.75}$$

It can be seen that when $P_H = P$ the first two terms give the slope of the isentrope where it crosses the Hugoniot. The last term then gives the change in slope for states above or below the Hugoniot.

As a matter of interest it is appropriate to note the analogs for the velocity of sound

$$C = -V(\partial P/\partial V)^{1/2} \tag{II.76}$$

with the velocity of a shock wave Eq. (II.43) and the corresponding equations for the material velocity on a rarefaction wave Eq. (II.31) and the material velocity due to a shock wave Eq. (II.44).

III. SUPPLEMENTAL HUGONIOT CALCULATIONS

In this section we will outline several calculational procedures for extending the EOS to regions off the Hugoniot, mainly by calculating reflected shocks and pressure-release isentropes. We will also show how other thermodynamic quantities, such as temperature and entropy, can be calculated, so that reasonable estimates of these quantities can be made. The equations are also inverted, so that quantities like the Grüncisen parameter or specific heat can *be* calculated if sound velocities and/or temperatures have been measured. Almost all the calculations are done by stepwise integration or iterational methods. Sometimes both are necessary. This causes no hardships, since one is usually creating tables or graphs. Temperatures can readily be calculated in flow problems with only a slight increase in computer time. If appropriate, some examples are given. It should be kept in mind that gamma and the specific heat usually are considered functions of volume only, because of our ignorance and theoretical considerations. This restriction does not have to be imposed on the numerical methods, but the thermodynamic variables must be internally consistent.

A. Reflected Shocks and Isentropes

A problem that frequently arises in shock-wave physics is to find the state that a shock-loaded material goes to when the shock waves passes through it and into a different material placed on it. To find the solution to this problem one uses the pressure-particle velocity Hugoniots of the materials of interest. In Fig. III.1 are plotted three Hugoniots with the center one representing the material through which the shock traverses first. The Hugoniot of the second material could either lie above or below the first material. Although there are some objections to the term "shock impedance" the term is often used to describe states in the pressure-particle velocity plane. Thus the upper curve is said to have a higher shock impedance than the other two, or that they have a lower shock impedance. The origin of the term comes from the conservation of moment equation (II.38), $P = \rho_o U_s U_p$, where the product $\rho_o U_s$ compared to the similar terms ρC in ultrasonics. The product is also used to define stiffness but that term is more appropriately restricted to U_s or C itself.

The materials were in contact before and after the passage of the shock wave. This means that they have the same particle velocity, and continuity also requires that the pressure in both material at the interface be the same. Since the particle velocity and pressure at the interface must be the same, a graphical or numerical solution for this

requirement in the pressure particle-velocity plane yields the new states (see Fig. III.1). The states in the samples are reached by what are called reflected shocks when the pressure in the samples are higher, or pressure release states or isentropes when the pressure in the samples are lower.

To calculate the reflected shock states and isentropic release states, one must use energy equation, the Hugoniot of the material shocked first, and its Grüneisen parameter, γ, defined as

$$\gamma = V(dP/dE)_V \quad .$$ (III.1)

Various forms of the previous equation are used in what has been called the Mie Grüneisen EOS. As defined, γ can be used in a general energy equation for relating processes and energies at any point to corresponding values on the Hugoniot, or

$$E = E_H + (P - P_H)/\rho\gamma \quad .$$ (III.2)

Reflected shock loci are calculated in the P-V plane. The difference in energy between a single-shocked state and a double-shocked state is illustrated in Fig. III.2. Using that difference and the indicated pressure difference, the locus of second shock states can be calculated by III.2. The following is the equation for calculating reflected shocks, obtained by satisfying the energy conditions along the two Hugoniots:

$$P_2 = \frac{P_H - (\rho\gamma)_2[(P_H - P_1)(V_o - V_2)/2]}{1 - (\rho\gamma)_2(V_1 - V_2)/2} \quad .$$ (III.3)

Even though it is known that rigidity effects are present in most shock flow problems, they are ignored when calculating release states, as they were when making the reflected shock calculations. In that case release states are assumed to be isentropic and can be calculated via the thermodynamic law

$$dE = TdS - PdV$$ (III.4)

with $dS = 0$. Using the nomenclature in Fig. III.3, the following difference equation can be obtained to calculate the P-V loci of the isentropes.

$$Pi = \frac{P_H - (\rho\gamma)_i[P_{i-1}\Delta V/2 + E_H - E_{i-1}]}{1 + (\rho\gamma)_i\Delta V/2}$$ (III.5)

Using the same nomenclature, a modified form of the Riemann equation,

$$\Delta U_r = \sqrt{-\Delta V \Delta P} \quad ,$$ (III.6)

23

where ΔU_r is the incremental increase in the material velocity, is easily evaluated at the same time as the PV locus is determined. Although it is difficult to compress solids isentropically to very high pressure, Eqs. III.5 and III.6 can be solved for increasing or decreasing pressure conditions.

B. Recentered Hugoniots

On occasion it is desirable to calculate the locus of a Hugoniot that was centered at some other state; perhaps the material was heated or the sample had some porosity. This can be done in the same manner as calculating reflected shock states for use in impedance-match calculations. Gamma has been used to calculate the effect of porosity on the density-pressure loci of shocked materials. This was first demonstrated in 1964 [13]. Subsequently, porous materials have been used by several experimenters in an attempt to obtain gamma. With reference to Fig. III.4, the energy difference at the shocked volume state V between a Hugoniot based on a crystal density material, V_x, and one shocked from a porous state, V_o, is shown by the slashed area. The average value of gamma is

$$\bar{\gamma} = V(P_o - P_x)/[P_x(V_x - V) - P_o(V_o - V)] \quad . \tag{III.7}$$

Here all values are taken along the Hugoniots and the o subscript refers to the originally porous material. It is assumed here that the specific internal energies of the crystalline and porous materials are the same. The addition of an energy term in the denominator allows temperature corrections to be made.

To correct a Hugoniot data set obtained with porous samples, (III.7) is inverted, giving

$$P_x = P_o[\bar{\gamma}(V_o - V) + 2V]/[\gamma(V_x - V) + 2V] \quad . \tag{III.8}$$

The Los Alamos group [12,14] calculated γ from the Dugdale MacDonald [15] relationship

$$\gamma = \frac{V}{2}\left(\frac{d^2(PV^{2/3})/dV^2}{d(PV^{2/3})dV}\right) - \frac{1}{3} \quad . \tag{III.9}$$

However, it is common to use the relationship

$$\gamma = \gamma_o(\rho_o\rho)^q \quad . \tag{III.10}$$

There seems to be no justification for using more complicated functional forms at the present time. Further discussion of the Grüneisen parameter will be given later.

24

C. Temperature and Other Thermodynamic Considerations

Temperatures are usually not measured in shock-wave experiments, but knowledge of the temperature of the shock state is of considerable interest. For example, many rate processes are strongly temperature dependent; studies of the interior of the earth involve temperature as well as compressibility, and composition and phase boundaries are best described in the P-T plane. It thus behooves us to discuss methods for calculating temperature. If temperatures are measured, the equations can be modified so specific heats can be calculated at least to the uncertainties in the Grüneisen parameter. In addition to the relationships discussed previously, the thermodynamic identity

$$TdS = C_v dT + T(\partial P/\partial T)_V dV \quad , \tag{III.11}$$

where

$$(\partial P/\partial T)_V = C_v(\gamma/V) \tag{III.12}$$

is used. Here C_v is the specific heat at constant volume. Substituting the value of dE from the Grüneisen equation (II.67) in the thermodynamic law (II.46) gives the following relationship:

$$TdS = (V_o - V)dP/2 + (P - P_o)dV/2 \quad . \tag{III.13}$$

Eliminating TdS from (III.11) and (III.13) above gives the differential equation

$$dT = (V_o - V)dP/2C_v + [(P - P_o)/2C_v - T(\gamma/V)]dV \quad . \tag{III.14}$$

It was shown by Wackerle [16] that although this equation can be integrated in closed form for some special cases, it is undoubtedly more convenient to solve this equation by using a centered difference equation. One we have used is

$$T_i = \frac{T_{i-1}[1 - \bar{\rho}\bar{\gamma}\Delta V/2] + [(V_o - \bar{V})\Delta P + (\bar{P} - P_o)\Delta V]/2\bar{C}_v}{1 + \bar{\rho}\bar{\gamma}\Delta V/2} \quad . \tag{III.15}$$

The origin of the various terms is explained in Fig. III.5. When using this difference equation, any form of the Hugoniot, Grüneisen parameter, and specific heat, can be used as long as they are compatible. If the temperature is assumed known at some point on the Hugoniot, the previous equation can be integrated either up or down in pressure. The specific heat used in temperature calculations varies, from a simple constant 3R value to a value calcula d from the Debye theory with electronic contributions. The latter term certainly is very important for metals at high temperatures. If dS = 0 (isentropes) then the thermodynamic identity (III.11) becomes

$$dT = -T(\gamma/V)dV \quad , \tag{III.16}$$

25

which can be readily integrated:

$$T = T_l \exp \left[- \int_{V_l}^{V} (\gamma/V) dV \right] \quad . \tag{III.17}$$

Temperatures along isentropes have been calculated with III.17 using initial values along the $P = 0$ isobar. It might appear that doing so would eliminate errors caused by uncertainties in the specific heat. However, these same types of uncertainties are reflected in the assumption that γ is a function of volume only. Equation III.12 has been used, again with the reservation that the variable is only a function of volume, to calculate isotherms from isentropes or Hugoniot temperature loci simply because more complex functions are not justified. The ΔP term in (III.12) is often described as the thermal pressure.

Equation III.13 can also be used to calculate the entropy in a similar manner. A difference equation we have used is

$$S_l = S_{l-1} + \left[\Delta P(V_o - \bar{V}) + \Delta V(\bar{P} - P_o) \right]/2T \quad . \tag{III.18}$$

D. The Method of Mixtures

The need sometimes arises to know the Hugoniot of a material that is a mixture of other materials whose Hugoniots are known. It would be advantageous if the Hugoniot of the composite could be calculated rather than measured. We feel that this can be done reasonably well, at least in some instances. Before proceeding further we wish to specify what mixtures should be amenable to calculation. First, the components should not interact with each other. This would exclude such things as alloys and compounds, for there is nothing in the simple calculations to be described that can account for changes in the microstructure or electronic structures that can effect compressibility and other such things. However, if nothing better can be done, the method could still be useful. At least some properties of the new state can be incorporated. The calculations are based on equilibrium thermodynamic conditions, which means that the particle size should be such that thermal equilibrium can be obtained on the time scale of the experiments. However, even this may be too restrictive, since the total energy is properly accounted for and variations in the temperature distribution will average out through the thermal expansion of the components.

Mixtures occur frequently in geological materials; rocks are probably the most abundant, and in a sense more of a true mixture without chemical interactions, as opposed to

iron-nickel meteorites, in which some alloying occurs. Some minerals such as forsterite and enstatite, whose chemical formulas may be written as sums of basic oxides, have definite crystal structures of their own. Their EOS properties at STP, such as density and bulk moduli, do not correspond to the properties that would be expected for mixing without chemical or structural reaction. Another type of mixing common in silicates is continuous substitution of Fe and Mg, e.g., $(Mg,Fe)SiO_4$. One would expect that if the EOS of the end members were known, it should be possible to predict the EOS for any intermediate composition of this latter set quite well.

There are obviously many ways to perform a mixing calculation for determining Hugoniots, all involving some degree of approximation, some because of uncertainties in temperatures caused primarily by lack of knowledge of some of the thermodynamic properties. However, we note that if one had a static-isothermal press, and if no reactions took place, the P-V locus measured should be precisely the same as that calculated if one used additive volumes. This was the approach used by the Los Alamos group [17], and since they demonstrated that the procedure did quite well in several tests, that is the approach we will use.

In brief, a zero-Kelvin isentrope is calculated for each component in the mixture. For simplicity, and lack of knowledge, the specific heat and $\rho\gamma$ assumed to be constant. The density at zero pressure and temperature is first found, which contains a small error because the specific heat is not constant. The isentropes starting at those densities are calculated by the difference equation (III.5). The zero-Kelvin isentrope, K, for the mixture was found from the equations

$$V_K = \sum m_i V_i(P) \tag{III.18}$$

and

$$E_K = \sum m_i E_i(P) \quad . \tag{III.19}$$

In the above, all the quantities are taken on the appropriate isentrope, and m_i is the mass fractions of each component. Similarly, $\rho\gamma$ and C_V for the mixture required for the calculations can be determined:

$$\rho\gamma = \sum m_i(\rho\gamma)_i \tag{III.20}$$

and

$$C_V = \sum m_i(C_{vi}) \quad . \tag{III.21}$$

If the parameters used in the two previous equations are known, they can be incorporated in the calculation rather than estimated. The Hugoniot for the mixture is then calculated

27

in a manner similar to that for reflected shocks, using the equation

$$P_H = \frac{P_s - \rho\gamma[(E_s - E_o)]}{1 - \rho\gamma(V_H - V_o)/2} \quad , \tag{III.22}$$

where P_s and E_s are on the isentrope and E_o and V_o are the starting conditions for the new Hugoniot at $P = 0$. It is to be noted that the V_o used in the previous equation is that measured on the material of interest. If there are voids in the sample, this procedure wiil correctly account for them, as in the similar situation where Hugoniots for porous materials were calculated with Eq. III.8.

Several tests of the usefulness of the above procedure were presented. One test was conducted on a series of commercially available sintered mixtures of Cu with W and tungsten carbide, and Ag with W, called Elkonites [Morton Co]. The U_s-U_p Hugoniots for some of the mixtures are plotted in Fig. III.6, and the values of $P - \rho$ are plotted in Fig. III.7. It is obvious that the agreement is very good. The downward curvature seen in the U_s-U_p plot in the low-pressure regime is caused by voids or porosity. The percentage composition of these materials can be determined quite well, and in all cases the computed zero-pressure density was higher than that measured, indicating a small amount of porosity. The measured density was used for V_o in (III.22), which accounts for the curvature in the calculated Hugoniot and data plots.

Hugoniot data for two Au-Ge alloys (Fig. III.8) are also compared with the calculated Hugoniot. Here the Hugoniot of the Ge end member has a very large density increase, probably because of shock induced melting. Again, measured and calculated Hugoniots are in good agreement. Data for three iron-nickel alloys are also compared (Fig. III.9), with similar good agreement. The Hugoniot of the iron used for the calculation was in the hcp phase and the Hugonlot for the Ni was in the fcc phase.

IV. PHASE CHANGES AND HUGONIOTS

A. Shock Wave Stability

During World War II, Bethe [18] wrote a paper on the theory of shock waves in which he showed that for a shock wave to be stable the sound velocity of the material must increase. In general, this would mean that a P-V EOS would be concave upward. It is also true that for the shock front to be stable the shock velocity must increase with pressure. This is probably obvious, since if the shock velocity decreased with pressure, the

lower-pressure part of the wave would simply outrun the high-pressure pulse. For a normal material, $d^2P/dV^2 > 0$, so we expect that shock waves should be stable. However, if there is a phase change, regions could exist in the material where the P-V EOS would appear to be concave downward as indicated in the P-V Plot (Fig. IV.1). Referring to Fig. 1 we see that for the wave to be stable,

$$U_{S2} \geq U_{S1} \quad . \tag{IV.1}$$

If we substitute the P-V shock-velocity relationship, Eq. (II.41), in Eq. (IV.1) and remember that the second wave is riding on material moving with a particle velocity U_{p1}, we obtain

$$V_1[(P_2 - P_1)/(V_1 - V_2)]^{1/2} + U_{p1} \geq V_0[(P_1 - P_0)/(V_0 - V_1)]^{1/2} \quad , \tag{IV.2}$$

and replacing U_{p1} by Eq. (II.42),

$$V_1[(P_2 - P_1)/(V_1 - V_2)]^{1/2} + [(P_1 - P_0)(V_0 - V_1)]^{1/2} \geq V_0[(P_0 - P_1)/(V_0 - V_1)]^{1/2} \quad . \tag{IV.3}$$

On rearranging,

$$(P_2 - P_1)/(V_1 - V_2) \geq (P_1 - P_0)/(V_0 - V) \quad . \tag{IV.4}$$

Thus the slopes in the P-V plane must increase or the shock front will not be stable.

One material known to have an anomalous compression curve is fused quartz. Bridgeman [19] found that with increasing pressure it became more compressible, that is its P-V locus is concave downward. From the above analysis, Eq. (IV.4), a nonstable wave should develop if the material is subjected to some type of high-pressure loading. Such behavior can be observed in fused silicate when subjected to shocks of less than 300-kb. The initial sound velocity is ~6 km/s but it decreases with pressure thus a wave is generated in which the lead moves at 6 km/s but the higher pressure component of the wave moves at ~5 km/s. Thus, the further the wave travels the more smeared out it becomes. This example of a nonstable shock wave is illustrated in Fig. IV.2. Fused quartz also has a phase change beginning at ~100 kb so there is additional structure in the wave front caused by a transition. It takes a pressure of about 300 kb before a stable shock wave develops but this still does not overdrive the anomalous compression region. The type of Hugoniots that would result in a particle velocity time record shown in the previous figure is sketched in Fig. IV.3.

The most likely type of transition to be observed in shock-wave studies would be a phase change with an increase in density. Because of various thermodynamic effects

29

outlined earlier, the Hugoniot will not coincide with an isotherm where the phase change is manifested as an isobar in the P-V plane. In addition to the thermal effects, there are also nonequilibrium conditions and rate processes often present. The effect of transitions and other considerations on the structure of the shock front is illustrated in the figures. The solid curves in the P-V plane are the Hugoniot loci for a material that has an equilibrium EOS shown by solid lines. In the first example (Fig. IV.4) the onset of the phase change is drawn higher than that of the equilibrium. Two reasons for this are: (1) the phase change might be quite slow relative to the time scale used in the shock-wave experiments, hence requiring some amount of overdrive to initiate it; or (2) if the slope of the phase line is positive, the increase in temperature in the shock wave would require that a higher pressure be reached before the Hugoniot intersects the phase line. The Hugoniot transition point could actually lie below the isotherm for at least two reasons: (1) a rather large shear stress is usually induced in shock waves, which could enhance the phase change relative to a pure hydrostatic stress, which means that the material was not in thermal equilibrium. Or, if the slope of the phase line is negative, the shock wave will cross the phase line at a lower pressure relative to the cold isotherm. In the next figure (IV.5) are drawn a P-V plot where three shock states are indicated: (1) the onset of the transition, (2) the pressure of the shocked state, and (3) the intersection of the ray from 0 to 1 and the Hugoniot. The second column of figures shows the type of wave profiles that might be observed, and the third column the type of U_s-U_p Hugonlots that could result from these phase changes. The region between points 2 and 3 in the U_s-U_p Hugoniot in Figs. IV.3 and IV.4 is drawn with point 2 considerably lower than 3 and with considerable curvature, indicating that the transition under shock conditions is close to equilibrium. In some cases the region between 1 and 3 might contain sections with concave-downward curvature. When this occurs, and the pressure lies below the point $0 \rightarrow 3$ ray, a two-wave structure will occur but the wave profile will show dispersion and curvature. This would indicate that the transition has not gone to equilibrium. Three examples of this are illustrated on Fig. IV.5. If point 2 lies above the $0 \rightarrow 3$ ray, a two-wave structure will not exist. However, if there is some downward curvature, the resulting wave profile will show a sharp rise followed by a rounded dispersive top whose actual shape, of course, is related to the shape of the P-V curve. If the region between 2 and 3 is concave upward, sharp shocks can develop. This would be the case for shock pressures lower than indicated. For these cases the U_s-U_p Hugoniot can show a gradual increase from 1 to 3. When shock-velocity measuring techniques that detect only the arrival of the shock front are used, the region between points 1 and 3 will appear as a region of constant shock velocity.

B. Phase Lines, P-V curves and U_s-U_p Hugoniots

A first-order phase change is characterized by the slope, dP/dT, of the phase line, which is usually given by

$$dP/dT = \Delta S/\Delta V = \Delta H/T\Delta V \quad , \qquad\qquad (IV.5)$$

where ΔS and ΔV indicate the difference in entropy and volume between the initial and final states. In Fig. IV.6 are sketched two systems where dP/dT is positive. In the first set, the Hugoniot is centered in the low-temperature/high-density phase. This is the type of behavior to be expected for normal melting. As can be seen, there is really very little change in slope going through the mixed phase region, and not necessarily much change from region I to II. For this region it appears that normal melting would be quite difficult to detect from Hugoniot measurements, because the thermodynamic properties of the material are so similar in both phases. As indicated, for melting, dH/dV is nearly continuous. These drawings show that the temperature must increase on the Hugoniot as it crosses the mixed phase region, but the temperature will increase at a lower rate. In this and the next figure, the curves are drawn for assumed equilibrium situations. It is reasonable to expect that for a normal material the Hugoniot would cross the melting curve, because with increasing pressure the temperature along the Hugoniot increases more rapidly. In the second set of figures (IV.6) the Hugoniot is centered in the low-pressure/low-density phase, and, as indicated, a two-wave structure is possible, depending on how the shock wave goes through the mixed-phase region. The graphite-diamond transformation would be of this type. In both of the previous examples the temperature must increase.

Figure IV.7 illustrates the case where dP/dT is negative. Here the Hugoniot must originate in the low-density phase if it is to cross the phase line. A two wave system can develop, depending on the caveats discussed previously. For this type of transition we see that the temperature must decrease if the reaction goes to equilibrium conditions. If $dP/dT < 0$ we note from (Fig. IV.5) that the entropy must decrease, and since the second shock must increase the entropy, we conclude that there is no way that equilibrium states can be observed in the shock-wave experiments with these conditions. The α-ϵ transition in iron is representative of this type of transformation. However, the onset of the transition can be at an equilibrium state.

It should be noted that even though the final states in a shock-induced transition are not at equilibrium, it is still quite possible to detect the beginning of the transition with

31

shock-arrival measurements, since even if only a small amount of material is transformed it can give rise to a two-wave structure that can be observed readily.

We have indicated that some first-order phase changes result only in a change in slope on the U_s-U_p Hugoniot. A similar behavior would be observed if the material only undergoes a second-order phase change, e.g., a change in compressibility. This type of behavior has been observed in aliphatic polymers, where it is believed dissociation is occurring [20].

Although it is not ordinarily considered a phase change, the relaxation resulting from a one-dimensional compression to a hydrodynamical state will also cause the formation of a two-wave structure in shock fronts. For weak shocks in materials with rigidity, the shock front separates into two waves, the first traveling at the longitudinal sound velocity and the second at the bulk wave velocity [14]. The amplitude of the first wave is called the Hugoniot elastic limit, HEL, which can be quite large in some materials with large yield strengths. If the amplitude of this elastic precursor is great enough, first-shock-arrival measuring techniques often detect it. Often the records appear to have abnormally high-shock velocities. Such data can usually be recognized and treated appropriately. As expected, Al_2O_3 (sapphire) has a huge HEL, which causes considerable errors when making Hugoniot measurements unless proper precautions are taken. If the shock-wave data indicate a phase change, several features can be used to decide whether the transition is due to a phase change or to elastic-plastic flow. If the high-pressure U_s-U_p data extrapolate to a zero-pressure value substantially below the bulk sound velocity, then it must be concluded that a phase change exists. If the data extrapolate to a velocity higher than the zero-pressure sound velocity, a transition is indicated, but most likely to a different type. Such behavior would be compatible with a second-order phase change as a result of which the material has become more compressible. Ordinarily the high-pressure phase is less compressible, but in some compounds, if low-pressure bonds are destroyed, the material can indeed become more compressible. Even though the high-pressure data extrapolate to the zero-pressure bulk sound velocity, low-pressure phase changes can exist. For these cases, and those for which the data do not go to high enough pressure to resolve the problem through the previous considerations, it is stil' possible to decide whether or not a transition exists. To do this, first examine the flat segment of the U_s-U_p Hugoniot. If this does not occur near or above the measured longitudinal wave velocity, one is not observing the effect of a two-wave structure due to elastic-plastic flow. If the shock velocity happens to be in agreement with the longitudinal wave velocity, one must then check to see if there are any lower-pressure data that extrapolate toward the bulk sound velocity. If so, it must

be concluded that agreement with the longitudinal velocity is purely coincidental, because if it were indeed due to an elastic wave, the low-pressure data would have to extrapolate to the zero-pressure longitudinal value. It should be remembered that if any of the last two conditions are satisfied, the existence of a phase change is established. Two necessary conditions for establishing that the wave structure is due to an elastic wave are that the low-pressure data extrapolate to the longitudinal sound speed or that the flat region be at or slightly higher than the longitudinal sound speed and also that the high-pressure data extrapolate reasonably well to the bulk sound velocity.

C. Metastable Hugoniots and their Derivation from Shock-wave Data

It is sometimes desirable to estimate the high-pressure EOS of some material that has undergone a transition in terms of its zero-pressure parameters, or the Hugoniot EOS of the material if it were shocked from its metastable state. From examination of the diagrams of the schematics of the effects of phase changes, Figs. IV.6 and IV.7, we see that it is obviously incorrect to extrapolate the high-pressure U_s-U_p Hugoniot data down to zero pressure, because this results in zero-pressure sound velocities or compressibilities that are often lower than those of the original material. A phase change, with an increase in density, should most likely also have an increase in its bulk modulus. More reasonable results are obtained if the extrapolation is done in the P-ρ plane, but even here the extrapolation is quite subjective because the rate of change of curvature must be estimated. As was discussed earlier, the linear U_s-U_p Hugoniot is the logical one to be specified for a normal material. A procedure for finding this best Hugoniot was first described in 1963 in determining the EOS of stishovite [21], and later in more detail [22] for some rocks. It is an iterative method for finding a ρ_o, C_o, and S for the metastable Hugoniot, which, when used with certain initial conditions, makes it possible to calculate or reproduce the original Hugoniot data. The schematic in Fig. IV.8 illustrates the conditions that exist in the transition region and that must be satisfied to determine the difference in internal energy of the two states at $P = 0$. The procedure is first to calculate all the thermo-dynamic quantities T, S, E, and the Gibbs free energy, G, at the P-V of the transition (Point 1). This requires that the Grüneisen parameter and specific heat and the slope of the phase line be known or estimated. These values must also be known or estimated for the metastable phase, and while they need not be the same, except for the slope of the P-T phase line, they are usually assumed to be. An isentrope is calculated from an assumed metastable Hugoniot that satisfies the condition that the temperature at 2S is the same as that at Point 1. This determines ΔV and hence ΔS. Since the free energy must be the

33

same on the phase line $(G_1 = G_2)$, the energy difference, $E_{0A} - E_{0B}$, can be found. With this a Hugoniot centered at the original state can be calculated from the assumed or trial Hugoniot. The somewhat familiar form of the working equation for doing this is

$$P_C = \frac{P_B[1 - \rho\gamma(V_{0B} - V)/2] + \rho\gamma[E_{0A} - E_{0B}]}{1 - \rho\gamma(V_{0A} - V)/2} \quad . \tag{IV.6}$$

This is essentially (III.8) with an additional term to account for the difference in the internal energy of the two states. This P-V Hugoniot can then be transformed to a U_s-U_p Hugoniot by the application of Eqs. (II.41) and (II.42). The values of U_p on the calculated Hugoniot are found at the shock velocity of the data points. The minimizing procedure is arbitrary, but usually C_0 and S are held fixed and the density ρ_0 is found such that $\Sigma\Delta U_p = 0$. This variation tends to move the calculated U_s-U_p Hugoniots more or less parallel to themselves (Fig. IV.9). C_0 is usually varied next and the $\Sigma|U_p|$ or ΣU_p^2 is minimized. This variation tends to rotate the calculated U_S-U_P trial curves (Fig. IV.10). Finally S is varied, which tends to change the curvature. This last minimization is the least sensitive of all (Fig. IV.11). If any parameter or parameters are known, they can be specified, and the resulting solution is called restrained. If the density of the high-pressure phase is measured from shock recovered or synthesized samples, that can be used and the bulk modulus will be much better constrained. If enough material can be obtained to measure both the density and the sound speed, then the determination of the slope, S, becomes meaningful.

D. Elastic-Plastic Flow

Elastic-plastic flow is only of secondary interest to the subject being addressed in this lecture. But by the nature of our experiments it is almost always with us. In the plate-impact experiments, the initial microscopic motion must be one-dimensional on both the macro and micro scale. If the material is isotropic, the shock wave must travel at a velocity governed by a one-dimensional EOS. This means that the shock-wave velocity would be determined by the velocity associated with the longitudinal sound velocity. The meaning of this is illustrated in Fig. IV.13, where we have drawn two hypothetical linear U_s-U_p EOSs. The one-dimensional nature of the flow can only last for as long as it takes for the material to relax to or toward the lower equilibrium EOS. For most materials, this relaxation process begins almost instantly. Exceptions of some inter.st are materials like graphite when shocked perpendicular to the basal planes. Here the forces between planes are so weak that this is simply the easy mode of compression. Even though relaxation usually occurs immediately, there are many instances in which the longitudinal states

34

do not reach equilibrium. How closely the approach equilibrium and how the materials relax are governed by its elastic properties. These features are readily observable by several techniques in low-pressure shock studies. The shear modulus is the dominant elastic parameter governing the relaxation flow. What must be considered is that for an ordinary material the one-dimensional macroscopic flow produces large shear stresses, which must eventually result in flow by slip on the large scale and which in turn are formed by dislocations on the micro scale.

Some additional features in Fig. IV.13 deserve comment. The three-dimensional equilibrium and experimental U_s-U_p curves have been drawn with straight lines because of experimental evidence. The one-dimensional longitudinal curve and the transverse curve have both been drawn with a downward curvature. The shape of the transverse velocity curve is due to the shear modulus, and it is shown increasing originally because static measurements have shown that the shear modulus increases with pressure. However, because of the rapidly increasing temperatures along the Hugoniot the shear moduli will decrease, so that curve has been drawn with a downward curvature. If the material melts on the Hugoniot, the shear velocity will become zero. At present there is evidence that the shear velocity does not smoothly approach zero, but disappears rather abruptly. When that happens the one-dimensional curve becomes the equilibrium curve. No evidence exists to show how close the experimental and equilibrium curves are at high pressure. Most likely the deviatoric stress, or the separation, is comparable to that observed at low pressures. This would imply that it would only be a small percentage of the total stress. The Hugoniot states calculated from the conservation equations are correct, even if the states are not at the hydrodynamic equilibrium condition; it simply means we do not know precisely what has been measured.

V. EXPERIMENTAL TECHNIQUES

Many techniques have been used for studying shock-wave phenomena. In this section we will describe briefly some experimentation related to these lectures. When appropriate, an example or two of typical results will be given. Many techniques have been invented or developed to study shock waves. These range from the early systems, which detected arrival times only, to devices that make it possible to make time-resolved pressure and material velocity measurements to a few nanoseconds. We will limit this discussion to a few relatively simple methods that determine only arrival times, from which average shock velocities or material velocities are calculated; some temperature measurements; some

optical methods for determining sound velocities at high pressure; and some recovery systems. The simple X-T measurements are included because they form the data base on which most of the high-pressure EOS is based. It should be noted that this also includes most static high-pressure data, since their calibrations are based on shock-wave data. Temperature measurements are important since they are the only way we are going to learn about specific heats at extremely high temperatures and pressures where other quantum effects come into play. These effects can be seen in the increasingly sophisticated band structure calculations, and experimental verification is needed. The sound-velocity measurements have given us the opportunity to determine both the melting point of solids on the Hugoniot and the Grüneissen parameter. Both of these quantities are required for a more complete understanding of nature. Some very elegant and sophisticated techniques have been omitted simply because they have not been used to address the three major problems: accurate Hugoniot, temperature, and sound velocity measurements. The other techniques have primarily addressed the study of elastic-plastic flow and other problems at relatively low pressures.

Shock waves were first used to obtain EOS data for solids during World War II. In 1945 a program was initiated at Los Alamos National Laboratory (LANL) to determine the EOS by shock waves using pin contactors and oscilloscopes. Shock velocities were determined by shock arrival times from pins located in holes in the sample and the material velocity, U_{fs}, by pins off the surface. To our knowledge, the first report of that work was published in 1955 [3]. By using various high explosives (HE) in contact with metal plates, pressures to about 500 kbar were attained in dense materials like copper. At that time Professor Bridgman's upper limit was about 100 Kb. The ability to fabricate high quality explosive lenses with fast and slow detonating components made it possible to generate relatively large plane waves that could be used to obtain shock-wave data on several materials simultaneously. Several such lens systems have been developed by various laboratories, including air lenses, where the slow component is an accelerated metal plate whose velocity is much slower than the detonation velocity of the high explosive. In the mid-1950s, HE systems were used to accelerate metal plates, which were then used to generate even higher pressures. Figure V.1 is a drawing of an HE system used in the 1950s. Black powder guns have been used as well as gas-propelled guns. With these only modest pressure could be attained, but the small gas guns could be used in a laboratory on a college campus if desired. With the advent of the space age, large two-stage guns were developed to study re-entry ballistics, which were capable of accelerating small projectiles (originally spheres) to velocities in excess of 7 km/s. In 1966 Jones, Isbell, and Maiden

[23] adapted one of these guns for doing EOS work. Several of these types of guns are currently being used. The two-stage gun at LANL consists of a pump tube ~15-m long and 100 mm in diameter, an accelerating reservoir, the launch tube, ~10-m long and ~30 mm in diameter, and an impact chamber. The pump tube is filled with hydrogen gas, which is compressed by a projectile made of lead and plastic launched by relatively slow-burning powder in the magazine. The two barrels are coupled with what is called an accelerating reservoir, where the hydrogen gas is compressed and then accelerates a plastic sabot with a metal disc on it. Spherical implosion systems can, of course, reach much higher pressures, but they are very expensive and not as convenient to use. It has been surmised that the Soviets used these in their early [9–11] 100-GPa experiments. Experiments have been done using the energy from nuclear explosives, which have generated shock pressures in excess of 500 GPa. Unfortunately, no measurement of the material velocity were made in those experiments; only relative shock velocities. Because of this, no further mention will be made of them.

A. Electrical Pins

Probably the first shock-velocity detecting systems used electrical shorting pins [3,5,6]. Electrical signals were generated when metal pins were shorted by shock-accelerated metal plates. These signals could be displayed on oscilloscopes, a few for each sweep, or on rasters where many signals could also be recorded with good time resolutions but for longer times. The signals could be used to detect time differences between shocked samples of different thicknesses. These then give a straightforward method for determining shock velocity. In these experiments and others, many pins must be dedicated to establish the shape of the shock-wave arrival. By placing pins known distances away from the free or front surface of a shock-loaded metal plate, the free surface velocity, U_{fs}, could be determined. In the early 1950s it was standard practice to assume that U_{fs} was twice the shock particle velocity in determining Hugoniot parameters. By setting the many pins with different spacings and accurately measuring their position, a replica of the shape of the shock-wave could be determined from the derivative of the data. Minshall [5], who was extremely meticulous in assembling and measuring these target assemblies, detected the elastic wave in shocked iron. Later, employing similar techniques, he and colleagues [24] presented data (Fig. V.2) showing that in shocked iron there was an additional wave propagating at 13 GPa. They also described the necessary unfolding required for reducing free-surface x-t data to P-V states in a multiwave system. The signals from more than 60 pins were recorded on oscilloscopes in this experiment, which implies that considerable

effort was expended in performing this measurement. Some of the optical experiments to be described later eliminate much of this work. In 1964 R. Dick began using shorting pins to measure the EOS of liquids [25–26]. The experimental configuration he employed for measuring shock velocities in liquid N_2 [25] is shown in Fig. V.3 and the data in V.4.

Shorting pins are still being used as shock arrival detectors on the high-velocity two-stage guns, e.g., Morgan, 1974 [27] and Mitchell and Nellis, 1981 [28,29]. In these experiments the diameter of the target is fairly small (20–25 mm) so that only ten or so pins are used, usually detecting shock arrival at two thicknesses at different radii (Fig. V.5). This is sufficient to determine projectile tilt. Bow is essentially determined by a pin at the center. By use of high-quality coaxial cable delay lines, the time interval between signals can be made quite small and recorded with fast-sweeping oscilloscopes, which reduces reading errors. The accuracy in determining shock velocity is probably about one percent. However, the projectile velocity can be determined to ~0.1 percent, since the projectile's transit time can be measured over a long distance (0.2–0.3 m). Various detectors have been used to measure the impactor velocity, including interrupted laser light, flash x-rays, and magnetic pickup coils. This is a major advantage of using these guns as opposed to high explosive systems. Records for various diagnostics are shown in Fig. V.6 for an experiment on the gun.

B. Flash Gap Technique

Almost all the optical techniques used to study shock-wave phenomena rely on the use of a sweeping image or smear camera. Somewhere in the camera, a rotating mirror in the optical path causes the image to move across the film plane. We do not know when the first smear camera was constructed, but their origin undoubtedly goes back to around 1850, when rotating mirrors were used to determine the velocity of light. By World War II many sweeping image cameras were used with writing speeds of a few $mm/\mu s$. This was soon increased to almost 10 $mm/\mu s$, and finally with the advent of beryllium mirrors, to about 20 $mm/\mu s$. Electro-optical devices available now have writing speed capabilities that far exceed ordinarily shock-wave diagnostic requirements.

The flash-gap type of experiment first described by Walsh and Christian [4] has probably been used more than any other technique to obtain Hugoniot data. The principle of its operation is that strongly shocked gases emit radiation. Walsh put Plexiglas blocks with spaces approximately 0.1 mm over different areas of the target and viewed the radiation through a set of slits. When the free surface of the material traverses the small gaps,

the shocked gas radiates. This radiation is sometimes observed, depending on the width of the slit and other things, but it is much weaker than the light emitted when the gas shock is reflected back from the plexiglas window. This burst of light is quite short but it is long and bright enough to expose the film. The light is extinguished or the plexiglas becomes opaque, so the camera records an image approximately the width of the slit as if it were taken instantaneously. Details of some flash-gap systems are shown in Fig. V.7. The system as described is used almost exclusively for measuring discrete time intervals. Many modifications of the target assembly exist.

C. Standards

The definition of the word standard is rather nebulous. In general, any material that can be used as a basis for determining the EOS of other materials is in principle a standard. For the present discussion we are being slightly more restrictive in that we will consider a material a standard only if its EOS has been determined in some manner that does not require the use of the EOS of some other material.

It has long been recognized that Hugoniot data could be obtained by simultaneously measuring the impact velocity of a rapidly moving plate and the subsequent shock velocity induced in a stationary plate. If the driver plate and target plate are made of the same material and are in the same thermodynamic state, then the symmetry of the collision requires not only that the pressure be the same in the driver and in the target plate but also that the particle or material velocity behind the shock wave be exactly one-half the driver velocity. When using gun devices the projectile velocity can be measured with very good precision by monitoring its free-flight motion over relatively long distances by electronic pins or other suitable devices. This has been done at LANL, Caltech and LLNL, for example, using two-stage gun devices. However, the bulk of the experimental data obtained here has been obtained using explosively accelerated driver plates. Unfortunately it is more difficult to make accurate measurement of the driver plate velocity, U_D. The biggest difficulty is due to the fact that the driver plates are not moving at constant velocity at the time of impact, which means that the velocity must be determined at some position, over a very short interval of motion. Pin techniques have also been used successfully in explosive systems. However, for standards developed at LANL we have used a sweeping image camera to record shock-wave arrival by the flash-gap technique described earlier.

The shock velocity was determined in the usual way by measuring shock wave arrival times at different levels in the target plate. In order to circumvent the fabrication diffi-

culties encountered in making precise velocity measurements of the driver plate directly, a small groove was machined in the impact side of the target plate, which allows a differential measurement of the shock-wave velocity and driver-plate velocity when the shock-wave arrival was observed over a plane area from the free surface direction.

Details of the assembly can be seen in Fig. V.8. The upper part of the figure shows the arrangement of the plastic flash blocks which in effect gave four independent sets of U_s-U_D data points. The left-hand side of the assembly was used to measure the shock velocity and the other side the driver velocity. Each set of blocks was viewed through four or five slits. The cross-sectional views below are designs used in different pressure regions. The first two designs are for the low-pressure regime; the upper one has the U_D groove in the correct position. At higher pressure the grooves are not as readily pinched off and can be made as deep as the target plate thickness allows. For the high-pressure shots the target plate thickness is limited by the thin drivers (0.9 mm) used to reach high velocity.

A resulting photographic record is shown in Fig. V.9. This was a relatively low-pressure shot and the uppermost cross-sectional design was used. In this record, time increases downward; hence, the early traces on the left-hand side represent the shock-wave arrival at the bottom of the narrow groove. The corresponding reference traces establish the wave arrival at the top of the plate. Since the flash blocks on the right-hand side were at a lower level, the reference traces for the U_D measurements arrived earlier. The offsets represent the difference in the driver-shock transit times through the small gap machined in the bottom of the plate.

As simple as such a system appears to be, considerable care must be used in choosing the correct groove depths so that optimum precision can be obtained. In those experiments the width and lateral location of the grooves were always the same. In low-pressure shocks, the U_D traces are pinched off by the sidewise rarefactions caused by the shock wave, which runs considerably ahead of the projectile. Thus, the driver velocity can only be measured over a run of about 1 mm. Data for several materials were reported in Kinslow's Hypervelocity Impact Phenomena book. Linear fits of the data were adequate for all except iron, where a small amount of curvature or a slight break in the curve can be observed. This lack of linearity has been observed in other materials that have undergone a phase change. In iron it was thought that the curvature or change in slope could be due to additional phase changes, either the hcp $\rightarrow$ fcc transition, the solid-liquid transition, or both. These techniques are not capable of resolving this problem. The zero-pressure sound

velocity data measured here were not used in the least-squares fits. The resulting U_s-U_p and P-U_p Hugoniots are shown in Figs. V.10 and V.11.

At least two other materials qualify as standards, Pt and Ta. Symmetrical impact experiments were performed with two-stage gun experiments both at LANL and LLNL by Morgan [28] and Mitchell and Nellis [30].

D. Impedance Match Solution

Although much data have been obtained using symmetrical impacts, which includes all those materials we consider to be primary high-pressure shock-wave standards, most data have been obtained using the shock impedance technique developed by Walsh et al. [1955]. With this method relatively small samples of the material being studied are placed on a flat plate, often called the standard or the base plate. Since the particle velocity and pressure at the standard-sample interface must be the same, a graphical or numerical solution for this requirement in the pressure-particle velocity plane yields the necessary values. This establishes the pressure and particle velocity of the other samples. (see Fig. V.12). To calculate the reflected shock states and isentropic release states, one must use the calculations outlined earlier. The impedance match solutions are done in the P-U_p plane, but the cross curves are calculated in the P-V plane. It is known that rigidity effects are present in these shocked conditions, but they are ignored now as they were then in making the impedance match solutions. In which case release states are assumed to be isentropic (constant entropy, S) and can be calculated via the methods outlined earlier. In the majority of the measurements the shock velocity was measured through two samples of the standard to establish the shock strength in the standard. A drawing of a typical assembly is shown in Fig. V.13 and an enlargement of a record in Fig. V.14.

In the previous section the experiments to determine standards and some results were presented. However, when any material is used as standards, some form of the Grüneisen function must be used to calculate reflected shocks and rarefaction waves so that the impedance match technique can be used to obtain Hugoniots of other materials as described in this section. A necessary but not sufficient condition for their adequacy is that we should be able to reproduce the Hugoniots of the others when one is used as a standard in the impedance match system. In the work reported in Kinslow [17], five materials were considered as standards. These were all cross checked as described above. The results of three of these cross checks, using the standards most frequently employed, Cu, 2024 Al, and Fe, are reproduced in Figs. V.15–V.17.

41

These good results do not preclude the possibility that the EOS of all of these materials contain some type of systematic error. One possible source of error is the rigidity of the materials. Until shock heating melts the material, rigidity effects will be present. It is not known how far the actual states on the Hugoniot are away from equilibrium, or what effect this unknown deviatoric stress will have on the reshock and release states of the standards.

E. Interferometry Methods

The first interferometer used in shock-wave studies was a "Michelson interferometer," MI, developed by Barker and Hollenbach in 1965 [31]. This instrument had a practical velocity limit of 0.1 km/s, because the number of recorded fringes was proportional to interface displacement. To extend the velocity range, they [32] developed the "velocity interferometer," VI. For this interferometer the recorded fringes were directly proportional to the interface velocity. Both the MI and the VI required spectrally reflecting surfaces. This criterion limited the upper velocity range of the VI because there is usually substantial surface degradation at pressures exceeding 10 GPa. Phase changes can also influence surface integrity. To circumvent the problem of surface degradation upon shock loading, Barker and Hollenbach in 1972 developed the VISAR [32], which is their acronym for "Velocity Interferometer System for Any Reflector" (Fig. V.18). In a VISAR the reflecting surfaces can be either spectral or diffuse. However, for most applications the surfaces are initially reported to be diffused reflectors to minimize reflectivity changes during shock-wave experiments. A VISAR modification developed by Hemsing in 1979 uses all four quadrature signals rather than just the two used in the original design [33]. This modification has resulted in substantial improvements in both data acquisition and data analysis. In a typical VISAR experiment a transparent window with a reflecting coating is put on the front surface of the sample being investigated. This helps maintain surface quality and pressure. Three windows commonly used are sapphire, LiF, and PMMA. It is expected that all these windows would themselves radiate at some pressure, and if so they would also become absorbers. Most likely these windows are absorbing, but not enough to quench the intense monochromatic radiation from the laser. Interferometers have been used increasingly for work in geophysics, especially to study the response of crustal minerals to shock-induced impacts [34]. Figure V.19 is an example of the result of a VISAR experiment to study the shock-wave structure.

F. Temperature Measurements

We have shown in Sec. III how to calculate temperatures along the Hugoniots. In general, the specific heat, C_v, and the Grüneisen parameter, γ, are required to do this, in addition to the measured Hugoniot. While there are usually fairly good theoretical reasons for choosing values for these parameters, it would increase our knowledge considerably if the temperature could be measured behind the shock front and these parameters derived. Of course the effect γ and C_v would have to be separated. This can be done because there are other types of experiments in which γ can be obtained.

Temperature measurements on shocked transparent materials was begun by the Soviets by Kormer, Sinitsyn, Kirillov, and Urlin [35] in 1965 on some alkali halides. This work was done with two-color pyrometry. They observed that the intensity of the radiation emanating from the shock front rose very slowly, implying that the shocked material was not optically opaque. Current measurements fortunately show that the onset of radiation can be quite steep (a few ns) for many materials. Others performed additional radiation measurements. In 1968 Kirillov, Kormer, and Sinitzyn [36], studied ionic crystals at somewhat lower pressures and reported that the inferred temperatures were much higher than could be accounted for on the basic of equilibrium thermodynamics. They estimated that the thermal energy imparted by the shock wave was only about a fifth of that required to give the apparent thermal radiation. They proposed that plastic deformation created a large number of free electrons that only slowly came into equilibrium with the lattice. Later, 1969, Kormer et al. [37] reported on non-equilibrium temperatures in ionic crystals measured photo graphically by a method used by Model in 1957 for shocked gases. These were very high pressure experiments. Zel'dovich in 1968 [38] proposed that there was a layer of nonequilibrium electrons behind the density discontinuity that completely screened the radiation from the electrons in equilibrium with the lattice. In the alkali halides it appears there is a limited pressure range where thermodynamic properties can be measured. An increase in interest seemed to occur at the end of the 1970s. Lyzenga and Ahrens [39] described a six-channel optical pyrometer, (Fig. V.20), and they reported some data on SiO_2 on Mg_2SiO_4 in 1980 [40]. They calibrated with a tungsten filament and fitted the results with a Planck's distribution (Fig. V.21). If the material has a constant emissivity as a function of wave length, then a value for the average emissivity can be obtained when fitting the data to the Planck radiation function. However, if it is not constant the radiation curve becomes distorted and an incorrect temperature inferred. More recently Lyzenga and Ahrens and Mitchell presented data on SiO_2 (Fig. V.22).

In 1980, Suquira, Kondo, and Sawaoka [41] described their optical pyrometer, which

used a holographic grating to disperse the radiation on a multichannel analyzer with silicon-intensified targets. A similar system was used by Kondo and Ahrens [47]. A record of the spectra from shocked calcite they measured is reproduced in Fig. V.23. The detector had 490 channels, which were sampled in groups of 10. The system relies on gating circuits to sample the radiation over the correct time interval. If the radiation is not uniform over this interval some reservations should be made about its assumed accuracy. They showed a record of radiation intensity against time in which the light intensity was very nonuniform.

We have photographically determined brightness temperatures for shocked SiO_2 over a broad spectral range ($\sim$400–700 mm) by simultaneously recording the radiation from shocked SiO_2 and the radiation from detonated nitromethane. The radiation from the nitromethane and SiO_2 were viewed through a set of slits of different widths (Fig. V.24) so that the relative intensities could be compared (Fig. V.25) and the temperature of quartz determined from known temperature of the nitromethane and Planck's radiation law. This technique has the nice feature in that absolute radiation levels need not be determined, only the relative radiation of the unknown and the standard. A disadvantage is that it must be assumed that both the standard and unknown radiate like a black body. The data plot (Fig. V.26) shows the effect of a previously unobserved phase change. The data also indicate that the specific heat is substantially different in the two phases. Because the crystal quartz and fused quartz data lie on the same curves it is concluded that the radiation is solely due to the internal energy of the SiO_2, since the fused quartz and crystal quartz are not at the same pressure-density states.

Up to the present time, temperature measurements were restricted to transparent materials. This more or less precluded measuring the shock temperature of most elements. Recently, Bass, Svendsen, and Ahrens [42] reported temperatures on shocked iron. They measured the radiation from the iron through a sapphire window using the techniques described earlier (Figs. V.20–V.22). The temperatures derived are dependent on the transmission of the sapphire and the relative thermal diffusivities of the sapphire window and the opaque sample. Although the sapphire appears to be a good window, neither the iron or sapphire thermal diffusion coefficients are well known. Extraneous radiation from the interface adds further difficulties to these measurements. Efforts to measure the thermal diffusion in shocked materials has begun, and it is hoped that temperature measurements on opaque materials can be made with less uncertainty.

G. Experimental Techniques Using Shock Emitted Radiation

Many transparent materials radiate like a black body. The radiation from these shocked transparent materials can provide an extremely sensitive method of looking for small changes in pressure. We have utilized this feature for detecting rarefaction waves in both transparent and nontransparent materials [43]. The standard technique of impacting a target plate with a relatively thin (a factor of four or so) impactor or driver was used. By using proper thickness ratios, the shock induced in the target will be overtaken by the rarefaction from the back side of the impactor. We have attempted to measure the rarefaction overtaking velocity with some of the *in situ* gauges available, but when the shock pressures were sufficiently high for the results to be interesting, our gauges failed. For nontransparent materials one can usually make the driver and target of the same materials, which is usually the preferred arrangement. For these materials a transparent material, called the analyzer, that radiates like a black body is put on the front surface of the target plate. This plate has areas of different thicknesses, like a step wedge. It can be made of discrete pieces of different thicknesses. When the shock reaches the analyzer it radiates at constant amplitude until the rarefaction wave overtakes it and degrades the pressure, which lowers the radiation intensity. The radiation is viewed through a small hole, ~1 mm in diameter, by the end of a fiber-optic light pipe with a diameter of 0.6 mm, about 20 mm from it. Most scattered light is eliminated by a pair of baffles in between. The light pipes transmit the radiation into PM tubes whose output is recorded on Tektronix 485s. The tubes have Beck's [44] voltage divider circuits, which have rise times of <1 ns. The x-t plot (Fig. V.27), although idealized, is typical for a strong shock in aluminum. Only the lead characteristics of the release w· ɔ are drawn, which here represents the elastic wave in the target and a bulk wave in a liquid analyzer. For materials with elastic-plastic flow the x-t diagram can become quite complicated, and if the amplitude of the elastic release wave is large, it becomes difficult to ascertain where the bulk release wave comes in. Some help in making that determination is obtained by having the elastic overtake position occur in the target. In Fig. V.28 the type of record obtained by this method is compared with one that would be recorded with an *in situ* gauge.

The ratio of the target to driver thickness where the rarefaction wave just overtakes the shock is designated R. In Fig. V.27 we can see that time for shock through the driver and the rarefaction waves to the shock transit time through the target is equal to

$$t = T/U_s = D/U_s + D/C_D^L + T/C_T^L \quad . \tag{V.1}$$

With a little algebra it follows that

$$C^L = U_s(R + 1)/(R - 1) = U_s R^* \quad . \tag{V.2}$$

C^L as indicated in Fig. V.27 is the Lagrangian sound velocity. The actual sound velocity, C, is given by

$$C = C^L \rho_o / \rho \quad . \tag{V.2}$$

R in Eq. (V.2) is in a sense an EOS parameter, since it is the ratio of the sound velocity to the shock velocity. Several analyzers have been used: bromoform ($CHBr_3$), density 2.89 g/cm^3; fused quartz; and some high-density lead glasses with densities of 4.8 and 5.2 gm/cm. A set of records obtained with these is reproduced in Fig. V.29. Bromoform, in spite of being somewhat nasty, is usually used because of its high density and the ease with which high quality assemblies can be made. An example of the level of precision obtainable with this technique can be seen in the distance-thickness plot in Fig. V.30.

If the driver and target are not the same, Eq. (V.1) is modified somewhat because the shock and sound velocities are not the same in the driver and target plates. The sound velocity in the target is now given by

$$\frac{1}{C_T^L} = \frac{1}{U_T} - \frac{1}{R}\left[\frac{1}{U_D} + \frac{1}{C_D^L}\right] \quad . \tag{V.3}$$

Here D and T refer to driver and target and U to the shock velocity. R again is the catchup ratio of the system.

If the impacted plate is transparent, and if it radiates, then the sound speed can be determined on a single sample. A record obtained from the radiation from shocked fused quartz and one on bromoform are reproduced in Figs. V.31–V.32. The quartz sample was made of several layers. An opaque film of Al was vapor deposited on the first interface to prevent extraneous light from shocked gases in the driver-target free run space. Approximately 80% transmission Al films were deposited on the other layers. In the bromoform experiment, 5-micron Mylar films with Inconel coatings were placed in the liquid. Thus, as the shock progressed through the assembly, an increase in the radiation occurred at each interface. If these interfaces are parallel to the shock front the rise time through these interfaces is a measure of the structure of the shock front. Hence a well-determined measure of the shock velocity can be obtained if the spacing is known, as well as the catch-up ratios. Thus, the shock velocity and the sound velocity at pressure can be measured on the same experiment.

II. Recovery Experiments

Probably every shock-wave research group has performed some recovery experiments

at some time or other. There are at least two reasons for this: (1) some interesting things have been observed; and (2) it is just plain fun. DeCarli and Jamieson [45] reported on the successful recovery of diamonds from shock-loaded carbon. We do not believe their recovery system has been fully described, but a modest yield of diamond can apparently be obtained in various explosives systems. The type of recovery system outlined in Fig. V.33 has been used by several laboratories. This particular system was used by Zukas and McQueen [46] to produce fine-grain iron. For recovery experiments we prefer to use impactors as opposed to in-contact HE experiments, because the length of time the samples are at pressure is easily estimated. This also makes it straightforward to specify how thick the front spall plate should be, and approximately where the side protection rings should be. When these considerations are observed, the central regions are recovered with remarkably little distortion. There is some distortion where the samples are located, which is to be expected because the samples and the holders do not have precisely the same shock-wave characteristics, e.g., shock impedance and compressibilities. We have used iron for most experiments because it is cheap and strong and comes in in convenient sizes for making the assemblies. We have found that some materials, boron nitride for example, just left the holes they were placed in. For BN this was probably due to the large phase change in that material. For these materials we simply countersink a hole in the top of the container and weld a plug in place. Reasonable care should be taken to avoid altering the samples by high temperatures. Welding is not required for most materials.

Rather than use a conical plane wave HE lens, we prefer to use a plane air lens to initiate the driving HE. Line-wave generators are used to initiate a sweeping wave in a thin sheet of HE that drives a metal plate so that it reaches the HE charge more or less simultaneously. This type of system is used for most recovery shots to minimize the cost and to minimize the total amount of HE used in the experiments.

Another recovery system (Fig. V.34) that has been used frequently is the cylindrical sweeping wave system. The material of interest is loaded into a pipe, usually stainless steel. Sometimes end plugs are used, other times the ends of the holder pipe extend beyond the sample are simply extruded together in the shot. Deta sheet is wrapped around the holder. The thickness of the wrap gives some control of the pressure pulse generated. To minimize the amount of explosive and to increase the pulse-time response, confining shells are often used. Here the annulus between the HE and the confining shell wave was sometimes filled with Hg, thus eliminating any machining and problems of putting the HE in the pipe. Similarly Comp C can be used by simply packing it between the inner pipe and confining

pipe. A disk of explosive is placed in contact with the charge on one end and is initiated at the center. All one needs to do now is to pick up the pieces. If a steady state Mach disk is formed, then the pressure in the material in that region can be determined from the detonation velocity of the explosive. The maximum pulse duration is in general not known, but it is usually quite short. There is also a radial distribution for the maximum pressures reached. Recently Morris, McQueen, and Marsh [47] described some experiments and hydrodynamic calculations relative to formation of Mach disk in these geometries.

VI. THE LINEAR U_S-U_P RELATIONSHIP

From the examples shown in the previous sections it is apparent that the shock-wave data are adequately described by the linear U_s-U_p relationship. This was noted many years ago [14], and because the U_s vs U_p data were remarkably linear, it became common place to describe the Hugoniot loci with the equation

$$U_s = C_0 + SU_p \quad .\tag{VI.1}$$

We will often refer to this equation as the linear EOS or the linear Hugoniot. In this section C_0 is the zero-pressure intercept and S the slope. Usually S refers to entropy, but in this section we will use S for the slope to make it easier to see in the equations. C_0 is the zero-pressure shock velocity and should be equal to the zero pressure bulk sound velocity

$$C_B = \left[C_l^2 - (4/3)C_s^2\right]^{1/2} \quad .\tag{VI.2}$$

C_l and C_s are the longitudinal and shear elastic wave velocities for an isentropic material. In most instances the agreement of the shock-wave intercept, C_o, and C_B is within the experimental accuracy. Several people have investigated the appropriateness and adequacy of this simple relationship Pastine and Piacesi [48]; Ruoff [49]; and more recently, Jeanloz and Grover [50]. There is no doubt that in the absence of phase changes and nonideal behavior caused by elastic waves the description is quite good. We tested it for 19 metals by fitting the data by the method of least squares to linear and quadratic terms in Eq. (VI.1). We found that the sign of the quadratic term was plus or minus with almost equal frequency. Moreover, because of the extra degree of freedom, it was sometimes found that the sigmas for the quadratic fits were greater than for the linear.

Probably the greatest use for an EOS for materials before the development of atomic bombs was for predicting the state of the interior of the Earth. Those EOSs were based on

whatever data was available and the best scientific insight. However, most involved some type of expansion, which we know is not a very reliable method of extrapolation. Recently Jeanloz [51] compared the shock-wave EOS, Eq. (VI.1), with finite strain theory by mathematically expanding and comparing equivalent terms. He found that the Birch-Murnaghan equation, and the linear EOS, are virtually indistinguishable. He also compared Eq. (VI.1) with other EOSs. If the shock-wave EOS is not appealing to one because of the procedures required to calculate temperatures and to account for entropy, these other EOSs might be beneficial. For those interested, Jeanloz determined higher-order terms than are developed in the next section.

Without needing to fit data with various expansions, some insight to physical behavior or properties can be made by examining the coefficients C_0 and S. The first requirement is to express the Hugoniot relations Eqs. (II.37–II.43) in terms of these coefficients. The pressure, P_H, as a function of volume, V, is

$$P_H = \frac{C_0^2(V_0 - V)}{[V_0 - S(V_0 - V)]^2} \quad . \tag{VI.3}$$

Its pressure derivative with respect to V becomes

$$P_H' = \frac{dP}{dV}\bigg|_H = -C_0^2 \frac{[V_0 + S(V_0 - V)]}{[V_0 - S(V_0 - V)]^3} \quad . \tag{VI.4}$$

If we substitute the value of the compression

$$\eta = (V_0 - V)/V_0 \quad , \tag{VI.5}$$

which from the conservation of mass [Eq. (II.37)] becomes

$$\eta = U_p/U_s \quad , \tag{VI.6}$$

Eq. (VI.3) becomes

$$P_H = \frac{C_0^2 \eta}{V_0[1 - S\eta]^2} \tag{VI.7}$$

and its volume derivative

$$dP/dV\bigg|_H = P_H' = \frac{-C_0^2}{V_0^2} \frac{(1 + S\eta)}{(1 - S\eta)^3} \quad . \tag{VI.8}$$

In terms of η, the slope on the isentrope (II.73) along the Hugoniot can be written

$$\frac{dP}{dV}\bigg|_s = P_s' = -\left[1 - \frac{\rho\gamma}{2} V_0 \eta\right] \frac{C_0^2(1 + S\eta)}{V_0^2(1 - S\eta)^3} + \frac{\rho\gamma}{2} \frac{C_0^2 \eta}{V_0(1 - S\eta)^2} \quad . \tag{VI.9}$$

49

Recalling that the sound velocity $C = V(-\partial P/\partial V)_s^{1/2}$, the expression for the sound speed along the Hugoniot becomes

$$C_H = \frac{C_0(1-\eta)}{(1-S\eta)^{3/2}}\left[1 + S\eta - \frac{\gamma\eta}{(1-\eta)}\right]^{1/2} \quad . \tag{VI.10}$$

Since the sound velocities can now be determined along the Hugoniot at high pressures it is possible to calculate γ from these experimentally determined quantities. Solving for $\rho\gamma$ in Eq. (II.73) gives

$$\rho\gamma = \frac{2[P_H' - P_S']}{P_H + P_H'(V_0 - V_H)} \quad . \tag{VI.11}$$

We saw in the previous section [Eq. (V.2)] that there is a unique relationship between the sound velocity and the shock velocity, $R^* = C^L/U_s$, in the overtaking experiments used to determine the sound velocity. If we use that feature, Eq. (VI.11) becomes considerably simpler when incorporated in the linear U_s-U_p relationship. The isentropic pressure derivative becomes

$$P_s' = dP/dV\big|_s = -C^2/V^2 = -[R^*U_s/V_0]^2 \quad . \tag{VI.12}$$

In terms of C and S, the shock velocity from $P = 0$ is

$$U_s^2 = V_0 P_H/\eta = C_0^2/[1 - S\eta]^2 \quad . \tag{VI.13}$$

This term can be canceled out of all four terms of Eq. (VI.10), which becomes

$$\frac{\rho\gamma}{2} = \frac{\dfrac{-(1+S\eta)}{V_0^2(1-S\eta)} + [R^*/V_0)]^2}{\left(\dfrac{\eta}{V_0}\right) - \dfrac{V_0\eta}{V_0^2}\dfrac{(1+S\eta)}{(1-S\eta)}} \quad , \tag{VI.14}$$

or

$$\rho\gamma = \rho_0\frac{\{(1+S\eta) - R^*(1-S\eta)\}}{S\eta^2} \quad . \tag{VI.15}$$

If we look back at the first equation for γ, Eq. (VI.11), it becomes apparent that to make meaningful determination of γ one must go to higher pressure, where the difference in slopes of the Hugoniot and isentrope becomes large enough for the calculated γ's to be meaningful. Of course, it is at high pressures that we most need to know γ. A rather fortunate circumstance.

There is one more relationship we need and that is the pressure derivative of the adiabatic bulk modulus expressed in terms of the coefficients of the linear EOS. The bulk modulus, K_H is defined as

$$K_H = -V(dP/dV)_H \qquad (VI.16)$$

and we will find its pressure derivative using the definition of P'_H in Eq. (IV.4). Thus

$$\left(\frac{dK_H}{dP}\right)_H = C_o^2 \frac{V[V_o + S(V_o - V)]}{[V_o - S(V_o - V)]^3} \qquad (VI.17)$$

$$= \left(\frac{dV}{dP}\right)\frac{C_o^2}{[V_o - S(V_o - V)]^3}\left\{[V_o + S(V_o - V) - SV - 3S\frac{[V_o + S(V_o - V)]}{[V_o - S(V_o - V)]}\right\} \quad . \quad (VI.18)$$

At $P = 0$, $V = V_o$, dV/dP $C_o^2 = -V_o^2$ and $P'_H = P'_s$.

So at $P = 0$

$$\frac{dK_s}{dP_{P=0}} - V_o^3\frac{[V_o - SV_o - 3SV_o]}{V_o^3} \quad . \qquad (VI.19)$$

The zero-pressure derivative of the bulk modulus is usually defined as K'_{os}, so in terms of the Hugoniot it becomes

$$K'_{os} = 4S - 1 \quad . \qquad (VI.20)$$

K'_s is difficult for static experiments to measure, as this is basically measuring the curvature of the P-V curve. Even though the pressure range of the static experiments has increased or exceeded the pressure regime for routine shock measurements, an accompanying decrease in accuracy has prevented a better resolution of this parameter.

It would be beneficial to find some physical reasons to explain why the linear relationship (VI.1) is so good. As stated by Jeanloz [51], "A remarkable finding that has emerged from these studies is that the pressure volume relation of the Hugoniot can be expressed in a simple form for virtually all materials that have been examined. This is surprising in the sense that there is no general expression known from quantum mechanics for the energy of a condensed phase as a function of volumetric strain. As the EOS is the observation of the energy with respect to volume, the Hugoniot should be sensitive to the changes in electron densities that occur under pressure." What is more remarkable is the fact that this has been known for over thirty years. We can offer a couple of arguments for why the linear relation works so well, but nothing profound. We do note that it starts off right and heads in the correct direction. This is obvious from Eq. VI.1. It can be seen that in the P-V plane the Hugoniot (Eq. VI.4) has an asymptote, V_a, where a finite compression

results in infinite pressure. This is determined from the slope of the Hugoniot (VI.4) and is given by

$$V_a/V_o = (S-1)/S \quad . \tag{VI.21}$$

This is probably the most significant feature of the linear EOS; it not only starts right and heads in the right direction, but it also continues in the right direction. Jeanloz compiled a histogram of the frequency of the slopes in Marsh's [52] compendium of LANL's shock wave data (Fig. VI.1). This shows a bimodal distribution around $s = 1.25$ and 1.45. A cursory examination of the data does not show any significant reason for the two maxima. For example the metallic elements range from close to 1.0 to over 1.6 with some of the extremes known to be associated with phase changes. There are evidences of periodic effects, but exceptions are numerous (see Table VI.1). In Table I some slopes, S, of the elements are listed with the elements in a periodic chart. Trends can be seen going across the chart but what may be of greater interest are the values of some of the elements in the vertical columns. The slopes of the lanthanides were nicely tabulated in the work by Carter, Fritz, Marsh, and McQueen [53] Fig. VI.2. All the lanthanides examined exhibited phase changes so they [53] plotted S's for both the high and low-pressure phases. As might be expected the slopes, in general, show a trend changing slowly with atomic number going from La to Yb (except Ce). In this series the outer electronic configuration remains relatively similar. From the data plots it can be inferred that most of the transitions have little if any volume change, indicating the phase changes are of second order. Moreover, the phase changes are believed to be caused by anomalous melting. Alkali halides make up a part of the sampling and they also seem to follow the trend. There are synthetic (plastics) in the group, and although they are spread out, they have in general larger slopes. Oxides, as might be expected, tend to fall in a group with smaller slopes. The question that needs to be answered is whether V_a has any physical significance. The fact that the internal energy also approaches infinity as V_a is approached further complicates the problem. This means that increasing the shock strength in a normal material finally merely increases the internal energy and pressure without increasing the density. This also suggests that the compressed atomic volume need not be as small as one would think.

Perhaps a more reasonable meaning of V_a is that it is the volume that the electronic distribution being sampled tends to go before a major restructuring takes place. For example, the EOS of elements with relatively high electronic densities is reasonably well described by the Thomas-Fermi-Dirac models by the time the pressure reaches ~ 10 Mbar. This implies that the extrapolations referred to are not necessarily very great. Eventually the compression of these materials will be governed by the interstitial electron gas densi-

ties. The large atoms (alkali metals) still appear to be influenced by the original periodic structure at 10 Mb, and in spite of their original large compressibilities still have further to go before the T-F-D models are appropriate. Regardless of the physical significance of V_a, it is true that having a Hugoniot headed toward some asymptotic density does not cause any problems, at least when using (VI.1). Of course it was not intended that pressures be extrapolated to infinity, and as yet (VI.3) has been verified only to modest compressions.

Another interesting feature of the linear EOS is that it can also be extrapolated into the negative pressure region (Fig. VI.2). Although it cannot be extrapolated to infinite negative pressure, it is easily extrapolated to infinite volume. From the Eq. (VI.6) for η, this occurs at $U_s = 0$. Moreover, we see that at $U_s = 0$,

$$U_p = -C_o/S \quad , \tag{VI.22}$$

which tells us that the energy at $\varepsilon = 0$ is given by

$$E_c = \frac{U_p^2}{2} = \frac{1}{2}(C_o/S)^2 \quad . \tag{VI.23}$$

Rodean [54,55] discussed the meaning of this term. However, we [56] identified it as the cohesive energy when we tested it on some metallic elements in 1967. Data plots (Figs. VI.4 and VI.5) by Rodean compare measured binding energies with the $(C_o/S)^2/2$ relation for a large number of materials. The overall agreement is impressive.

As we mentioned earlier, the pressure cannot be extrapolated to minus infinity. To find the maximum tension predicted by the linear EOS, we find the critical volume, V_c, when P'_H equals zero:

$$V_c/V_o = (S+1)/S \quad . \tag{VI.24}$$

This determines the critical pressure, P_c:

$$P_c = -\rho_o C_o^2/4S \quad . \tag{VI.25}$$

For materials like W and Mo, the above equations predict ideal yield strengths greater than 0.5 Mbar. It is not very likely that these values will ever be verified. However, some dynamic tension experiments were performed on some single crystals of Cu. The results indicated that Cu supported tension waves in excess of half the yield strength (230 kbar) predicted by the previous equation.

It is debatable how much physics is involved in the above. It is well known that at equilibrium there is a balance between cohesive forces and repulsive forces no matter

53

how complicated the nature of the forces. It is also well known that the initial bulk compressibility or the sound velocity, correlates well with hardness (Moh scale), which correlates well with the cohesive energy. Thus it should be no surprise to see this term in an equation for the binding energy. The fact that slope of the Hugoniot, S, represents the net result of many interactions leading to an effective repulsive coefficient that by all evidence is effective over a very large volume is somewhat of a surprise. There has been objection to the way the linear EOS approaches $U_s = 0$. We simply note that there is ample space to bring the U_s-U_p fit back to zero pressure in any manner you please.

Two caveats must be observed in using the linear EOS and the Mie Grüneisen EOS to describe states off the Hugoniot in a hydrodynamic calculation. If the volume exceeds V_c, the sound speed will become zero or negative and most calculations will become unstable, because there is no communication between adjacent zones. If the compression exceeds that predicted by V_a, there will simply be no EOS prescribed. There is very little chance for this to happen if S is close to one. However, for plastics and other materials that have large S's, this can easily happen.

Whether the EOS in the negative pressure regime actually follows that locus will probably never be known. We do not believe the linear relationship is precise or that the two cited extrapolations are really meaningful. What we do believe is that the linear relationship has the characteristics to fit shock-wave data; hence when deviations are observed — discontinuities, change in slope, whatever, — the chances are good that some type of phase change has or is occurring. The U_s-U_p Hugoniot for an initially porous material is always concave downward, with most of the curvature in the low-pressure region. If the data are fitted so that the upper segment is linear, there should be no problem. Or one could simply transpose the data to a Hugoniot centered at crystal density and find its linear EOS; or one could just run the metastable Hugoniot curve and let the calculator find the zero porosity Hugoniot (Sec. III). We recall that because the shock velocity is in essence a differential measurement, it is sensitive to changes in slope in the P-ρ plane. One final remark: if a quadratic term is included in the U_s-U_p EOS, even modest extrapolations can cause unrealistic things to occur.

VII. THE SPECIFIC HEAT AND THE GRÜNEISEN PARAMETER

It is sometimes of interest and sometimes important to know the temperature of shocked-compressed materials. In geophysics, for example, temperatures of shocked mate-

rials and/or temperatures of isentropes are of considerable interest in inferring the probable temperature distribution of the Earth. Melting at high pressure of course is a temperature-related phenomenon, as are many thermodynamic functions, e.g., the Gibbs free energy, required when the locations of phase boundaries are to be calculated. As one would expect, both the specific heat and Grüneisen parameters are required to make these calculations (Eqs. III.11–III.18). Fortunately, the behavior of these parameters can be predicted satisfactorily for most materials at atmospheric pressure by statistical mechanics. The volume dependence of these functions is ordinarily determined by measurements at different temperatures. The assumption that the specific heat and gamma are functions of volume only has been used routinely in high-pressure applications at modest temperatures. Shock-wave studies have been used to verify some of these assumptions and will be mentioned later in this section. The two most obvious quantities to measure to show how specific heat and gamma vary at high pressure are the temperature, by measuring thermal radiation, and the sound velocities, by measuring overtaking wave velocities. Some results of shock-wave studies of this nature and some from measurements on porous materials are presented.

The Los Alamos group reported a large amount of experimental data [17], and to make the EOS as useful as possible they calculated and reported temperatures along the Hugoniots, at the foot of the pressure-release isentropes, and the P-V locus of the zero Kelvin isentrope. They wished to make these calculated quantities as accurate as possible. This meant describing the specific heat as well as reasonably possible, without expending the large amount of effort that would be required to incorporate all the data available.

For many solids, an adequate representation of the specific heat can be obtained from one of the simplest forms of the Debye theory. The form used by the Los Alamos group was characterized by a single Debye theta, $\Theta(V)$, which is a function only of volume. The thermal energy $E_T = E - E_K$, where E_K is the energy of the solid at $T = 0$ K and the same volume, is given by

$$E_T = 3nkTD_3(x) \tag{VII.1}$$

$$D_3(x) = \frac{2}{x^3} \int_0^x \frac{z^3 dz}{e^z - 1} \quad . \tag{VII.2}$$

Here, n is the number of atoms per gram, k is Boltzmann's constant and $x = \Theta/T$. The specific heat and the entropy are given by

$$C_V = 3nk\left[4\,D_3(x) - 3x/(e^x - 1)\right] \tag{VII.3}$$

and

$$S = 3nk\left[\frac{4}{3}D_3(x) - \ln(1 - e^{-x})\right] \quad . \tag{VII.4}$$

This form for the specific heat is consistent with the assumption that the Grüneisen parameter depends only on the volume, since it can be seen from Eqs. (VII.3) and (VII.4) that the specific heat depends only on the entropy. They used these thermal equations to approximate the specific heat. They chose Θ so that Eq. (VII.3) would give the correct room-temperature zero-pressure value for the specific heat.

For some materials, neither C_V nor n was available, so they used the approximation

$$k\Theta = \hbar c_o (6\pi^2 n\rho)^{1/3} \quad . \tag{VII.5}$$

In the cases where C_V was known but n was uncertain, they used $n \approx C_V/3k$, provided that the sound speed and density were low enough to expect a low Debye theta.

This simplified choice for the specific heat does not represent the detailed behavior of the specific heat of most materials, particularly at high temperatures. The electronic contribution to the specific heat, important for metals at high temperatures, and the anharmonic contribution of the lattice vibrations to the specific heat (linearly increasing with temperature) are not taken fully into account. The optical modes for some of these solids could be better represented by an Einstein theta, Θ_E. The choice of specific heat used does two important things. It gives a reasonable way to determine the initial density of the zero-Kelvin isentrope at zero pressure. It also assures that the calculated temperatures at modest pressures are as accurate as can reasonably be expected. The error in the $P_K(V)$ curve produced by the inaccuracy in C_V is probably less than or comparable to the uncertainty in the Hugoniot curve at modest pressures. All the zero-Kelvin isentropes calculated from Hugoniots in the high-pressure/high-temperature region have large uncertainties caused by lack of knowledge of gamma. For metals the increasing contribution of the electrons to the specific heat at high temperatures invalidates the assumption that the Grüneisen gamma is a function only of volume.

Referring to supplemental calculations (Sec. III) it was shown that isentropes can be calculated directly from the Hugoniot (III.5). If one extrapolates the Hugoniot a bit to negative pressures, a pressure-release isentrope from some point on the Hugoniot can be calculated to zero pressure. One could then use the procedures outlined in this section to determine what the temperature should be along this isentrope, using (III.17). This procedure has been used [12], except that instead of extrapolating the Hugoniot, the locations of the isentropes at $P = 0$ were successively tied to an energy-volume locus determined from experimental specific heat and thermal expansion data. These zero-

pressure energy-volume loci are not usually available and must be compiled, which in light of uncertainties in gamma, makes some of the simple approximations more appealing.

When the pressure becomes quite high, a more accurate characterization for the specific heat would be the following:

$$C_V = D(T) + b_e(p/po)\gamma_e T \quad , \tag{VII.6}$$

where $D(T)$ is the Debye function, b_e is proportional to the density for electrons at the Fermi level at STP, and γ_e is the electronic Grüneisen parameter.

Some Comments on the Grüneisen Parameter

It could be seen throughout the first sections that all states off the measured Hugoniot required the use of the Grüneisen parameter, γ, in the calculations. Temperature calculations along isentropes also required it, as well as along Hugoniots where the specific heat is also required. The early work by Grüneisen in 1912 [57], and more conveniently Grüneisen [58] established the fundamental concepts of why this theoretical or thermodynamic parameter has the properties it does. Space does not permit a complete review of this subject, and for further reading the work by Slater [59], Seitz [60], and Born and Huang [61] is recommended. Let it suffice to say there are theoretical reasons to justify γ being independent of pressure, at least in the working range of most of these experiments. One of the basic results from these studies is that γ is a function of volume only. To our knowledge this has really never been tested, since γ has never been measured at two temperatures at the same density.

These studies show how closely gamma and the specific heat are related. In fact, from Eqs. VII.4 and VII.5 above and a slightly rewritten Eq. (III.11),

$$dT/T = -\gamma dV/V + dS/C_V \quad , \tag{VII.7}$$

the usual function for γ is obtained:

$$d \ln \Theta / d \ln V = -\gamma \quad . \tag{VII.8}$$

The definition of the Grüneisen parameter, γ, given at the beginning of Sec. III, was adequate for the applications there. However, it does not establish its numerical value. In terms of measurable thermodynamic variables at zero pressure,

$$\gamma = V(dP/dE)_V = \frac{c_o^2 \alpha}{V_o C_V} \quad , \tag{VII.9}$$

where α is the volume coefficient of thermal expansion. At standard conditions for many materials γ is about two. Of the three parameters defining γ, two are rather difficult to measure, so values of γ_0 are in many instances accurate only within a few percent.

We have referred to γ and the Mie Grüneisen EOS. The origin of these lies in statistical mechanics. For a metallic crystals it is assumed that the thermal energy can be described as the sum of the energies of a set of simple harmonic oscillators whose frequencies, ν_α, are functions of volume only. The internal energy of the system is given by the sum of the potential energy, $\phi(V)$, of the cold lattice and the summation of the normal modes, 3N, of the N atoms. Thus the energy is given by

$$E = \phi(V) + \sum_{\alpha=1}^{3N} \left[\frac{h\nu_\alpha}{2} + \frac{h\nu_\alpha}{e^{h\nu_\alpha/RT} - 1} \right] \quad , \qquad \text{(VII.10)}$$

and the Helmholtz free energy by

$$A = \phi(V) + \sum_{\alpha=1} h\nu_\alpha/2 + kT \sum_{\alpha=1}^{3N} \ln\left(1 - e^{-h\nu_\alpha/kT}\right) \quad . \qquad \text{(VII.11)}$$

The volume derivative of A gives the pressure:

$$P = -\left(\frac{\partial A}{\partial V}\right)_T = -\frac{d\phi}{dV} + \frac{1}{V} \sum_{\alpha=1}^{3N} \gamma_\alpha \left[\frac{h\nu_\alpha}{2} + \frac{h\nu_\alpha}{e^{h\nu_\alpha/kT} - 1} \right] \quad , \qquad \text{(VII.12)}$$

where γ_α was defined as the logarithmic volume derivative of the frequencies

$$\gamma_\alpha = -\frac{d\ln\nu_\alpha}{d\ln V} \quad . \qquad \text{(VII.13)}$$

On the assumption that the frequencies of all the normal modes change proportionally the same with volume, the γ_α's can be taken out of the summation and the subscript removed, and VII.12 gives the Mie Grüneisen EOS:

$$P = -\frac{\partial\phi}{\partial V} + \frac{\gamma}{V} E_{vib} \quad . \qquad \text{(VII.14)}$$

Similar results can be obtained in the high-temperature classical limit, where the energy of each oscillator approaches kT; VII.12 then becomes

$$P - P_K = \frac{3NkT}{V} \left[\frac{1}{3N} \sum_{\alpha=1}^{3N} \gamma_\alpha \right] \quad , \qquad \text{(VII.15)}$$

where γ is now an average value of logarithmic derivatives.

Several efforts have been made to find a functional form for γ using various assumptions concerning the vibrational spectra, etc. Slater [59] assumed an isotropic body and a constant Poisson's ratio. Using the relationships for the isentropic values for the longitudinal and transverse sound velocities, he obtained the result that

$$\gamma_i = d\ln\nu_i/d\ln V \qquad \text{(VII.16)}$$

are equal for all modes of vibration. Further work leads to the Slater formula

$$\gamma = -\frac{V}{2}\frac{(\partial^2 P/\partial V^2)}{(\partial P/\partial V)} - \frac{2}{3} \quad . \qquad \text{(VII.17)}$$

Dugdale and MacDonald [63] proposed that the constant term in the Slater relation be changed from −2/3 to −1/3. Their result came in part from the assumption that for a Hooke's law EOS for the interaction forces, the thermal expansion is zero. It was argued that the last assumption was incorrect. Rice [14] used the basic assumption that the potential energy of a cubic crystal lattice is some function of the Cartesian coordinates. They also assume that the spatial derivatives of the potential all change in at the same rate with volume. The force constants govern the amplitude of the thermal vibrations. This leads to the conclusion that these are equivalent to the equivalent set of harmonic oscillators. With further work they arrived at the Dugdale-MacDonald relationship. Another development, called the free volume model, gives a similar result with the constant coefficient of VII.17 equal to one. It seems appropriate to write the equation for γ based on the various assumptions as

$$\gamma_i = \frac{V}{2}\frac{d^2(PV^{2/3})/dV^2}{d(PV^{2/3})/dV} - \frac{\kappa}{3} \quad . \qquad \text{(VII.18)}$$

The above equation can be solved for a linear EOS, in the same manner as was done in Sec. VI. After a considerable amount of differentiation and algebra an equation is obtained for the zero pressure value of γ.

$$\gamma_o = 2S - \kappa \quad . \qquad \text{(VII.19)}$$

Since S can be measured reasonably well for many materials, a simple test of the various models can be made by using the measured γ_o's and S's and solving for κ in VII.17. The κ's examined by Rice have values centered around 1 ± 0.4. The fact that the results are in good agreement with the models is probably fortuitous. The overall functional form of the

equation probably lies in the assumption that the frequencies of the normal modes change at approximately the same rate with volume. As appealing as it is, such simplification is hardly justified, considering all the approximations involved.

If one has fondness for these models and believes a better description of the zero Kelvin isentrope can be made using them, it is suggested that κ in the previous equation be satisfied by the thermodynamic γ, Eq. (VII.10) and the slope S. It is then possible to solve for the zero-Kelvin isentrope with VII.18 and the difference equation, III.5. In order to solve the equation it is necessary to start the calculation with the correct volume derivative for γ. This can be obtained in terms of S, and it is given by

$$d\gamma/dV = \left[S^2 - S/3 + 5/9\right]/V_o \qquad (VII.20)$$

when $\kappa = 1$. The result of such a calculation is shown later for Cu where $\kappa = 1$.

Gammas From Porous Materials

In Sec. III it was shown how γ could be obtained from shock-loading porous materials. Probably the largest effort to measure γ this way was reported in Kinslow [17]. Data were reported on porous Cu, Fe, and 2024 Al. We have reproduced some of their results for Cu in Figs. VII.1–VII.3. The experimental design shown in Fig. V.13 was used, which enabled them to measure the shock velocities in six samples in each experiment. They used the EOS of Cu to determine the associated particle velocity with the impedance-match technique. One objection in doing these experiments to determine γ is that a value for γ had to be assumed to calculate the isentropes for the impedance-match solution. Since the final results were compatible with the γ's used, the objection automatically disappeared. The densities of the Cu samples were 89, 76, 60, and 43 percent of the crystal density. Steel shims were used under all the flash blocks to minimize errors in calculating velocities for the gap closure times. The closure times were calculated through an iterative procedure that ensured that these times were calculated as accurately as possible. The shock-particle velocity data (Fig. 1) have considerably more scatter than usual because the samples did not have uniform density. There are solid curves that go through each of the data sets. These are Hugoniots calculated from the crystal density Hugoniot and gamma determined from the relationship, $\rho\gamma = 17.8$, determined from the STP values. It was planned to use various forms for gamma and to minimize the difference between the calculated and the experimental points. It is clear that such a refined treatment is not justified and in general the $\rho_o\gamma_o$ formulation is fairly good except at the upper end of the 0.8 density Hugoniot. A quadratic fit of the U_s-U_p data was obtained for each density group by the method of

least squares. Average values of $(\rho\gamma)^{-1}$ were calculated at constant volume from these fits and the crystal density Hugoniot. These values are plotted with various types of lines in Fig. (VII.3) and in Fig. (VII.4) for Fe. In addition to these curves, the value of each γ calculated from the crystal density Hugoniot and the P-V point are plotted. Most of the calculated γ's lie around the value of $dE/dP = (\rho\gamma)^{-1} = 0.056$ cm^3/g, so it comes as no surprise that the calculated curves in the previous figures agree so well with the data. As mentioned earlier in this section, the Dugdale-MacDonald relationship was used to calculate the zero-Kelvin curve and the volume dependence of γ for Cu. This form was chosen because $\gamma_0 = 2S - 1$ for Cu. This curve is obviously also in good agreement with the data in the $\rho_0\gamma_0$ plot, but the $\rho_0\gamma_0$ constant curve agrees even better. From these studies it was concluded that if no other data preclude it, that a constant $\rho\gamma$ is adequate.

It was shown earlier, Sec. III, that the above (VII.21) was adequate when their standards were cross-checked. Sound-velocity measurements in shocked 2024 Aℓ [64] also indicate that (III.10) is a good approximation, but that it might possibly be refined with better experimental data.

When deriving γ's from the measured ΔE's and ΔP's, on porous samples quite often the states along the crystal density Hugoniot and the porous Hugoniot are not in the same phase. Clearly, states on the porous Hugoniot will be melted and/or vaporized before those on the crystal density Hugoniot, and there seem little doubt that the latter will melt somewhere in the experimental range.

The question has been asked why γ is not taken as constant instead of using $\rho\gamma$. The answer is that it does not have the correct form and at large compression it produces isentropes concave downward. Taking γ as constant will result in zero or negative sound velocities at high pressure. From the equation for the sound velocity on the Hugoniot (VI.10) it can be found that the sound speed becomes zero when

$$\eta = \frac{S - 1 - \gamma + [(\gamma + 1 - S)^2 + 4S]^{1/2}}{2S} \qquad (VII.21)$$

For Cu, with $S = 1.5$ and $\gamma = 2$, the sound velocity becomes zero at $\eta = 0.56$, but major difficulties become apparent before that. A dashed line on Fig. VII.4 corresponds to $\gamma = 2$. The data lie above this line except near the origin.

A feature seen in U_s-U_p plots of data on porous materials is that for a modest amount of porosity $\sim 10\%$ there is a lot of downward curvature in the low-pressure regime. The amount of this downward curvature becomes less with increasing porosity. The Hugoniot

becoming nearly linear for porosity near 50%. This behavior can be explained in a qualitative manner by referring to the figure (III.4) of the P-V loci of the porous and crystal density Hugoniot. There is a dashed line indicating the Hugoniot locus. It was drawn above the axis from its origin to V_x as a manifestation of the material rigidity and as such represented a crush or collapse curve. If one assumed that the porous material were ideally distended and existed at V_o-P_o in a metastable state and was then shocked, it would not follow the Hugoniot indicated by the dashed line. Instead it would go below the $P = 0$ line and cross it at the crystal-density volume. This is the solution if the problem were solved by application of Eq. (III.8) for calculating recentered Hugoniots. This curve would then run into the dashed curve at higher pressure. The salient feature illustrated, is that the Hugoniot for the porous material will head toward the origin of the crystal density Hugoniot, and from the shock-wave conservation relationship this also means the origin in the U_s-U_p plane. Thus all those curves drawn in Fig. II.1 are more or less trying to head toward zero. Examination of the P-V/V_o loci, Fig. VII.2, shows that their curvature becomes less with increasing porosity, moreover, their slopes at high pressure also become steeper.

When derivatives become zero or infinite simplifications sometime occur in related equations. We have already seen, Eq. (VI.16), that for a linear EOS, when

$$\eta_a = 1/S \quad . \tag{VII.22}$$

P_h' becomes infinite at an asymptotic volume, V_a, determined by the slope S. Looking further we see from (VI.11) that γ is also determined, and it is given by

$$\gamma_a = 2V_a/(V_o - V_a) \quad . \tag{VII.23}$$

It should be noted that this result does not depend on the Hugoniot having the linear EOS. Anywhere P_H' becomes infinite, gamma is determined. Gamma can also be written in terms of the slope and from (VII.24) and (VII.25). It is given by

$$\gamma_a = 2(S_a - 1) \quad . \tag{VII.24}$$

For completeness the inverse of the previous two equations are

$$V_a/V = \gamma(\gamma + 2) \tag{VII.25}$$

and

$$S_a = (\gamma + 2)/2 \quad . \tag{VII.26}$$

From (VII.24) we see that anywhere the slope, S_a, of a U_s-U_p Hugoniot satisfies the relationship

$$S_a = U_s/U_p \qquad\qquad (VII.29)$$

P'_h becomes infinite. This just gives a class of linear EOS's where C_o is zero. These Hugoniots are simply straight lines from the origin and represent isovolume curves in P-V space.

The Los Alamos group [17] offered a little test on this concept of γ. They proposed that if γ is indeed only a function of volume, then there should exist a Hugoniot whose asymptote occurs at crystal density (that is one of the family of Hugoniots of porous materials that should ideally be heading toward $V_{crystal}$) with an intercept, $C_o = 0$, and a slope given by (VII.27). They used the STP values for γ for the three materials they investigated. The percent porosities that satisfied these criteria were 50, 49, and 46% for Al, Cu, and Fe, respectively with corresponding slopes of 2.00, 1.98, and 1.85. Even though there is a lot of scatter in the data, the overall agreement is good.

It could be asked of what use is the little exercise just described, since the gamma was already known at $V_{crystal}$. The answer is that the exercise has demonstrated a concept. Moreover, if the samples had been of higher quality perhaps the data would have been good enough to establish whether or not the appropriate U_s-U_p Hugoniot was indeed linear or not. In either case, knowledge of the behavior of this fundamental parameter would have been obtained in a energy-density regime quite inaccessible by other techniques. The experiment is not restricted to the particular amount of porosity specified by the STP value for γ_x to determine a γ_a. Any place in the P-V phase where the P'_H is vertical determines γ_a and also the pressure where it occurs. The requirement is that the porosity be great enough so these conditions can be accessed. Just a closing comment, measuring the density well of these very porous material is as difficult as measuring their Hugoniots.

Gammas From Overtake Measurements

The principles and techniques for determining gammas by the rarefaction overtake technique were described in Secs. III and V. Shock-wave physicists have been aware of the possibility of doing this probably before shock-wave physics was considered a science, as the overtake criteria was also a design criteria for making shock-wave measurements. Al'tshuler [65,66] recognized the importance of such measurements and he performed a series of over 20 experiments to determine the sound velocity at one pressure point. The

overtake position can be located quite well with the optical analyzer technique. At high pressure, or what is more important, when P'_H becomes fairly steep, it should be possible to measure gamma to better than 10%, if elastic-plastic flow does not make it difficult to decide exactly where the bulk sound wave is. The first overtake wave detected can be measured with a precision comparable to the shock-wave velocity. Consequently some investigators have not reported on the value of gamma until they reach the melting point. To date, what is usually done is to plot the derived sound velocity and compare them to those calculated with the $\rho_0\gamma_0$ constant value. This seems to suffice, for example see Fig. VII.5 [67]. To date the following elements, C, Al, Fe, Mo, Ta, W, and Pb have been investigated. Of almost equal importance, the experiments also enable one to determine where melting occurs or at least where the system no longer supports a simple longitudinal wave. The precise location depends on how close the experimental points bracket this position. On occasion it appears that measurements have actually been made in the mixed phase region.

VIII. EARTH MODEL BASED ON A HUGONIOT EOS

We owe much of our current knowledge of the state of the Earth's deep interior to data obtained from shock-wave measurements. The fact that the accurate measurement of two quantities, the shock velocity and the associated shock particle velocity, when coupled with the conservation equations of mass, momentum, and energy, enable us to determine the pressure, density, and internal energy states of materials at conditions existing throughout the interior of the Earth. It is also interesting that the temperatures existing through the Earth must be quite comparable to those existing behind strong shock waves at comparable densities and pressures. If one considers a simplistic Earth creation scenario, accretion of material by impact and associated heating by the collision process, followed by the subsequent compression heating as more and more material is accumulated, it is easy to see that the temperature distributions through the earth must be near to the temperature on the Hugoniot but with a smaller pressure gradient. It is also important to remember that almost all apparatuses measuring static pressures above ~10 GPa has been calibrated from shock-wave data.

A serious weakness in the shock-wave experiments is the lack of knowledge of the state of the material while under compression, or whether is is in equilibrium. Except for some very limited flash x-ray work by Johnson and Mitchell, 1970 [68] one can only surmise what the crystal structure is. However, static presses are now capable of reaching megabar

pressures, so some of those questions have now at least been partially answered. The static experiment can be made on any time scale desired, while the time scale of the shock-wave experiments is predetermined. However, since shock velocities are measured, the results are essentially differential measurements. Because they are reasonably well measured, we are able to determine the pressure derivative of the compressibility, K', a quantity that can not be determined well from high-pressure static experiments.

To our knowledge the first shock-wave data on geological materials to appear in the literature was by Hughes and McQueen, 1958 [69]. By the end of the sixties, a considerable amount of data was available. Figures VIII.1–VIII.2 are typical records for minerals most likely to be in the deep mantle. Even though the time scale of the measurements was often less than a microsecond, it was apparent that silicate type minerals were undergoing high-pressure phase changes to much more compact structures. This verified Birch's 1952 predictions [70] that the materials making up the Earth's mantle must undergo phase changes to higher-density, more close-packed structures. Aft the appearance of the shock-wave data, many different investigators tried to use the data to formulate an EOS for the high-pressure phase of high-density materials evidenced from shock-wave measurements; that is, the EOS for the material if they existed at standard conditions but in a metastable state (see Sec. III). Unfortunately, most of that work was based on EOS formalisms that were not really amenable to ext. polation. That is, they simply did not work (see Jeanloz [51]). Also contributing to the problem is the fact that the pressure-density range covered by the shock-wave data above the phase changes is quite small. This meant that data of the very highest quality was required to perform that type of calculation with meaningful results, even though a proper form of the EOS was used.

Although it was apparent that the high-density phases of silicates with various amounts of Fe, Mg, Al, etc., could satisfy any desired Earth model for the mantle, the actual composition was not determinable (Fig. VIII.3). The following papers are representative of the shock-wave data of mantle minerals [71–74]. Even earlier it was shown that Fe alloyed or mixed with small percentages (10–20) of lighter elements would satisfy the density requirements for the composition of the Earth's core. Balchan and Cowan, 1966 [75]. Hugoniot data on Fe-Ni alloys by McQueen and Marsh, 1966 [77] eliminated forever the romantic notion that the core was probably composed primarily of an iron-nickel alloy like the iron meteorites.

In 1964 there were two papers published on the constitution of the Earth, Birch

[78] and ours [79]. The results were in surprisingly good agreement even though the calculational procedures were quite different. The main feature of our calculations was that the Williamson-Adams procedure [79] was not used and no pressure-density distribution was assumed. The linear U_s-U_p EOS was used to determine the density distribution of the Earth, which in turn determined the coefficients of linear EOS for the various regions of the earth. In addition to the linear Hugoniot fit required to perform these calculations, it was necessary to assume a Grüneisen γ, a specific heat, and a temperature distribution, since corrections were made for the difference in the temperatures on the Hugoniot and the temperatures through the Earth. Uncertainties in the derived EOS due to the last three parameters were small and will be discussed later. Because of the interesting results obtained from these calculations, the procedures used for making them are outlined below.

Starting with the linear U_s-U_p curve, the pressure on the Hugoniot is given as a function of density, and the temperature on the Hugoniot is determined by application of Eq. (III.20). Since the temperature of the Hugoniot is not necessarily the same as the temperature of the Earth at a given density, a pressure correction, ΔP, can be calculated from the relationship

$$\Delta P = \Delta T (\partial P / \partial T)_V = \rho \gamma C v / \Delta T \quad , \tag{VIII.1}$$

where ΔT is the temperature difference. The other thermodynamic parameter required for the Earth calculation is the local sound velocity, $(\partial P / \partial \rho)_s$, which is calculated from Eq. (VI.10).

The pressure in the Earth is found by integrating Poisson's gravitational equation

$$P_\bullet = \int^R g(r) \rho(r) dr \quad . \tag{VIII.2}$$

Using the notation $i - 1/2$ and $i + 1/2$ for the boundaries of the ith zone, the following difference equations are used for integrating the various parameters for the Earth: the pressure in the Earth

$$(Pe)_{i-1/2} = (Pe)_{i-1/2} + g_i \rho_i (r_{i-1/2} - r_{i+1/2}) \quad , \tag{VIII.3}$$

the gravitational acceleration

$$g_{i+1/2} = G \left[M - \sum_{i-1}^{i} m_i \right] / (r_{i+1/2})^2 \quad , \tag{VIII.4}$$

the incremental masses

$$m_i = (4/3)\pi\rho_i\left[r^3_{i-1/2} - r^3_{i+1/2}\right] \quad , \tag{VIII.5}$$

and the moment of inertia

$$I_{i+1/2} = \frac{2}{3}\sum_{i=1}^{i} m_i r_i^2 \quad . \tag{VIII.6}$$

In the above, quantities computed on boundaries but needed at midpoints are found by averaging.

The density used in these equations is found by an iterative process that determines an EOS that gives not only the correct seismic velocity but also the correct pressure. This is found by interpolating between two trial equation of states using some percentage or fraction. For this fraction, a density is first found that gives a sound speed that agrees with the seismic velocity. This density is used in the previous equations to compute the pressure in the Earth, which is then compared with that determined from the EOS. By successive iterations a fraction is found that brings the pressure in the Earth into agreement with the EOS pressure. The calculation is then advanced to the next zone. The interpolation was usually made between EOSs that differed only in either the sound speed coefficient, C_o, or the slope, s, the remaining parameters being the same for both trials.

Although this procedure gives an EOS that satisfies the seismic velocities and gravitational equations, it does not at this stage necessarily give a unique EOS in C_o and s. The next step in the iteration procedure is to transform the calculated P-ρ Hugoniot points to U_s-U_p and compare these with the trial Hugoniot curves. It was found that variations in the trial EOSs change the calculated U_s-U_p curves in a predictable manner. Thus it was possible to find trial EOSs that agreed with calculated U_s-U_p Hugoniots. For the B, D, and E regions it was found that a linear U_s-U_p Hugoniot could be found for each (see Figs VIII.5-VIII.9).

In applying the above procedures it is necessary to divide the Earth into the usual seismic regions. Since there are really only three parameters that one can use to restrain or restrict what the composition of the Earth might be, the radius, the mass, and moment of inertia, in addition to the seismic data, it is not possible to solve the Earth's density distribution uniquely for all the regions. Thus, in some regions, some compromises were made:

1) The outer crust was taken to be ~10-km thick with a density of 1.8 g/cm^3, underlaid by a second 10-km layer with a density of 3.0 g/cm^3.

67

2) The STP density, ρ_{oB}, of the B region was specified. This is a very critical parameter, and at the time these calculations were made, it was not well known.

3) The C region was found by interpolating from the inside of the B region to the outside of the D region. This was necessary so that the mass in the transition region could be calculated.

4) The EOS of the D region was fully determined by the calculational procedure, and no compromise was required.

5) The D' region, now called the D" region, was assumed to be a transition region between D and E and was treated like the C region. There has been some speculation that the leveling off of the sound velocity is due to partial melting of the mantle, which would imply that the rate of increase of density might decrease. However, the accepted value of the core mantle radius of the Earth is now 3486 km, which is ~13-km larger than the value used in our calculations. Thus by our interpolation procedure the density in this region was partially compensated.

6) The F and G regions were assumed to be extensions of the E region in the sense that the seismic data for F were extrapolated into E. Since the two determining parameters, the mass and moment of inertia, were already used, it was not possible to include these regions separately. Moreover, the seismic data for the inner core were certainly not very good at that time It would have been possible to arbitrarily increase the density of the G region by a small amount, but since there is so little change in density at these pressures for a liquid-solid transition, and so little mass involved, this was not done. The code for doing these calculation was already complicated.

The following paragraph summarizes the iteration procedure used in these calculations:

1) A density was found that gave the correct sound velocity for a particular zone. A zone was one of the one-hundred sections of equal radii into which the Earth was divided, except at "regional" boundaries.

2) The fractional composition between two trial EOSs was then found that made the EOS's pressure equal to the Earth pressure.

3) An EOS was determined for each region, not in transition regions, that satisfied the requirement for assumed uniform composition.

4) The initial density of the core was adjusted to give the correct mass of the Earth.

5) The initial density of the lower mantle EOS was varied to give the correct moment of inertia of the Earth.

6) For each iteration above, all the preceeding iterations were always satisfied.

The results of a series of calculations done with variations of parameters considered not to be well known is presented in the following table.

Free Oscillation Calculations and The Earth Hugoniot

At the time of writing [78] there was no actual way of determining the density at the outside of the B region. This is a very important constraint, as mentioned by Birch and by us. We used values of 3.2, 3.4, and 3.6 g/cm³ for the STP density of the B region. All but two other problems were run with a density of 3.4 g/cm³, since we assumed this density was probably the closest approximation to the actual value. The free oscillation data have been used in many Earth calculations in the subsequent years. In particular the Earth models B1 1066A and 1066B by Gilbert and Dziewonski, 1975 [80] and C2, Anderson and Hart, 1976 [81] have received considerable attention. With respect to the present discussion, these models do, among other things, put strong constraints on the density of the outer region of the B region.

Another Earth model by Dziewonski and Anderson, 1981 that has received considerable attention is PREM [82], an acronym for "Preliminary Earth Model." Except for some character in the transition region, this model has essentially the same density distribution as the other models cited.

It was stated earlier the largest uncertainty in our calculations was caused by lack of knowledge of the STP density of the B region. It is now possible to eliminate this uncertainty with the help of the 1975 Earth models, and to correct the Hugoniot EOS of the Earth, EH. The current best estimate of ρ_{oB} is 3.34 g/cm^3.

In Table II are the calculated values of the U_s-U_p Hugoniot parameters of the mantle D and core E for an assumed set of thermodynamic parameters. The most important feature of the numbers in Table II is that if the assumed density of the B region is not correct, then the derived densities and sound velocities for the core are wrong by about half as much and in the same direction; the mantle parameters also change by about the same percentage but in the other direction.

Table II. Derived EOS constants for Regions D and E for the listed values of the assumed thermodynamic parameters and their sensitivity to a ten percent change in these parameters. These are for an assumed temperature at the D-D′ boundary of 3000 K.

	Assumed	$\rho_{oB} = 3.34$ g/cm^3	$\gamma_o = 1.25$	$C_v = 1 \times 10^7$ egr/gK
	$\rho = 4.09$ g/cm^3	−6.0%	+1.0%	+0.1%
D	$C_o = 7.39$ km/s	−7.0%	−0.3%	+0.4%
	S = 1.25	−	1.0%	−
		$\rho_{oB} = 3.34$	$\gamma_o = 1.5$	$C_v = 0.75$ egr/gK
	$\rho = 7.22$ g/cm^2	+5.0%	+2.0%	+1.0%
E	$C_o = 5.03$ km/s	+5.0%	−0.3%	+0.3%
	S = 1.32	−	1.0%	--

The C_o and S calculated for the B region, using the parameters listed in Table II, are $C_o = 6$ km/s and S = 1.46. The sound velocity and slope are not unrealistic for likely outer mantle materials, but these values were obtained in a very speculative manner, especially because of the uncertainties in the temperature gradient and seismic data.

There are currently no universally accepted temperature distributions of the core, but most are more than 1000-K higher than those used in our earlier work. To enable anyone to make temperature corrections on our derived EOS parameters, the values in Table III should be reasonable estimates for the percentage change for a 500 K increase at 3000 K at the D-D′ interface.

70

Table III. Percentage change from an assumed temperature of 3000 K at the D-D' interface for a 500-K increase in temperature.

	ρo	C_o	S
D	+0.5%	+0.2%	+0.5%
E	+0.3%	+0.1%	+0.5%

It is not surprising that these parameters are so insensitive to assumed temperature distributions. This reflects on the inverse problem of trying to use EOS data to determine temperature distributions.

Some Summary Remarks on the Earth Hugoniot of State

Nothing much has changed since our earlier work using the linear U_s-U_p EOS to calculate the density-pressure distributions through the Earth. However, by using distributions that use the free oscillation data, a very close constraint can be imposed on the zero-pressure density of the B region, which in turn restricts the EOS parameters describing the lower mantle and outer core. Because of the small number of parameters describing the Hugoniot EOS, the initial densities were and are are in essence hinge points. These densities were determined by the mass and moment of inertia constraints, and were not after the fact extrapolations of calculated density distributions for the various regions. The zero-pressure sound speed determined with this procedure is also very closely associated with the seismic and mass and inertia constraints and it is essential in satisfying the seismic data. To our knowledge the procedures outlined here are the only ones where the density distributions and EOS are calculated simultaneously in a completely consistent fashion.

One thing emerges is the fact that the slope, S, of these derived Hugoniots appears to be quite well determined. It can be seen that for all reasonable variations in any of the thermodynamic variables, the slope, S, of the derived metastable Hugoniots of the lower mantle and the outer core are very insensitive. This is somewhat paradoxical, in that K'_o or S are the least well determined parameters calculated from all the various shock-wave data inversion techniques used to estimate metastable EOSs. Moreover, K'_o is usually determined to less than 20% from static high-pressure measurements for materials that do not even exhibit a phase change. Since the slopes appear to be so well determined for both

the inner mantle and outer core, it would seem appropriate when calculating metastable Hugoniots that are to be compared with Earth models, that these values of K_0' or S be used as constraints. Thus if the other two derived parameters, ρ_o and C_o, for a material do not agree with the values calculated for the Earth, then that material can be considered not to be a likely Earth constituent.

Composition of the Mantle

From the results of the work just described, we believe the EOS of the material comprising the inner mantle must have an EOS that falls within the limits

$$U_s = 7.4 \pm 0.2 + (1.25 \pm 0.01)\, U_p \quad , \tag{VIII.7}$$

with a zero-pressure density

$$\rho_{om} = 4.1 \pm 0.05 \; gm/cm^3 \quad . \tag{VIII.8}$$

Now one needs only is find materials that meet these criteria and a few other restrictions, e.g., they must be oxides or silicate-like compounds. It could be seen in Fig. VIII.3 that there are many materials and combinations of materials that fall in the correct pressure-density regime, but we know much more about the mantle than that. The problem is complicated by the fact that most of the candidate materials have undergone phase changes. A group of rocks and minerals were compared with the Earth EOS (Fig. VIII.4). Here the calculated density and the C_o's were plotted for various assumed S values. From the results one can clearly eliminate most from further considerations as mantle constituents. Two minerals:

$$Olivine = (Mg,Fe)_2SiO_4$$

$$Bronzite = (Mg,Fe)SiO_3$$
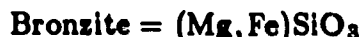
have nearly the type of EOS required for mantle constituents. They also have very nearly identical Hugoniots (Fig. VIII.10). Their density and bulk sound velocity both are just outside the range where we believe the Earth EOS should be. To proceed further we refer to an old plot of Birch's law (Fig. VIII.11), which basically states that the sound velocity is a linear function of density for oxides and silicates with the same mean molecular weight. It is clear that adding a bit of Iron (increasing $\bar{M}$) to either olivine or bronzite will match the density, but it will also lower the sound velocity. To increase the sound velocity and maintain $\bar{M}$, the addition of Al_2O_3 or SiO_2 should do quite well. It would take ~20% alumina to do the job. This might be more than some geophysicists would like. We have a fundamental problem with the olivine-bronzite MgO/SiO_2 ratio. A straightforward

mixture of the high-density oxides would give about the required values for the Earth with a ratio of about two (olivine composition), but the density of olivine is too low, as is that of enstatite, which appears to be identical to olivine. Clearly a dilemma exists.

Composition of the Core

We have already seen that the core must be predominantly iron mixed with some lighter elements or minerals. The results shown in Table II for the core (region E) are not as credible as those for the inner mantle. The seismic data for the core were not of the highest and moreover were approximated by a single phase. However, the Hugoniot EOS listed is certainly reasonable. The picture for the core that is emerging is that the outer melted core is composed of iron mixed with some other lighter material. To date it appears that iron oxide, sulfur, silicon, or any mixture of these can satisfy any constraint of the geophysics community can impose. To date there has been no experimental data to favor one model over any of the other. There does appear to be some agreement that the solid inner core is freezing out of the outer core and is most likely fairly pure iron. Thus, the composition of the Earth is believed to be fairly well known within the caveats mentioned.

The things that have been receiving attention during the recent years is the temperature distribution of the Earth and the iron phase diagram.

The impetus for this activity has been experimental results from diamond-anvil experiments, but mainly from two sets of shock-wave experiments. The sound velocity measurements on strongly shocked iron [83] using the optical detection system [43] have enabled us to determine the melting point on the Hugoniot, and they have shown us the location of a new high-pressure phase (Fig. VIII.12). The temperature of the melting point was calculated by the methods outlined in Sec. III. That work prompted a new generation of phase diagrams. Shortly after the sound-velocity work was reported Bass, Svendsen, and Ahrens [42] reported temperature measurements on shocked iron (Fig. VIII.13). These data and some diamond-anvil results were combined and reported in Science [84]. The net results of that work implies that the temperature of the inner-outer core boundary must be approximately a thousand degrees hotter than the calculated temperature based on the sound velocity data. The diamond-anvil work by Boehler, von Barger, and Hoffbaure [85] are significantly different than [84] and a phase diagram based on that data in general appears to be more compatible with the points based on the sound-velocity data.

Current Work

At the present time there is an effort to measure the longitudinal sound velocity in both olivine and bronzite through conditions existing in the mantle and into the melting regime [86]. This will establish where these materials melt on on the Hugoniot and also the value of the Grüneisen parameter in the melt zone. There is also an effort to measure their shock-temperature loci. The first endeavor will allow us to see if one assemblage or the other matches the seismic velocity of the mantle better. Knowing where the material melts on the Hugoniot could put restrictions on the maximum temperature of the mantle. Measuring the temperatures of these materials will reduce the uncertainty in this limit.

The recently reported temperature measurements on iron were done by observing the radiation coming from the iron through a sapphire window. There is some question of how to calculate the temperature of the iron from the observed radiation from the interface. This problem is currently being addressed by three shock-wave laboratories.

MCQUEEN.LEC.REFS

1. Rankine, W.J.M., On the thermodynamic theory of waves of finite longitudinal disturbance. Transactions of the Royal Society of London 160, 277–288, 1870.

2. Hugoniot, H., Sur la propagation du mouvement dans les corps et spécialement dans les gaz parfaits, Journal de l'école polytechnique, 58, 1–125, 1889.

3. Goranson, R. W., Bancroft, D., Burton, B. L., Belchar, T., Houston, E. E., Gittings, E. F., and Landeen, S. A., Dynamic Determination of the compressibility of metals, J. Appl. Phys. 26, 1472–1479 (1955).

4. Walsh, J. M. and R. H. Christian, Equations of state of metals from shock wave measurements, Phys. Rev. 97, 1544–1556, 1955.

5. Minshall, S., Properties of elastic and plastic waves determined by pin contactors and crystals, J. of Appl. Phys. 26(4), 463–469, 1955.

6. Mallroy, H. D., J. Appl. Phys. 26, 555 (1955).

7. Walsh, J. M., M. H. Rice, R. G. McQueen, and F. L. Yarger, Shock-wave compression of twenty-seven metals: equations of state of metals, Phys. Rev. 108, 196–216, 1957.

8. Shreffler, R. G. and Deal, W. E., Free surface properties of explosive-driven metal plates, J. Appl. Phys. Vol. 24, No. 1, 44–448, January 1953.

9. Al'tshuler, L. V., K. K. Krupnikov, B. N. Ledenev, V. I. Zhuchikhin, and M. I. Brazhinik, Dynamic compressibility and equation of state of iron under high pressure, Soviet Phys. JETP, English Transl. 7, 606–614, 1958.

10. Al'tshuler, L. V., Krupnikov, K. K., and Brazhnik, M. I., J. Exptl. Theoret. Phys. (USSR) 34, 886 (1958); Soviet Phys. JETP 34, 614 (1958).

11. Al'tshuler, L. V., Bakanova, A. A., and Trunin, R. F., Shock adiabats and zero isotherms of seven metals at high pressures, Soviet Physics J. Exptl. Theoret. Phys. Vol. 15, No. 1, 65, July 1962.

12. McQueen, R. G. and S. P. Marsh, Equation of state of nineteen metallic elements from shock-wave measurements to two megabars, J. Appl. Phys. 31, 1253–1269, 1960.

13. McQueen, R. G., Laboratory techniques for very high pressures and the behavior of metals under dynamic loading, in Metallurgy at High Pressures and High Temperatures, K. A. Gschneidner, Jr., M. T. Hepworth, and N.A.D. Parlee, Eds., Metallurgical Society Conferences, Vol. 22 (Gordon and Breach, New York, 1964), pp. 44–132.

14. Rice, M. H., McQueen, R. G., and Walsh, J. M., Compression of solids by strong shock waves, Solid State Physics, F. Seitz and D. Turnbull, Eds. (Academic Press Inc., Publishers, New York and London, 1958), Vol. 6, 1–63.

15. Dugdale, J. S. and MacDonald, D.K. C., *Phys. Rev.* **89**, 832 (1953).

16. Wackerle, J., Shock-wave compression of quartz, *J. Appl. Phys.*, **33**, 922–937, 1962.

17. McQueen, R. G. , S. P. Marsh, J. W. Taylor, J. N. Fritz, and W. J. Carter, The equation of state of solids from shock wave studies, in *High-Velocity Impact Phenomena*, R. Kinslow, Ed., (Academic, New York, 1970), pp. 293–417.

18. Bethe, H. A., The theory of shock waves for an arbitrary equation of state, Office Sci. Res. Develop. Rep. **545**, Serial No. 237, 1942.

19. Bridgman, P. W., *Am. J. Sci.* **237**, 7 (1939).

20. Carter, W. J., Marsh, S. P., and McQueen, R. G., The shock-wave equation of state of polymers, to be submitted.

21. McQueen, R. G., Fritz, J. N., and Marsh, S. P., On the equation of state of stishovite, *J. Geophys. Res.* **68**, 2319–2322, 1963.

22. McQueen, R. G., Marsh, S. P., and Fritz, J. N., Hugoniot equation of state of twelve rocks, *J. Geophys. Res.*, **72 20**, 4999–5036, 1967.

23. Jones, A. H., Isbell, W. M., and Maiden, C. J., Measurement of the very-high-pressure properties of materials using a light-gas gun, *J. App. Phy.*, 37(9), 3493–3499, 1966.

24. Bancroft, D., Peterson, E. L., and Minshall, S., Polymorphism of iron at high pressures, *J. Appl. Phys.*, **27**, 291–2985, 1956.

25. Dick, R. D., Shock wave compression of benzene, carbon disulfide, carbon tetrachloride, and liquid nitrogen, *J. Chem. Phys.*, Vol. 52, No. 12, June 1970

26. Dick, R. D., Shock compression data for liquids. I. Six hydrocarbon compounds, J. Chem. Phys., Vol. 52, No. 12, June 1970.

27. Morgan, J. A., The equation of state of platinum to 680 GPa, High Temperatures-High Pressures, 6, 195–201, 1974.

28. Mitchell, A. C. and Nellis, W. J., 1981, Diagnostic system of the Lawrence Livermore National Laboratory two-stage light-gas gun, *Rev. Sci. Instr.*, **50**, 347–359.

29. Mitchell, A. C. and Nellis, W. J., Shock compression of aluminum, copper, and tantalum, *J. Appl. Phys.*, 52, 3363–3374, 1981.

30. Barker, L. M. and Hollenbach, R. E., Interferometer technique for measuring the dynamic mechanical properties of materials, *Rev. Sci. Instr.* 36, 1617, 1965.

31. Barker, L. M. and Hollenbach, R. E., 1968.

32. Barker, L. M. and Hollenbach, R. E. Hollenbach, Laser interferometer for measuring high velocities of any reflecting surface, *J. Appl. Phys.*, 43, 4669–4675, 1972.

33. Hemsing, W. F., Velocity sensing interferometer (VISAR) modification, *Rev. Sci. Instr.*, 50, 73–78, 1979.

34. Grady, D. E., Murri, W. J., and DeCarli, P., Hugoniot sound velocities and phase transformations in two silicates, *J. Geophys. Res.*, 80, 4857–4861, 1975.

35. Kormer, S. B., Sinitsyn, M. V., Kirillov, G. A., and Urlin, V. D., Experimental determination of temperature in shock-compressed NaCl and KCl and of their melting curves at pressures at up to 700 kbar, *Sov. Phys. JETP*, 21, 689–700, 1965.

36. Kirillov, G. A. , Kormer, S. B., and Sinitsyn, M. V., Equilibrium radiation of shock-compressed ionic crystals, *JETP Lett.* 1, 290–291, 1968.

37. Kormer, S. B., Sinitsyn, M. V., and Kuryapin, A. I., Nonequilibrium radiation from shock compressed ionic crystals at temperatures above 1 eV. I, *Sov. Phys. JETP*, 28, 852, 1969.

38. Zel'dovich, Ya. B. and Raizer, Yu. P., Physics of shock waves and high-temperature hydrodynamic phenomena, Vol. II, Academic Press, NY, 1967.

39. Lyzenga, G. A. and Ahrens, T. J., 1979, A multi-wavelength optical pyrometer for shock compression experiments, *Rev. Sci. Instr.*, 50, 1421–1424.

40. Lyzenga, G. A. and Ahrens, T. J., Shock temperature measurements in Mg_2SiO_4 and SiO_2 at high pressures, *Geophysical Research Letters*, Vol. 7, No. 2, 141–144, 1980.

41. Suguira, H., Kondo, K., and Sawaoka, A., Method for the measurement of temperature in shock compression of solids, *Rev. Sci. Instrum.*, 51 6, 750–752, 1980.

42. Bass, J. D., Svendsen, B., and Ahrens, T. J., The temperatures of shock-compressed iron, in: High Pressure Research in Mineral Physics, eds. Manghnani and Syono (Terra Scientific Publishing Co., Tokyo, 1987), pp. 393–402.

43. McQueen, R. G., Hopson, J. W., and Fritz, J. N., Optical technique for determining rarefaction wave velocities at very high pressures, *Rev. Sci. Instrum.*, 53, 245–250, 1982.

44. Beck, G., *Rev. Sci. Instrum.* 47, 5 (1976).

45. DeCarli, P. S. and Jamieson, J. C., Formation of diamond by explosive shock, *Science* 133, 1821, 1961.

46. Zukas, E. G. and McQueen, R. G., Shock loading to produce fine grain structure, *Trans. Metall. Soc. AIME*, 211, 412-413, 1961.

47. Morris, C. E., Loughran, E. D., Mortensen, G. F., Gray III, G. T., and Shaw, M. S., Shock induced dissociation of polyethylene, in Shock Waves In Condensed Matter - 1983, J. R. Asay, R. A. Graham, and G. K. Straub, Eds., (Elsevier Science Publishers B. V., 1984), p. 7.

48. Pastine, D. J. and Piascesi, D., The existence and implications of curvature in the relations between shock and particle velocities in metals, *J. Phys. Chem. Solids*, **27**, 1783–1792, 1966.

49. Ruoff, Al. L., Linear shock-velocity—particle-velocity relationship, *J. Appl. Phys.*, **38**, 4976–4980, 1967.

50. Jeanloz, Raymond and Grover, Richard, Birch-Murnaghan and $U_s - u_p$ equations of state, in: Proceedings of the APS 1987 Topical Conference on Shock Waves in Condensed Matter, S. C. Schmidt and N. C. Holmes, Eds., Monterey, CA, July 1987.

51. Jeanloz, Raymond, Shock-wave equation of state and finite-strain theory, *J. Geophys. Res.*, May 1988.

52. LASL Sa..ck Hugoniot Data, S. P. Marsh, Ed. University of California Press, Berkeley, Los Angeles, London, 1980.

53. Carter, W. J., Fritz, J. N., Marsh, S. P., and McQueen, R. G., Hugoniot equation of state of the lanthanides, *J. Phys. Chem. Solids*, 1975, Vol. 36, pp. 741–752.

54. Rodean, H. C., Relationship for condensed materials among heat of sublimation, shock-wave velocity and particle velocity, *J. Chem. Phys.*, **49**, 4117–4127, 1968.

55. Rodean, H. C., Evaluation of relation among stress-wave parameters and cohesive energy of condensed materials, *J. Chem. Phys.*, **61**, 4848–4859, 1974.

56. McQueen, R. G. and Marsh, S. P., Ultimate yield strength of copper, *J. Appl. Phys.*, **33**, 654–665, 1962.

57. Grüneisen, E., Theorie des festen Zustandes einatomiger elemente, *Ann. Phys. Berlin*, **39**, 257–306, 1912.

58. Grüneisen, E., The state of a solid body, 76 pp., NASA Re-publication RF 2-18-59 W, February 1959.

59. Slater, J. C., Introduction to chemical physics, Chapter XIII, McGraw-Hill, New York, 1939.

61. Seitz, F., Modern theory of solids, Chapter III, McGraw-Hill, New York, 1940.

62. Born, M. and Huang, K., Dynamical theory of crystal lattices, Chapter II, Clarendon Press, Oxford, 1954.

63. Dugdale, J. S. and MacDonald, D.K.C., *Phys. Rev.* 89, 832 (1953).

64. McQueen, R. G., Fritz, J. N., and Morris, C. E., The velocity of sound behind strong shock waves in 2024 Al, in *Shock Waves in Condensed Matter*, edited by J. R. Asay, R. A. Graham, and G. K. Straub, pp. 95–98, Elsevier, New York, 1984.

65. Al'tshuler, L. V., Kormer, S. B., Brazhnik, M. I., Vladimirov, L. A., Speranskaya, M. P., and Funtikov, A. I., The isentropic compressibility of aluminum, copper, lead, and iron at high pressures, *Soviet Physics JETP*, Vol. 11, No. 4, p. 766, October 1960.

66. Al'tshuler, L. V., Brazhnik, M. I., and Telegin, G.I.S., *J. Appl. Mech. Tech. Phys.* 12, 921 (1971).

67. Shaner, J. W., Brown, J. M., and McQueen, R. G., Melting of metals above 100 GPa, *Mat. Res. Soc. Symp. Proc.*, Vol. 22, (1984).

68. Johnson, Q. and Mitchell, A. C., First x-ray diffraction evidence for a phase transition during shock-wave compression, *Phys. Rev. Lett.* 29, 1369–1371, 1972.

69. Hughes, D. S. and McQueen, R. G., Density of basic rocks at very high pressures, *Trans. Am. Geophys. Union* 39, 959–965 (1958).

70. Birch, F., Elasticity and constitution of the earth's interior, *J. Geophys. Res.*, 57, 227–286, 1952.

71. Ahrens, T. J. and Gregson, Jr., V. G., Shock compression of crustal rocks: Data for quartz, calcite, and plagioclase rocks, *J. Geophys. Res.*, 69 22, 4839–4874, 1964.

72. Trunin, R. F., Gon'shakova, V. I., Simakov, G. V., and Galdin, N. E., A study of rocks under the high pressures and temperatures created by shock compression, *Izv. Acad. Sci. USSR Phys. Solid Earth*, Engl. Transl., 8, 579–586, 1965.

73. Al'tshuier, L. V., Trunin, R. F., and Simakov, G. V., Shock wave compression of periclase and quartz, and the composition of the earth's lower mantle, *Izv. Acad. Sci. USSR, Phys. Sol. Earth*, 657–663, 1965.

74. Ahrens, T. J., High-pressure electrical behavior and equation of state of magnesium oxide from shock-wave measurements, *J. Appl. Phys.*, 37, 2532–2541, 1966.

75. Balchan, A. S. and Cowan, G. R., Shock compression of two iron-silicon alloys to 2.7 megabars, *J. Geophys. Res.*, 71, 3577–3588, 1966.

76. McQueen, R. G. and Marsh, S. P., Shock wave compression of iron nickel alloys and the earth's core, *J. Geophys. Res.*, 71, 1751–1756, 1966.

77. Birch, F., Density and composition of mantle and core, *J. Geophys. Res.*, 69, 4377–4388, 1964.

78. McQueen, R. G., Fritz, J. N., and Marsh, S. P., On the composition of the earth's interior, *J. Geophys. Res.*, **69**, 2947–2965, 1964.

79. Williamson, E. D. and Adams, L. H., Density distribution in the earth, *J. Washington Acad. Sci.*, **13**, 413–428, 1923.

80. Gilbert, F. and Dziewonski, A. M., An application of normal mode theory to the retrieval of structural parameters and source mechanisms from seismic spectra, *Phil. Trans. R. Soc.*, London, 1975.

81. Anderson, D. L. and Hart, R. S., An earth model based on free oscillations and body waves, *J. Geophys. Res.*, **81**, 1461–1475, 1976.

82. Dziewonski, A. M. and Anderson, D. L., Preliminary reference Earth model (PREM), *Phys. Earth Planet. Inter.*, **25**, 297–356, 1981.

83. Brown, J. M. and McQueen, R. G., Melting of iron under core conditions, *Geophysica Research Letters*, Vol. 7, No. 7, pp. 533–536, July 1980.

84. Williams, Q., Jeanloz, R., Bass, J., Svendsen, B., and Ahrens, T. J., Science 236 (1987) 181–182.

85. Boehler, R., Besson, J. M., Nicol, M., Nielsen, M., Itie, J. P., Weill, G., Johnson, S., and Grey, F., *J. Appl. Phys.* **65**, 1795–1797 (1989).

86. Brown, J. M., Furnish, M. D., and McQueen, R. G., Thermodynamics for $(Mg, Fe)_2SiO_4$ from the Hugoniot, *High-Pressure Research in Mineral Physics*, M. H. Manghnani and Y. Syono Eds. (Terra Scientific Publishing Company (TERRAPUB), Tokyo/American Geophysical Union, Washington, DC, 1987.

1A	IIA											IIA	IVA	VA
Li (1) 1.15	Be 1.124											B 4.0	C 01.4	N 1.58 1.31
Na (1) 1.24	Mg 1.263	IIIB	IVB	VB	VIB	VIIB		VIII		IB	IIB	Al 1.338	Si	P
Kb 1.19	Ca 0.94	Sc	Ti 1.09	V 1.20	Cr 1.473	Mn	Fe 1.9	Co 1.33	Ni 1.45	Cu 1.49	Zn 1.56	Ga	Ge	As
Rb (1) 1.23	Sr	Y	Zr 1.02	Nb 1.21	Mo 1.23	Tc	Ru	RH 1.38	Pd 1.59	Ag 1.59	Cd 1.67	In 1.5	Sn 1.48	Sb 1.6
Cs 1.33	Ba	La	Hf 1.12	Ta 1.20	W 1.24	Re 1.367	Os	Ir 1.46	Pt 1.54	Au 1.56	Hg 1.75	Tl 1.52	Pb 1.52	Bi

Fig. II.1. Schematic for deriving the equation for conservation of mass. For one-dimensional flow the cross-section A is uniform through the tube.

Fig. II.2. Schematic used for deriving the equation of motion in plane one-dimensional flow.

Fig. II.3. A moving slab of material undergoing compression used to develop the Lagrangian form of the one-dimensional equation for the conservation of mass.

Fig. II.4. The pressure gradient in a slab of material to develop the equation motion.

Fig. II.5. The power input into a Lagrangian element.

Fig. II.6. A Lagrangian x-t representation of the impact of a relatively thin moving plate usually designated as a driver or impactor, with a thick stationary plate often referred to as a target. The rarefaction waves have just begin to interact, and they will soon put the target plate in tension.

Fig. II.7. Schematic showing the locus of the rarefaction wave interacting with a shock going through a rectangular sample. It is assumed the driver impacts the sample at $t = 0$ as indicated. The shock wave reaches the top of the sample at $t = Y/U_s$ and the rarefaction wave from the edge has moved into the sample a distance X at that time. The driver sample interface has moved a distance Y_1 at that time.

Fig. II.8. The impact of a flat plate on another plate of the same material showing idealized velocity and pressure profiles and the location of the shock wave at various times.

Fig. II.9. Two pressure distance profiles of an initially steep pressure pulse dispersing with time. The top figure shows a shock wave passing through a material of thickness, d. In this exaggerated drawing there is almost as much material in the shock front as in the flat-topped section behind. The bottom figure represents transit time that one would measure if a pressure-sensitive device were placed at d. In typical experiments a similar effect is obtained by detecting motion of the free surface after it has moved a short distance. If the sensing device is placed very close to the surface, large velocities would be indicated relative to placing the detector further from the free surface.

Fig. III.1. Pressure-particle velocity representation of the Hugoniot and the impedance-match solution to reach the high and low-impedance Hugoniots from state O on the middle Hugoniot.

Fig. III.2. Diagram to identify terms used in (11) for calculating reflected shock loci. The shaded area represents the difference in energy between the single-shock Hugoniot and the energy in the shock reflected from state 1 at the volume V_2.

Fig. III.3. Diagram to identify terms in Eq. (III.5) for calculation of release isentropes. The isentrope must usually be integrated numerically. It is assumed that all values are known at state P_{1-1}. The decrease in energy at V_1 down the isentrope is given by Eq. (IV.4). The ratio of the difference in pressure and energy between the isentrope and the Hugoniot at V_1 is equated to γ.

Fig. III.4. Pressure-volume plot of a Hugoniot centered at crystal density, V_x, and one with some porosity at V_o. The shaded area indicates the difference in internal energy between the two at the indicated volume and pressures. It is noteworthy that this difference is independent of the actual Hugoniot loci, only the final state. The Hugoniot of the porous material has a small hump, or special character at the low-pressure end. Although not measured, such character could be caused by material rigidity and it represents the pressure required to collapse pores or voids in the material.

Fig. III.5. A pressure-volume Hugoniot with terms used in the equations to integrate temperature.

Fig. III.6. U_s-U_p Hugoniots for four Elkonites. The measured shock-particle velocity Hugoniots of mixtures of Cu-W and Ag-W are compared with those calculated by the method mixtures outlined in the text.

Fig. III.7. The measured pressure-density Hugoniots of Cu-W and Ag-W compared with those calculated.

Fig. III.8. Hugoniot data for Au-Ge alloys.

Fig. III.9. Hugoniot data for Fe-Ni alloys compared with those calculated as described in the text.

Fig. IV.1. A type of Hugoniot curve that will produce a double-wave shock structure; the resulting pressure profile; and a representative U_s-U_p Hugoniot. Point 3 in (A) is the intersection of the ray from the origin through the cusp on the Hugoniot. Point 1 with the high-pressure Hugoniot. Point 2, curve C will not be observed by some techniques since the faster wave, U_{s1}, will arrive first and destroy the recording equipment.

Fig. IV.2. Particle velocity vs time record on shocked fused quartz obtained from the induced emf in an electrical conductor embedded in the quartz, as it moved through a magnetic field. The timemarks are at 0.1-μs intervals. The light line is an extension to the base line drawn to show the ramping wave. The first break occurs when the shock strength exceeds the maximum pressure of the anomalous compression region. This is followed by another ramping wave and then another shock. The following decay is caused by the Taylor wave in the HE. The test shock wave almost overdrives the first transition wave.

Fig. IV.3. A schematic for the U_s-U_p Hugoniot for fused quartz. Note the original negative slope resulting from the anomalous compression. The dashed section must be obtained from experiments that give time-resolved pressure or velocity records.

Fig. IV.4. Two P-V Hugoniots and the resulting U_s-U_p Hugoniot. hugoniot data for both A and B would be recorded as shown in C with the experimentation used here. In A it has been assumed that the material does not begin to transform at the equilibrium conditions and that it is possible to overdrive the transition pressure by an amount depending on the initial shock strength; however, with time, the material transforms and the pressure decays. In case B it has been assumed that the transformation begins immediately but does not go to completion. This means that although the pressure lies slightly above the Rayleigh ray through the mixed-phase region, the slope does not increase as rapidly as it would if the material had stayed in the initial phase. Although A can give rise to a two-wave structure in the shock front, B of course will not. Hence, in principle the situation is resolvable.

Fig. IV.5. P-V Hugoniots, resulting shock-wave structure and U_s-U_p Hugoniots. In this figure point 3 lies on the extension of the line through the origin and the onset of the beginning of the transition. In (a) part of the Hugoniot lies above the ray through the transition zone and in (b) it lies below. Because of the downward curvature in this region both waves will show rounded profiles, and neither will be steady in time.

Fig. IV.6. Effect of a phase change on the U_s-U_p Hugoniot. In this figure we have considered the case where $dP/dT > 0$. Here and in the next figure H versus V is plotted at constant pressure; P versus T is along the phase line and also along the Hugoniot (dashed line); P versus V is plotted for the phase line boundaries and the Hugoniot loci (dashed line); and finally the type of U_s-U_p Hugonlot (solid line) that might be observed with the experimental technique described here is plotted. In the first row of figures, it is assumed that the original state of the Hugoniot lies in region I (the low-temperature phase) and that it crosses the phase line as indicated. At the present time we do not know of any clear examples of the detection of such a transition solely by U_s-U_p data. It is possible that the Hugoniot could enter the mixed-phase region and finally come out again in region I. In the second row of figures, the slope of the phase line is still positive, but the Hugoniot

3

is centered in the high-temperature phase (region II). When this Hugoniot crosses the mixed-phase region, there is ample experimental and thermodynamic data to show that the Hugoniots as drawn in the P-V and U_s-U_p planes can exist and will give rise to a two-wave structure as previously discussed. It is possible in either of these two cases that the Hugoniot P-T locus will not intersect the phase line.

Fig. IV.7. Phase change with $dP/dT < 0$. If such a phase change exists, the Hugoniot must eventually cross the phase line, provided that the Hugoniot is centered in the low-temperature phase. As drawn, this type of phase change gives rise to the same type of U_s-U_p Hugoniot as illustrated in the lower case in Fig. IV.

Fig. IV.8. P-V diagram to illustrate the conditions required for setting initial conditions for the iteration procedure to determine a meta-stable Hugoniot. Here A is the original low-density phase, and B is the derived, high-density metastable phase. C is the Hugoniot calculated from Hugoniot B but centered at $P = 0$ in phase A. Curve C is compared with the experimental data. Point 1 on Hugoniot A should, in principle at least, be established by the experimental result. Point 2 corresponds to the calculated isothermal volume change of this transition.

Fig. IV.9. Calculated recentered Hugoniots of the transformed high-pressure U_s-U_p Hugoniot obtained by varying the initial density of the high-pressure phase. The above example was for anorthosite with a trial C_{OB} of 7.5 km/s and a slope of 1.25 shown by the dashed line. The data points are designated by the circles. The deviation ΔU_p is found for each data point, and the initial or zero-pressure density ($\rho_{OB} = 3.9$ gm/cm^3) of Hugoniot B is found such that $\Sigma \Delta U_p = 0$.

Fig. IV.10. Calculated recentered Hugoniots of the transformed high-pressure U_s-U_p Hugoniots. This is the same problem as illustrated in Fig. IV.9 except that the results of two additional trials of C_{OB} are presented. All three curves have been obtained by using the initial density (ρ_{OB}) that gives $\Sigma \Delta U_p = 0$. Here $\Sigma (\Delta U_p)^2$ is a minimum for $C_{OB} = 5.79$ km/s.

Fig. IV.11. Calculated recentered Hugoniots obtained as in Fig. IV.10 except that two additional slopes have been used, thus demonstrating how this variation tends to bend the resulting calculated Hugoniots. The dashed lines (1, 2, and 3) represent the metastable Hugoniots that are transformed to the solid curves. All three curves fit the data quite well. This shows that, even thought there is a combination of ρ_o, C_o, and S that gives the best fit, the experimental data are usually not good enough to warrant this selection. However, the data do appear good enough to determine two of the parameters if the third is specified.

Fig. IV.12. $\Sigma (\Delta U_p)^2$ versus C_{OB} for various slopes and for the same problem as illustrated in Figs. IV.9–IV.11. The number at the bottom of each curve is the value of the slope used. The large increase in $\Sigma (\Delta U_p)^2$ for slopes greater than 1.5 arises from the fact that these require that the densities and sound velocities be less than the assumed stable phase, and it is quite impossible to obtain decent fits of the data. Any of the fits from $S = 1.0$ to 1.5 usually give quite adequate representation of the data, and the minimum near 1.5 must sometimes be disregarded for other physical requirements. Similar curves were obtained

for all the rocks analyzed in this manner.

Fig. IV.13. Hugoniot EOS curves for one-dimensional strains and equilibrium states, which control the initial elastic-plastic flow in shocked solids with rigidity. These also govern the release paths as can be seen in (b). The structure shown in (b) can give rise to wave profiles like shown in (c) for impact experiments. The pressure difference from the maximum pressure to the level indicated by REL gives a measure of the state of the material at pressure but does not give enough information to determine how close the Hugoniot point is to equilibrium. The impedance-match solution, (d) gives an indication of the type of errors introduced by rigidity effects in a standard.

Fig. V.1. A cross-sectional view of an HE-metal driver system used for EOS studies. As indicated a rotating-mirror sweeping image camera was used for the diagnostics. The plastic layer prevented driver plate breakup when the plate was thin. By using various explosives and other components a wide pressure range could be covered.

Fig. V.2. The free surface trajectory of shock loaded iron showing the arrival of the elastic wave, the first plastic wave and the arrival of the material in the mixed phase regime. The breaks are quite distinct and the average velocities well determined. Further differentiation is not warranted.

Fig. V.3. The cryogenic system used by Dick for measuring shock transit times in liquid N_2 and the motion of the 2024 Al driver plate. Approximately 20 pins were used in each measurement.

Fig. V.4. The U_s-U_p Hugoniot data for liquid N_2 measured by R. Dick. Although the large number of data is unusual the remarkable linearity is typical of most substances. There is a slight change in slope at about $U_p = 2.7$ mm/μs. It has been surmised that this is the onset of dissociation N_2 to other species.

Fig. V.5. Target assembly and pin holder used by Morgan to measure shock transit times.

Fig. V.6. Records for various measurements on a two-stage gun experiment. a) Time marks generated by the projectile, passing magnetic pickup loops. b) X-ray of the sabot and impactor. c) Raster an oscilloscope record of the x-ray trigger pulses. d) Pin pulses for shock transit time measurements.

Fig. V.7. A schematic of a flash-gap type of assembly that could be used to measure shock transit time through a shocked sample placed on a base plate. The film is exposed when the shocked free surface of the materials under the Plexiglas block travels ~0.9 of the distance of the gap. Since the free surface of the two materials (base plate and sample) are not necessarily the same, their velocities must be calculated (by methods described in Sec. II) and the appropriate correction in transit times made. A somewhat smaller correction is needed in the situation described in B where a shim of the same material as the baseplate is placed on the sample. The shock state on the shim must be calculated from an assumed EOS for the sample and its shock transit time and free surface velocities then calculated for the correction. In the third example, C, shims of the same material as the sample are placed on the reference on base plate. Now no calculations are necessary if the gaps are the same thickness. Unfortunately, it is not always possible to make the assemblies this way. Type B are usually used, which in addition to minimize the corrections insures that the optical character of the traces are the same over references and samples, which minimizes film-reading errors. The thickness of the gaps and shims shown are many times larger than actually used.

Fig. V.8. Shock-particle velocity assembly. In this assembly a driver plate strikes the bottom surface. The left-hand side of the assembly gives shock velocities by measuring the transit time through samples of different thicknesses. On the right-hand side the difference in transit time of the driver plate and the shock wave through the distance of the small gap on the bottom of the assembly is measured. When used with the measured shock velocity,

the driver plate velocity can be obtained.

Fig. V.9. A photographic record for a shock-particle velocity experiment. Transit times are obtained by measuring the distance between the offsets traces and the interpolated position where the reference would be, and dividing by the known writing speed of the camera (8.3 mm/μs). Driver plate curvature is apparent but accountable.

Fig. V.10. U_s-U_p data for Iron, Cu, 2024 Al, and U-3% Mo obtained by symmetrical direct impact measurements. ($\times$) 2024 Al, ($\circ$) 921T Al, ($*$) Fe, ($+$) Cu, ($\square$) U-3%-Mo alloy.

Fig. V.11. P-U_p velocity data for Iron, Cu, 2024 Al, and U-3% Mo obtained from direct impact measurements. These data cover a substantial area of the P-U_p space.

Fig. V.12. Impedance-match solution. The curve labeled Hugoniot is that of the standard, and point 1 is the measured state. The cross curve to the left represents reflected shock states of the standard shocked from (1), and those to the right represent states reached by an isentropic pressure release. The ray from the origin represents possible shock states of the material being investigated and is a consequence of the equation for conservation of momentum (II.40). The intersection of this ray, which is sometimes called the Rho-D line, from detonation physics, with the cross curve at (2) gives the pressure and particle velocity. The reflected shock and isentrope loci are almost mirror images of the Hugoniot. This approximation, which although is usually quite adequate is not quite correct, has often been used.

Fig. V.13. A schematic of an assembly used to obtain shock-wave EOS data. Various views of a standard multiple sample assembly used for obtaining Hugoniot data for many solid materials. There are four rows of two samples each indicated by raised cross-hatched rectangles. A flash block, a rectangular bar of Plexiglas with a small ~0.1-mm-deep, 13-mm-wide groove, machined in it is placed on each bar and on the base plate next to them. These blocks also will hold shims ~0.2-mm thick on top of the bars, if desired. The gas box is evacuated and filled with a gas. Xe is used for low-pressure measurements, and Ar for high-pressure shots. A photographic slit plate is placed on the gas box lid so that the shock arrival can be determined at various areas on the assembly. The shock transit times through eight samples are obtained two are usually the standard. By using the impedance match technique the P-U_p states for the other samples are determined. As indicated several slits are placed over each sample so some statistics can be obtained. The major benefit of using several slits is that assembly errors are readily detected, in particular if a sample or a flash black is not properly secured the spacing between slit traces will be different than its references. Although this is not the assembly used by Walsh it has been used for many years and is still being used.

Fig. V.14. An enlargement of a photograph record of a typical experiment. Two of the samples were made of the base plate or standard material. Here they have been identified as Al. The irregularity of the other traces is due to inhomogeneities in the samples. These were rocks and some of which had large grains of different minerals.

Fig. V.15. Shock-particle velocity data used for cross checking the standards. Here Cu was used as the standard. The top curve is for 921-T Al followed by Cu, Fe, and U-3%

Mo. (×) 2024 Al, (o) 921T Al, (*) Fe, (+) U–3%-Mo alloy.

Fig. V.16. Shock-particle velocity data used for cross checking the standards. Here 2024 Al was used as the standard. The top curve is for 921-T Al followed by Cu, Fe, and U–3% Mo.

Fig. V.17. Shock-particle velocity data used for cross checking the standard. Here 2024 Al was used as the standard. The Hugoniot of the iron was not linear but the Hugoniot data for the other materials are. The top curve is for 921-T Al followed by Cu, Fe, and U–3% Mo.

Fig. V.18. A schematic of a VISAR described by Barker and Hollenbach [1972]. Schematic of a VISAR optical system currently being used. The optical paths used to obtain two quadratures can be seen.

Fig. V.19. The results of a VISAR record of the particle velocity history of a LiF-Peridot interface driver by the impact of an Al driver and the subsequent rarefaction from the back surface of the driver. The figure to the left is a hypothetical velocity locus.

Fig. V.20. A diagram of the six-channel optical pyrometer used on the two-stage gas gun at the Lawrence Livermore National Laboratory. The objective lens views an area approximately 5 mm in diameter. The beam is split into the six photomultiplier tubes (PMT). Most of the system is outside the confinement chamber so a permanently aligned system can be used to calibrate light intensity records. This figure courtesy of Boslough and Ahrens, 1979.

Fig. V.21. A series of radiation vs wave length data plots along with best fits to the Planck's distribution function. At the wave lengths sampled they claim best sensitivity at about 5000 K. This figure courtesy of Boslough and Ahrens et al., 1980.

Fig. V.22. Temperatures measured by Lysenga, Ahrens, and Mitchell on Shocked SiO_2.

Fig. V.23. A nontime-resolved spectra obtained with a multiple-channel analyzer. Conceivably the jass in the trace is due to small sampling size. The average sampling bandwidth must be about 10 nm, thus if there were a sharp emission line or absorption band it might be seen even when averaged over sampling width. This figure courtesy of Boslough and Ahrens.

Fig. V.24. A plot of the inverse percent transmission as recorded by a microdensitometry scan of a photographic record. The fourteen splits over the nitromethane cover a range in radiation levels of a factor of four in seven steps. The slits over the samples cover a range of about two. The radiation from the fuse quartz was too great because the wrong size slit plate was used. The high-intensity-record must not be used, because it is impossible to make a meaningful extrapolation of the standard.

Fig. V.25. The radiation of the nitromethane, from Fig. V.24, is plotted against the slit width. The relative radiation from the samples is matched to this curve to establish the ratio of its radiation to that of the nitromethane. The radiation response to temperature

over the wave length for which the film is sensitive is used to determine the temperature.

Fig. V.26. The relative radiation of SiO_2 to nitromethane plotted against the shock particle velocity. Since U_p is a function of the internal energy (Eq. II.42) the fact that both the fused quartz and crystal quartz data fell on the same loci attest to the fact that both are most likely in the same high-pressure phase.

Fig. V.27. An x-t plot with the shocks and rarefaction waves, etc., indicated. This is equivalent to an experiment where there were target thicknesses of 2, 3, and 4 mm. The three measured Δt's extrapolate to the time the rarefaction wave first overtakes the shock in the target. Here at $x = 4$ mm.

Fig. V.28. In most measuring techniques the data are obtained at a given location in the material, e.g., a pressure-sensing transducer or at an interface where velocities are measured. Here the radiation is observed at the shock front as it moves through the sample. Both records show the pressure decrease caused by a rarefaction overtaking the shock wave in an impact experiment. The records can look similar but they are indeed different.

Fig. V.29. Reproductions of some records on an experiment to study the merits of some various analyzers. Two artifacts of the shock assemblies can then be seen: 1) the effect of a small air gap in the left-hand quartz record; and the effect of an excessively large glue joint in the right-hand glass record. The decay section of the analyzers is different, but the catch-up positions are the same.

Fig. V.30. Sample thickness vs catchup distance for an overtake experiment on 2024 Al using bromoform as the analyzer. In this high-quality data set the sigma for the least squares fit of the data was less than 0.2%. The linearity is predicted from the analysis on characteristics discussed in Sec. II.

Fig. V.31. The radiation emitted from a layered fused quartz target with an opaque aluminized interface and two 90% transmission aluminized interfaces. In addition to the shock arrivals the time of the overtake is quite clear.

Fig. V.32. Radiation from bromoform impacted by a 316 SS driver. The bromoform was covered by an opaque aluminized cover of mylar. Partially opaque layers of mylar were suspended in the bromoform. The radiation increases when the shock wave passes these layers, which like on the previous figure (VI.31) gives a measure of the shock front thickness if the layers are parallel to the front. In addition to the increase in radiation a small sharp decrease in radiation can be seen as the pressure and temperature or transmission decreases when the shock traverses the low density 5-micron-thick plastic films.

Fig. V.33. A recovery system used to shock load larg.. samples or several small ones. A plane wave lens initiates the charge, which accelerates the driver plate. The one-half-inch air gaps prevents spall of the driver. The release wave from the driver decreases pressure in the central region before rarefactions come in from the sides. The momentum from the driver is imparted to the lower plates. By using several plates, no tension waves reach the region of interest. The assemblies are fired above containers with water or on piles of sand

or both. The samples are usually found directly below their starting position.

Fig. V.34. A recovery system used by Morris et al. to study the dissociation of polymers under shock loading. The system is unique in that the decomposition products, which were amorphous carbon, diamond, and various gaseous hydrocarbons were all confined and their relative abundances were measured.

Fig. VI.1. Histogram of the frequency of the slope of the Hugoniot EOS.

Fig. VI.2. The slope of the lanthanide Hugoniots [56].

Fig. VI.3. Linear U_s-U_p Hugoniots illustrating the range covered by experiments on different materials. All the materials to the left of $U_p = 0$ are in the negative pressure region. Materials like Al_2O_3 with very high sound velocities also have very large binding energies. If one subscribes to the belief that the slope is a strong measure of the effective repulsive parameter of the atomic system it is easy to visualize how lowering S increases the binding energy as the top two lines indicate. The middle two lines represent Mg and Mo with the same indicated binding energies whose other properties are quite dissimilar. The bottom line is representative of Hg. Taylor demonstrated that on the μs scale Hg also will support a modest tension stress.

Fig. VI.4. Schematic of the pressure and energy typical for a linear U_s-U_p Hugoniot. As indicated this material has a binding energy comparable to the energy produced by the shock-wave.

Fig. VI.5. Rodean's compilation of cohesive energy compared with Eq. (VI 13).

Fig. VI.6. Rodean's comparison of cohesive energy vs Eq. (VI.13) for some alkali halides.

Fig. VII.1. Shock-particle velocity data for porous Cu samples using crystal density Cu as a standard. The symbols show the average value of the fractional densities of each set: (X) 1.0, (O) 0.88, (*) 0.71, (+) 0.71, (⊓) 0.64, (•) 0.51.

Fig. VII.2. Pressure vs relative volume data for Cu data shown in Fig. 1. The symbols show fractional densities of each set: (X) 1.0, (O) 0.88, (*) 0.82, (+) 0.71, (⊓) 0.64, (•) 0.51.

Fig. VII.3. Plots of $dE/dP]_V$ obtained from the shock velocity data on porous Cu (Fig. 0.1). The following symbols and lines used to identify the fractional densities: (O) 0.88, — - —; (*) 0.82, — – —; (⊓) 0.71, — — —; (×) 0.64, — —— —; (+) 0.51, — —— —. The solid line is from the calculated gamma using the Dougdale-McDonald equation.

Fig. VII.4. Plots of $dE/dP]_V$ obtained from shock data on porous iron samples. The fractional densities of the samples are: (O) 0.89, — - —; (*) 0.76, — – —; (⊓) 0.60, — — —; (×) 0.43, — —— —. Clearly the effect of temperature or some other systematic behavior is being displayed.

Fig. VII.5. Sound velocity behind the shock wave in Ta.

Fig. VIII.1. U_s-U_p Hugoniot data for two rocks. These two rocks have the general composition $(Mg,Fe)_2SiO_4$ with ~10% additional minerals. The olivine has an MgO/FeO ratio of about 90% and this Morchokee Mine MgO/FeO of about 50%. In general, increasing the iron in simple substitution for Mg not only increases the density but also increases the shock velocity. These records indicate that the high pressure transition would not be manifested by a two-wave structure.

Fig. VIII.2. U_s-U_p Hugoniot data for two enstatite-type rocks. Both rocks have MgO/FeO ratios of about 85%, both have the general composition $(Mg,Fe)SiO_3$ with about 15% other high-density-type silicates and oxides. The data for the Stillwater Complex bronzite indicates that a two-wave structure would probably not be present for the high-pressure transition. The lower set indicates that a two-wave structure might exist.

Fig. VIII.3. Pressure-density plots of the Hugoniots for various minerals compared with a likely distribution for the Earth.

Fig. VIII.4. Comparison of some pressure-density Hugoniots for various Fe compounds and alloys with a likely pressure-density distribution through the Earth's core.

Fig. VIII.5. U_s-U_p points through the Earth that satisfy the first requirements for the iteration procedure outlined in the text. A single-trial EOS set was used for the whole Earth. The calculated points wander between the two trials with the different regions of the Earth clearly observed.

Fig. VIII.6. U_s-U_p points to demonstrate how the solution converges in the inner mantle. Acceptable solution has been found for regions B and C. In general, too large a choice for the slope results in too low a slope for the U_s-U_p points.

Fig. VIII.7. U_s-U_p points that have nearly converged in the mantle.

Fig. VIII.8. U_s-U_p for the mantle demonstrating that there are other trial EOS that lead to the same solution. Here the same C_o was used for both trial EOS but their slopes were different.

Fig. VIII.9. The U_s-U_p solution for the whole Earth. Clearly the locus of points for each region is remarkably linear. The negative particle velocity for the beginning of the B region is caused by the high temperature of the outer mantle relative to the Hugoniot.

Fig. VIII.10. U_s-U_p data for olivine and bronzite.

Fig. VIII.11. Sound velocity vs density for oxides and other minerals ploted with the mean molecular weight, $\bar{M}$.

Fig. VIII.12. Sound velocity vs pressure for shocked Iron.

Fig. VIII.13. Shock temperature measurements in Fe. Courtesy of J. Bass.

Fig. VIII.14. Sound-velocity measurements on shocked forsterite and olivine compared with sound velocities through the Earth's mantle derived from seismic data.

$$\Delta X$$

$$A\rho\ U\ dt \longrightarrow$$

$$\rho + \frac{\partial\rho}{\partial X}\Delta X\ dt \longrightarrow$$

$$U + \frac{\partial U}{\partial X}\Delta X dt \longrightarrow$$

$$X \qquad\qquad X + \Delta X$$

Figure II.1

$$\Delta X$$

$$P(X) \longrightarrow$$

$$P(X) + \frac{\partial P}{\partial X} \longrightarrow$$

$$X \qquad\qquad X + \Delta X$$

Figure II.2

$$\Delta X$$

$$t \qquad\qquad \rho(t)$$

$$\underline{X} \qquad\qquad \underline{X + \Delta X}$$

$$t + \Delta t \qquad\qquad \rho(t + \Delta t)$$

$$\underline{X + U(X)\Delta t} \qquad \underline{X + \Delta X + U(X + \Delta X)\Delta t}$$

Figure II.3

P(X) ΔX P(X + ΔX)

ρ

U

X X + ΔX

Figure II.4

ΔX

UP(X) ρ UP(X + ΔX)

$U^2/2$

E

X X + ΔX
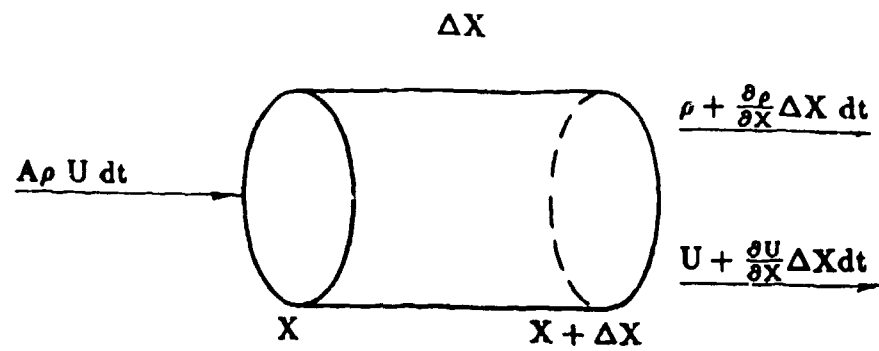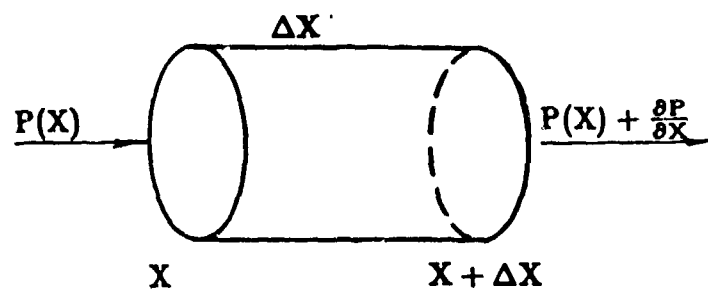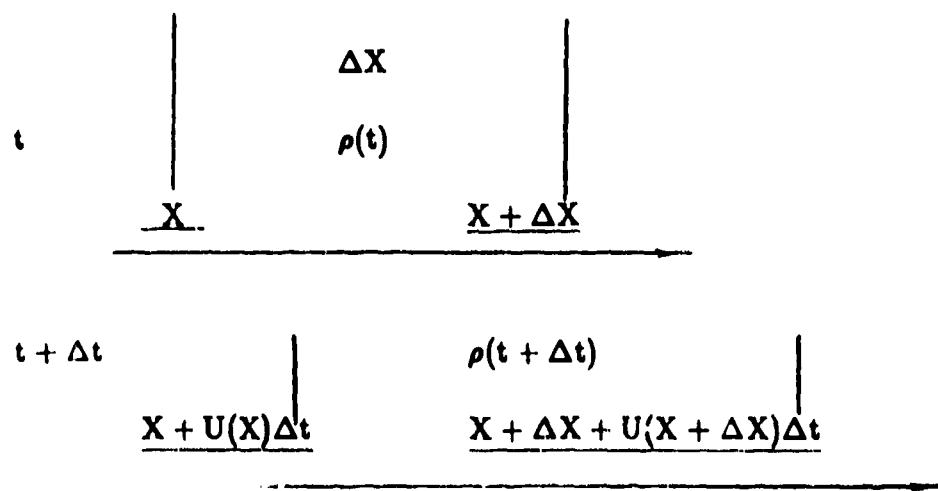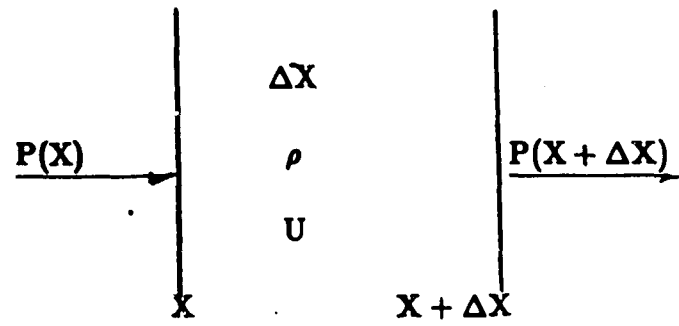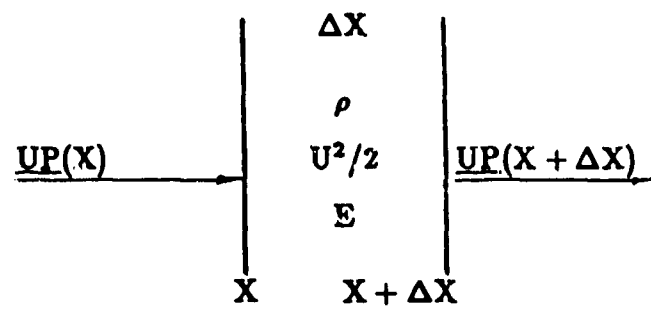
Figure II.5.

Figure II.6

Figure 13.7

DRIVER   TARGET

d

$U_P = 0$

$U_P = U_D$

COLLISION TIME
$t = 0$

SHOCK WAVE
HALF WAY
THROUGH DRIVER

TIME = $t/2$

SHOCK THROUGH
DRIVER

TIME = t

EULERIAN
COORDINATE
X

DRIVER   TARGET

INTERFACE

U_D

U_P

P

O d   x

x

U_D

U_P

P

O x

x

U_P

P

O x

x

PARTICLE
VELOCITY,
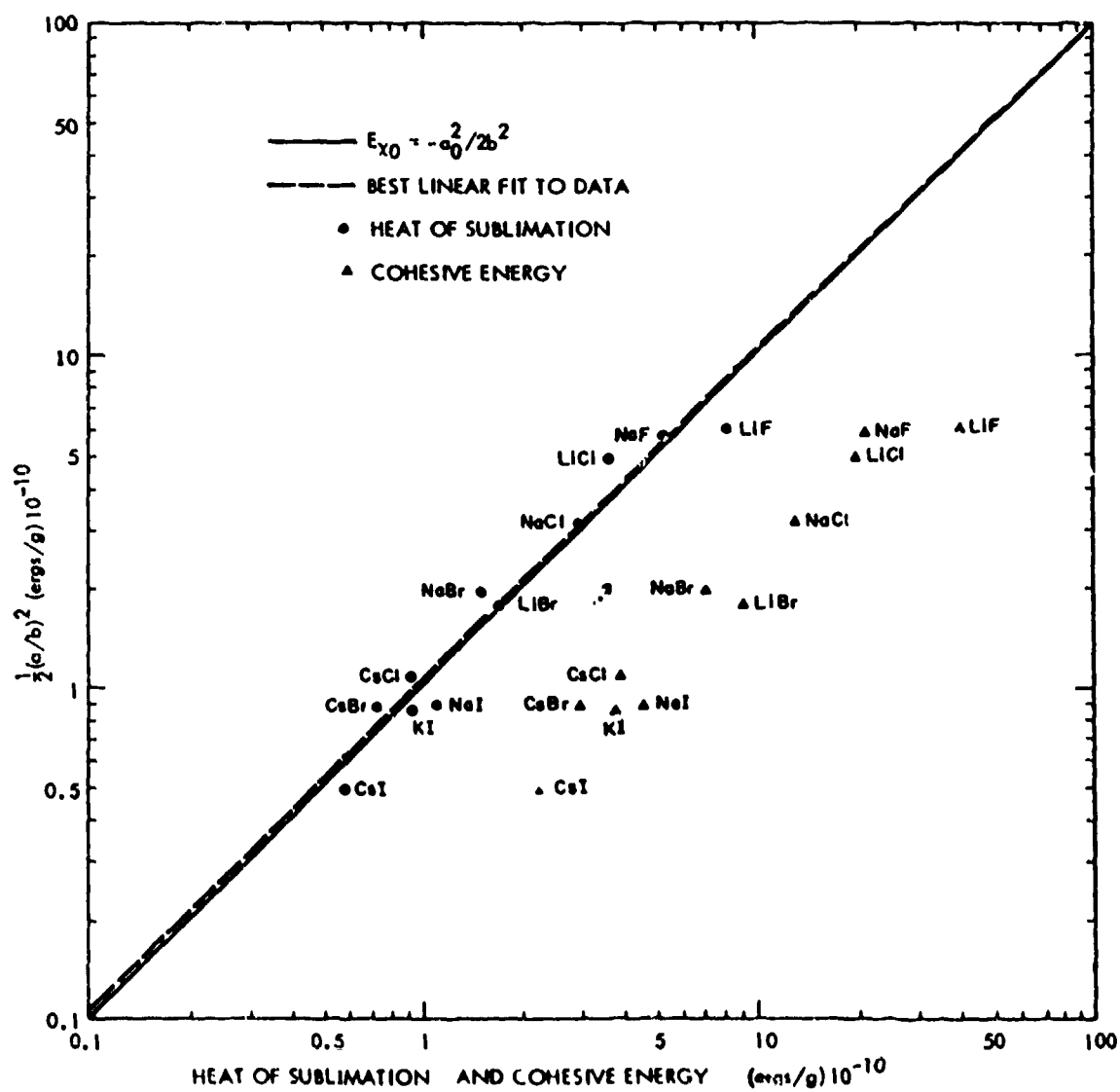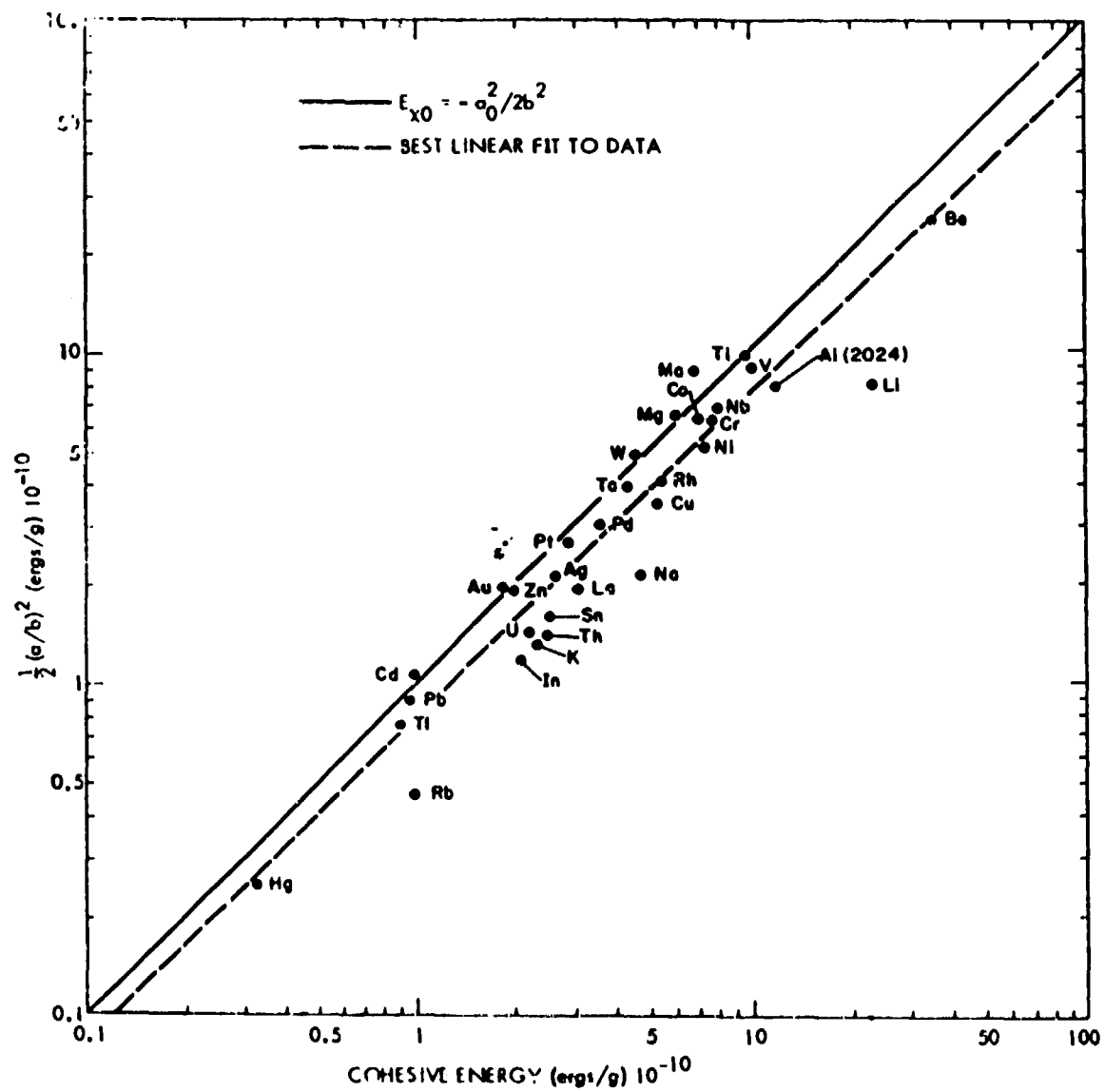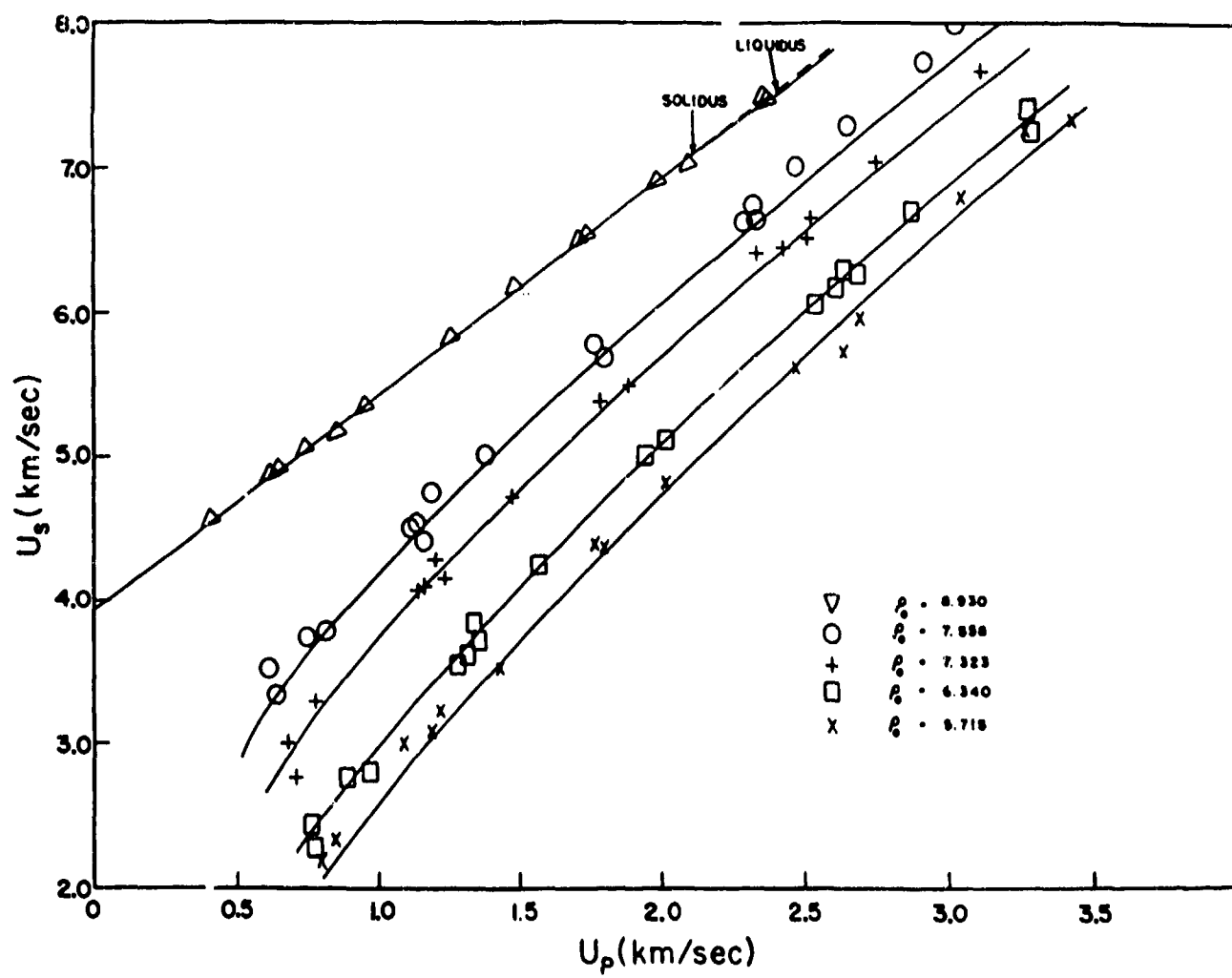U_P, vs x

PRESSURE,
P, vs x

LAGRANGIAN
COORDINATE
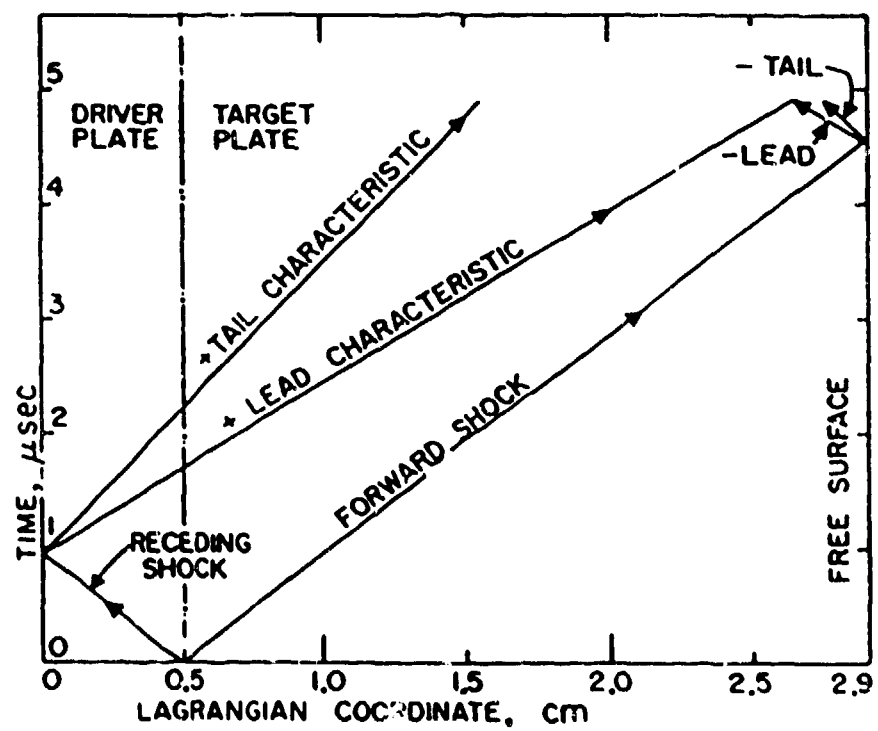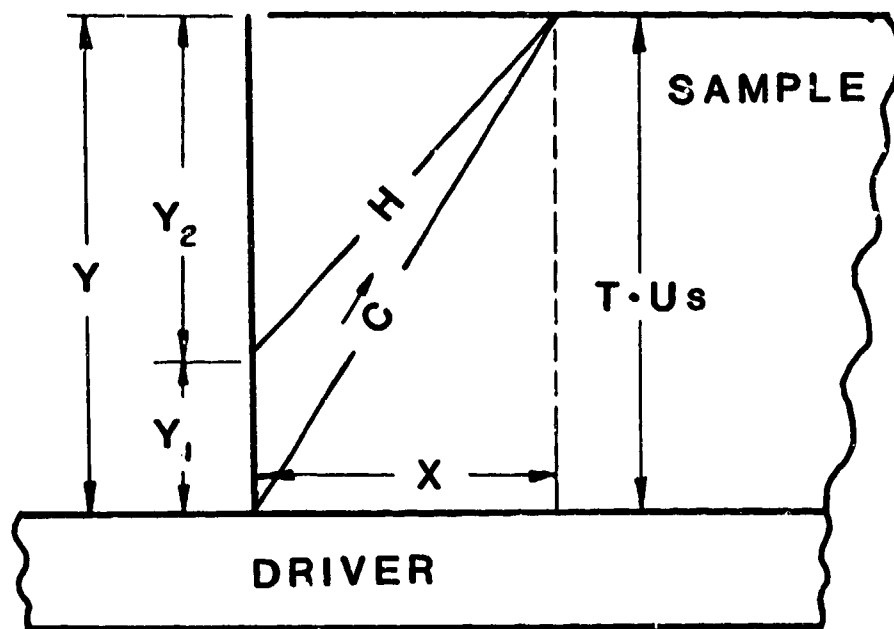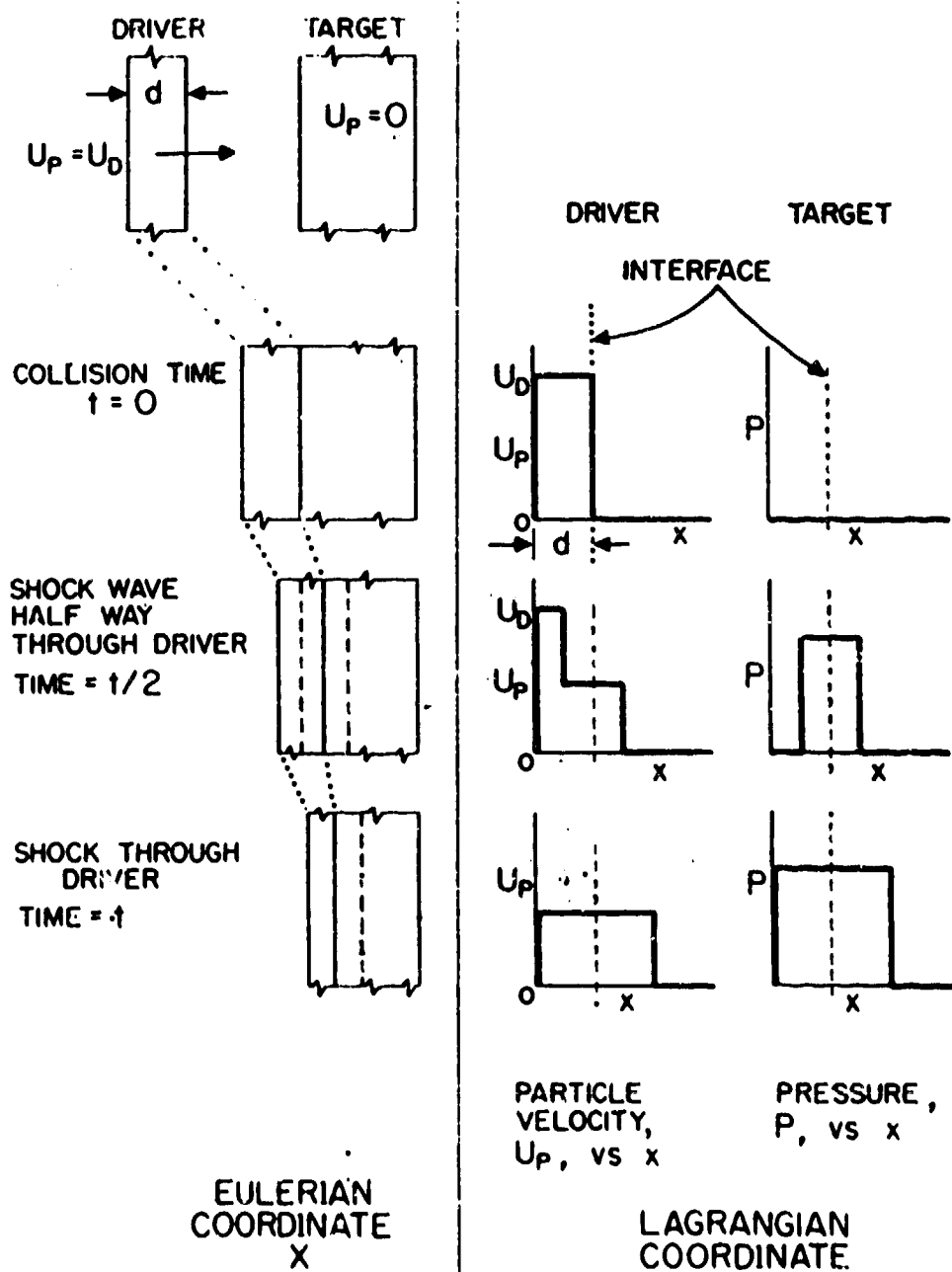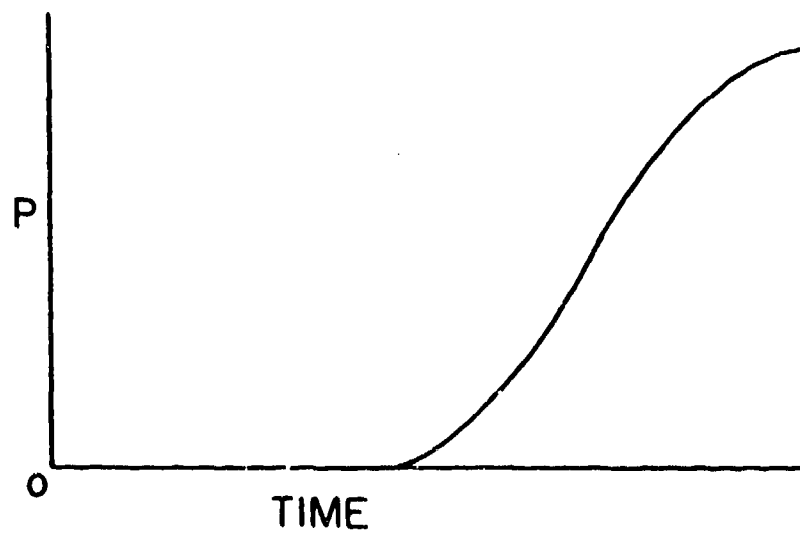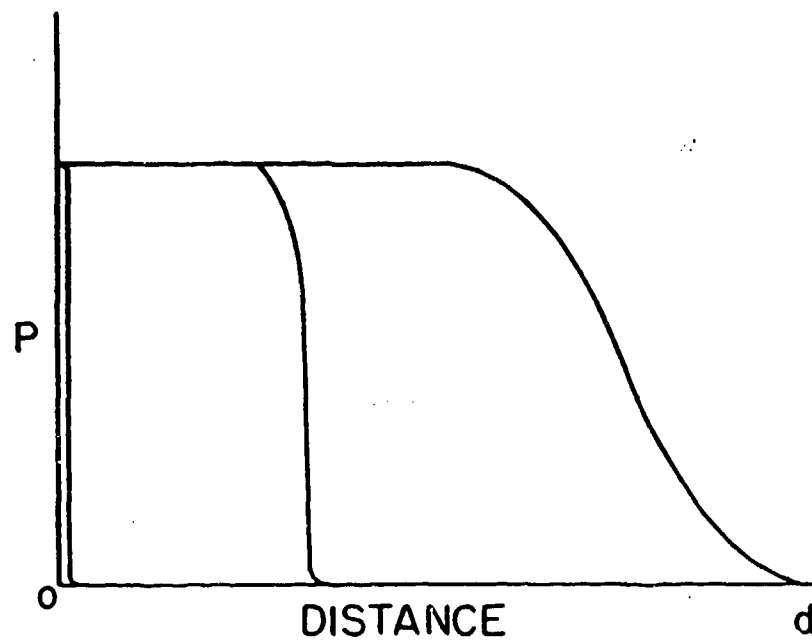
Figure II.8

Figure II.9

Figure III.1

Figure III.2

HUGONIOT

CALCULATED
ISENTROPE

P_{i-1} , E_{i-1}

P_i

P_H , E_H

V_{i-1} V_i V_o

P

V
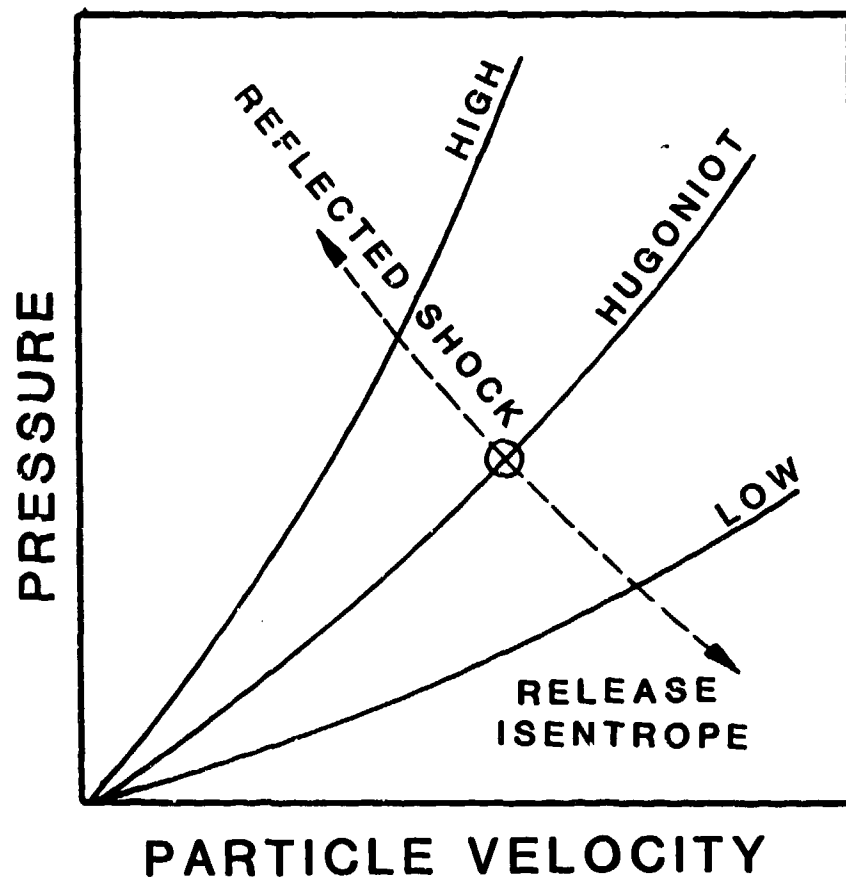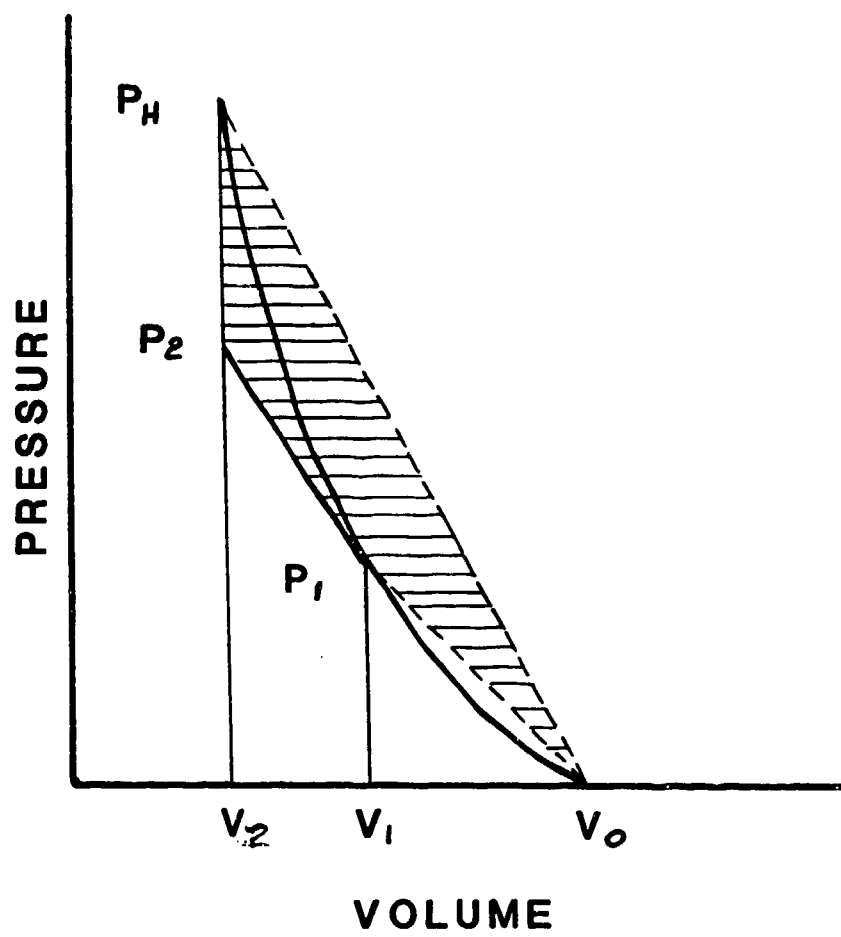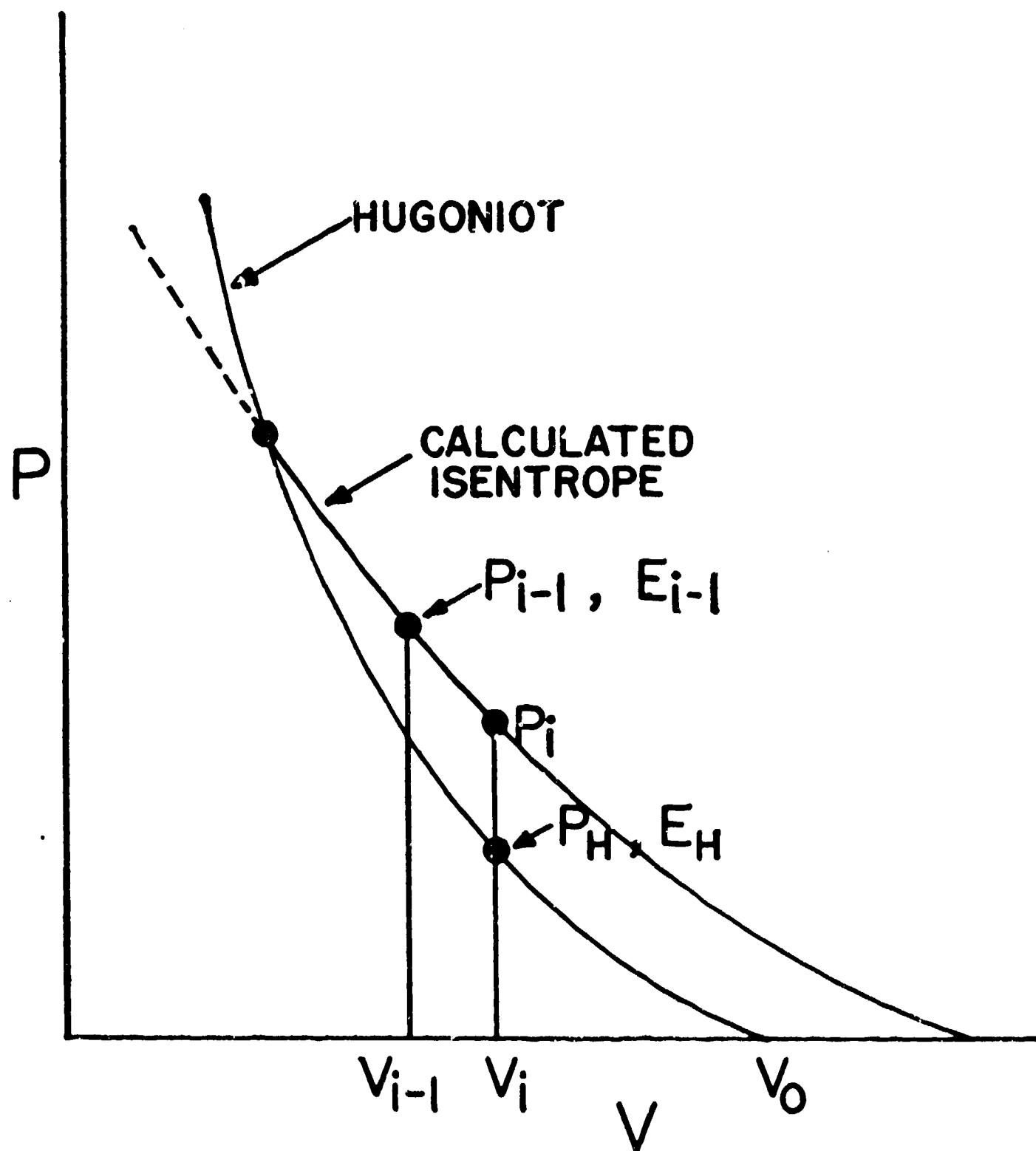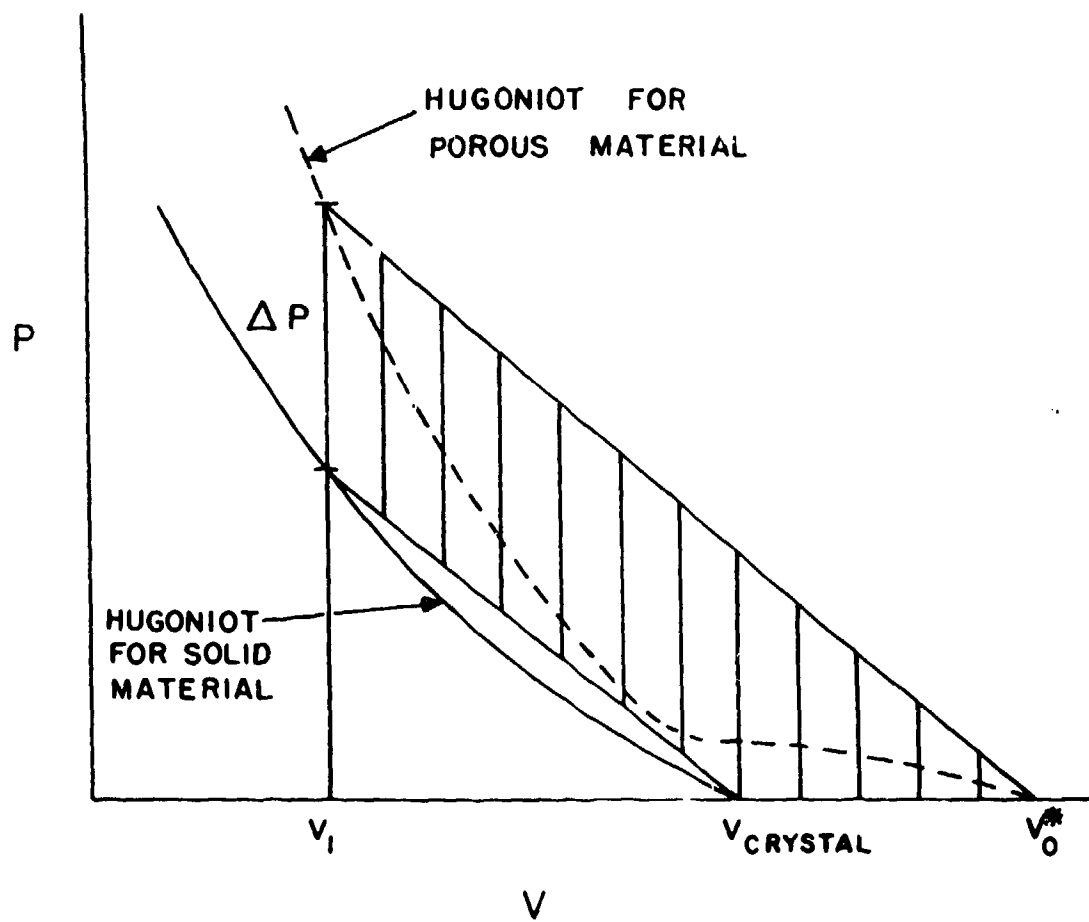
Figure III.3
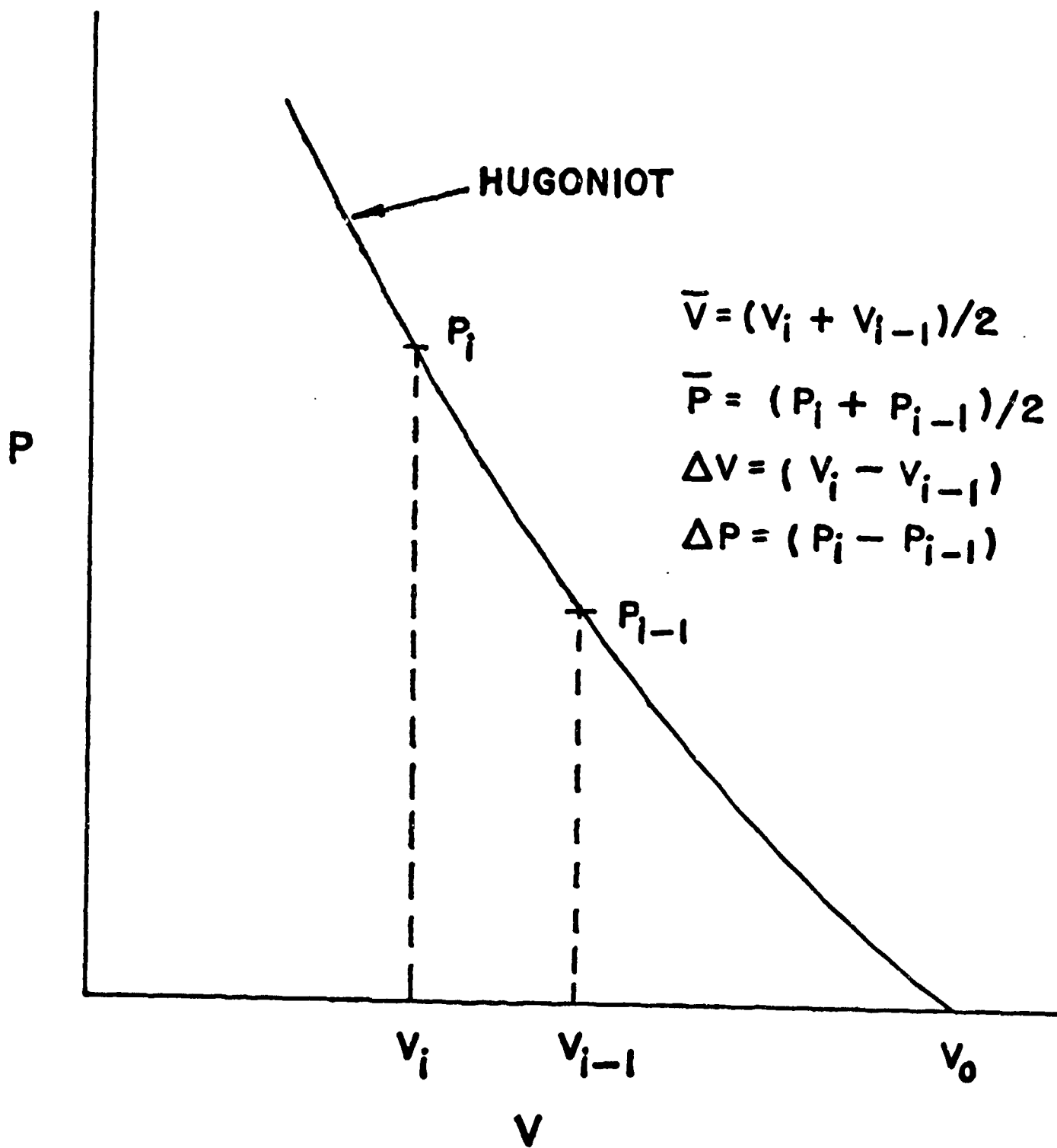
Figure III.4

Figure III.5
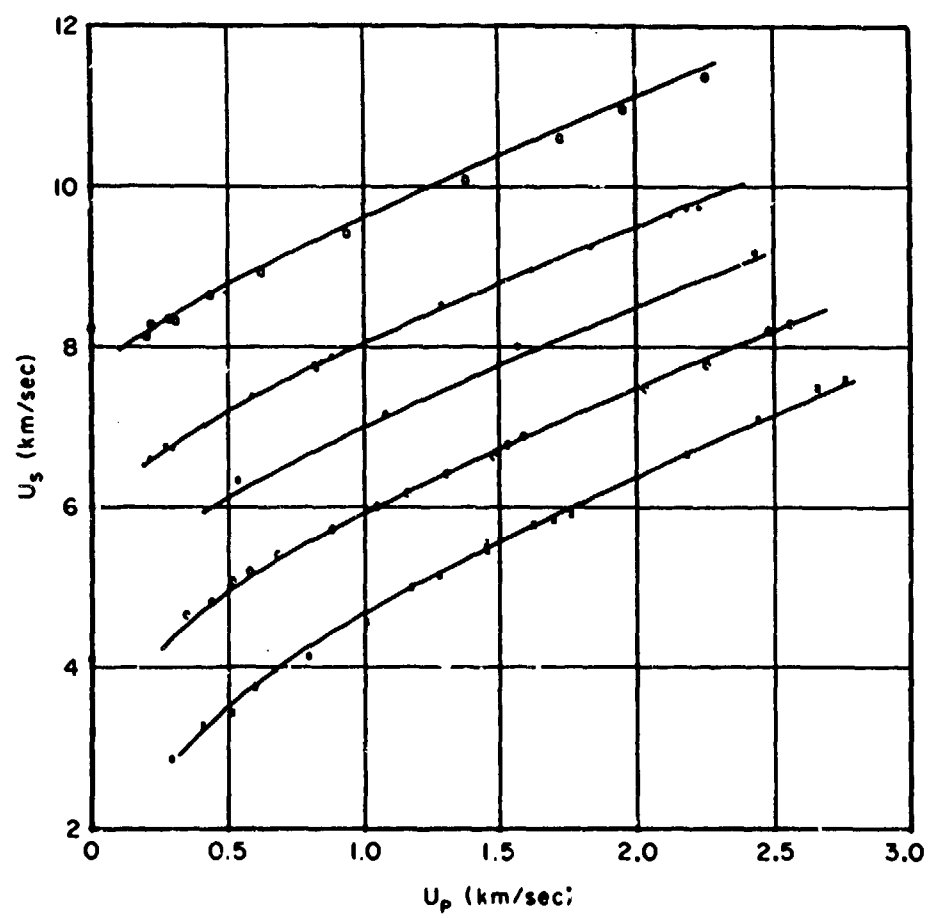
Figure III.6
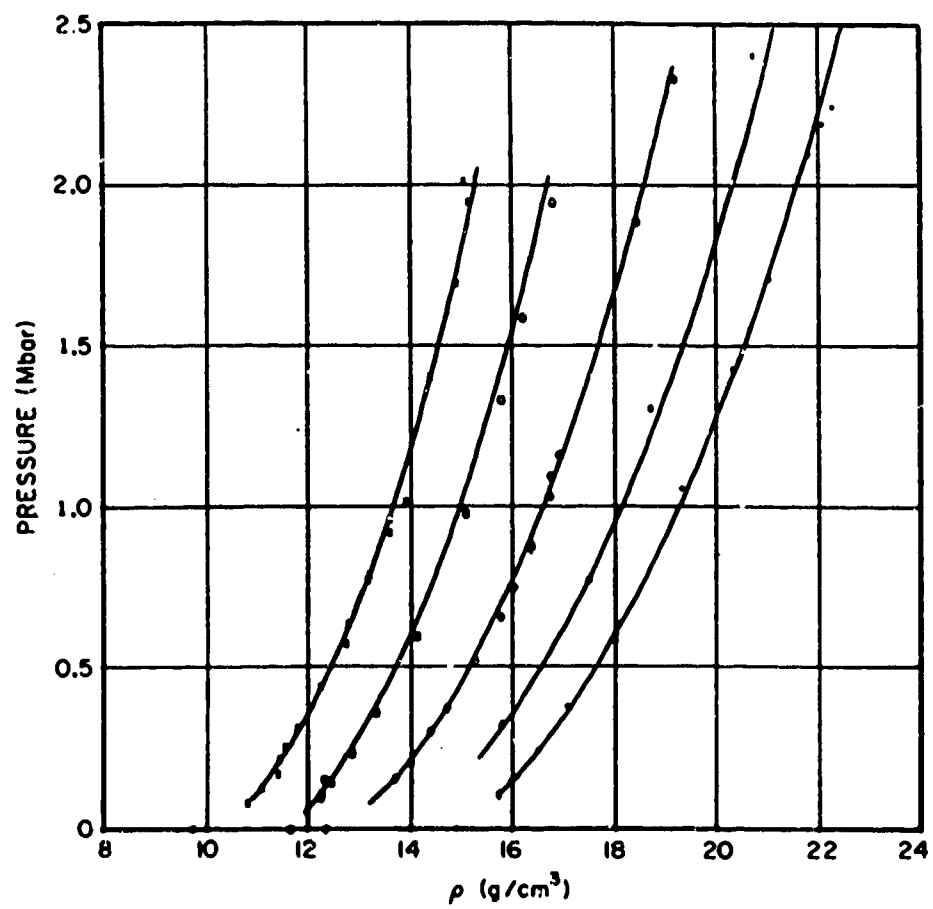
Figure III.7

Figure III.8

Figure III.9

(a)	(b)	(c)
HUGONIOT	SHOCK PROFILE	HUGONIOT
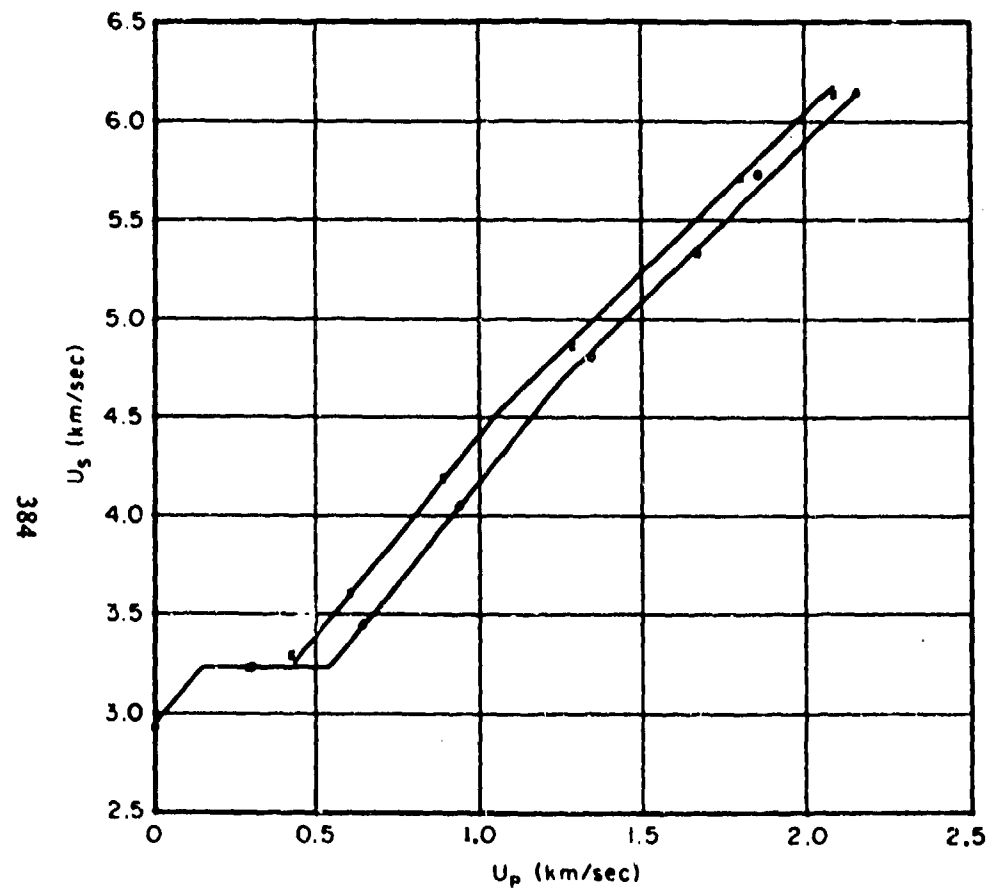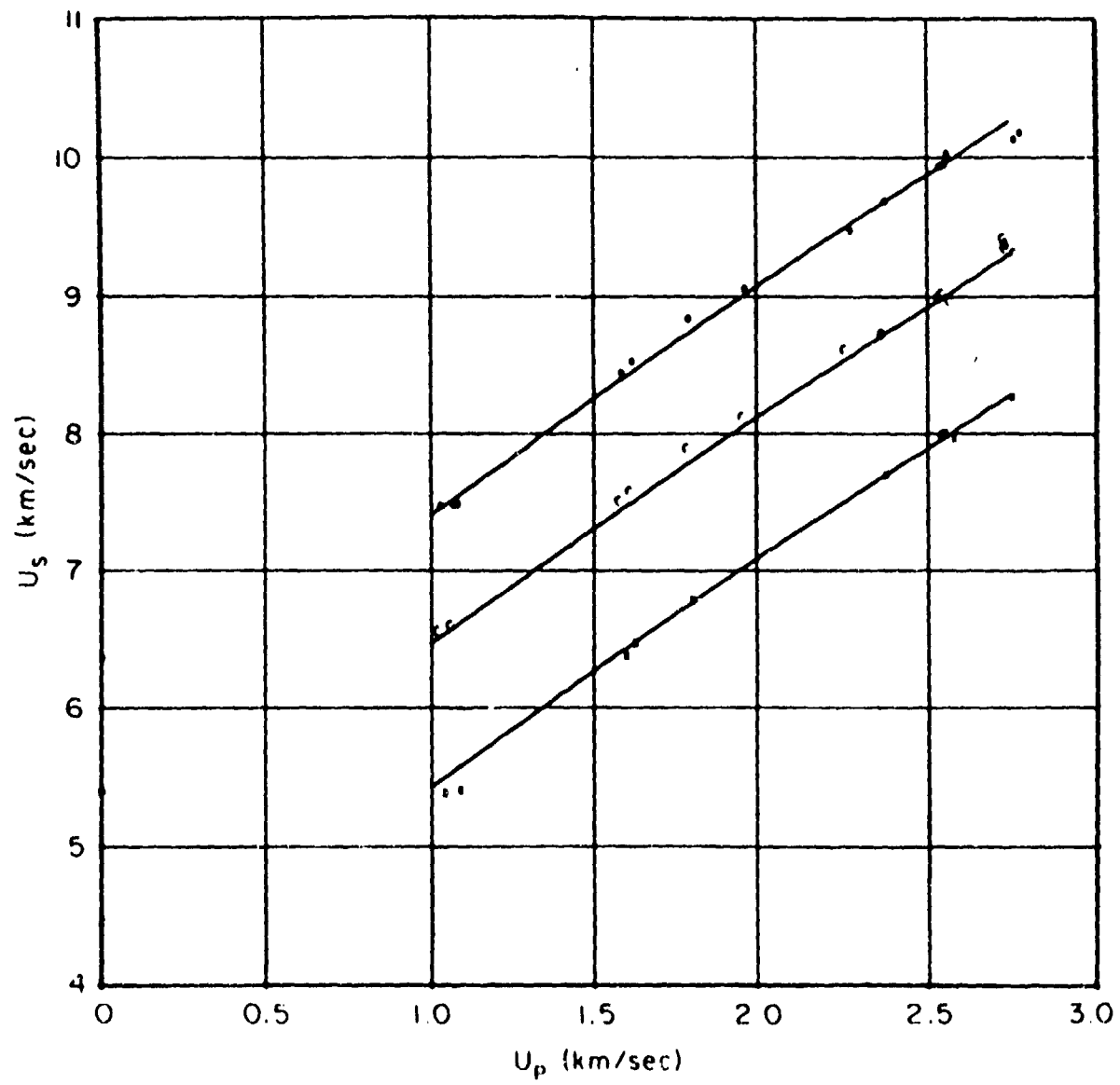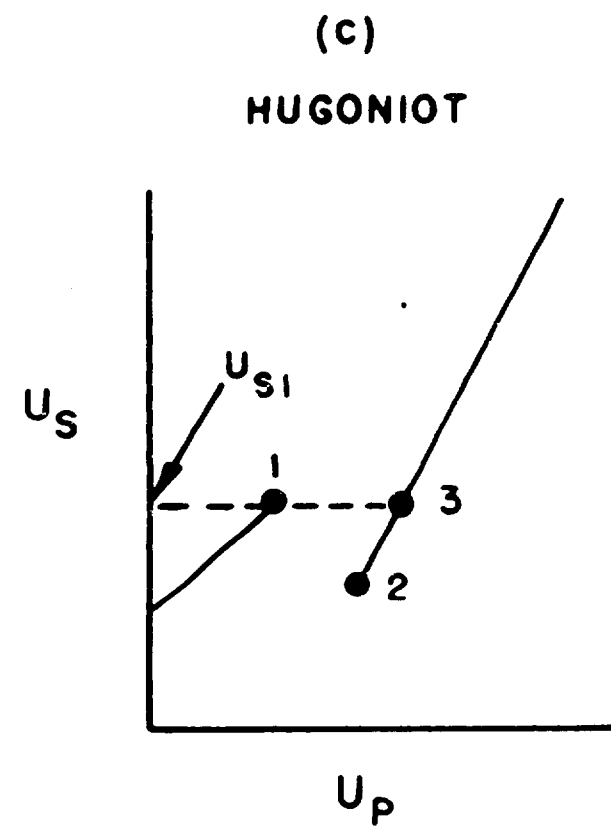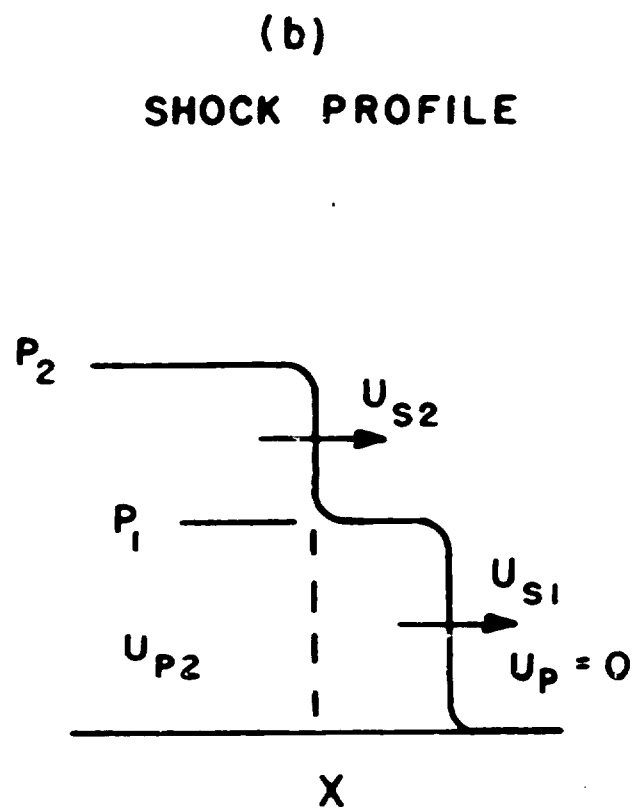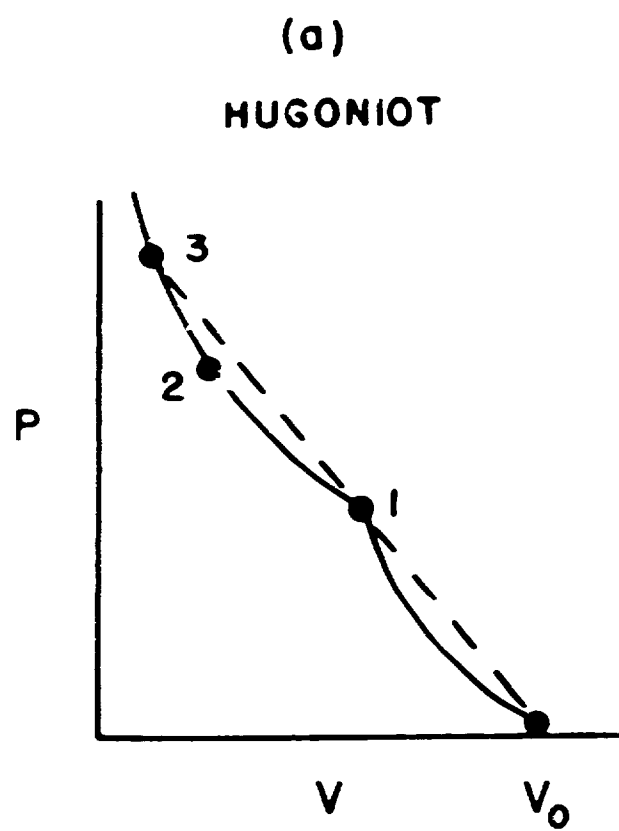
Figure IV.1

Figure IV.2

Figure IV.3

A

OVERDRIVEN
HUGONIOT

P

TRANSITION

EQUILIBRIUM

V

B

OBSERVED
HUGONIOT

P

EQUILIBRIUM

V

C

Us

Up
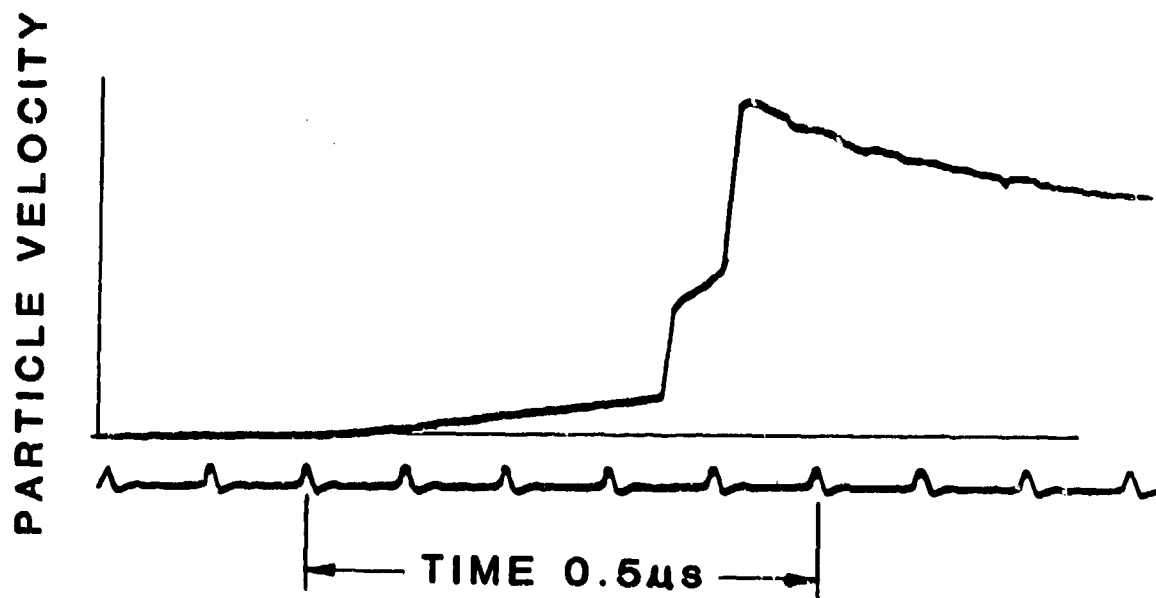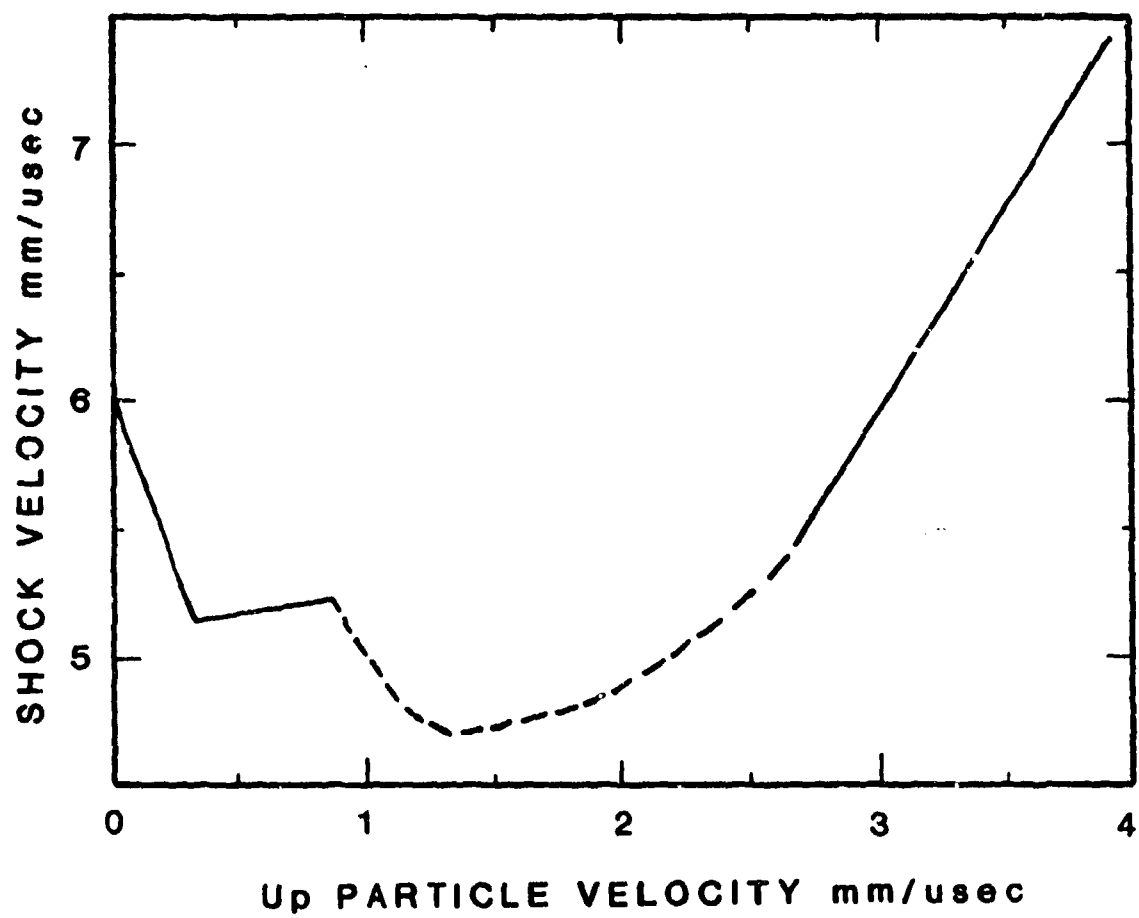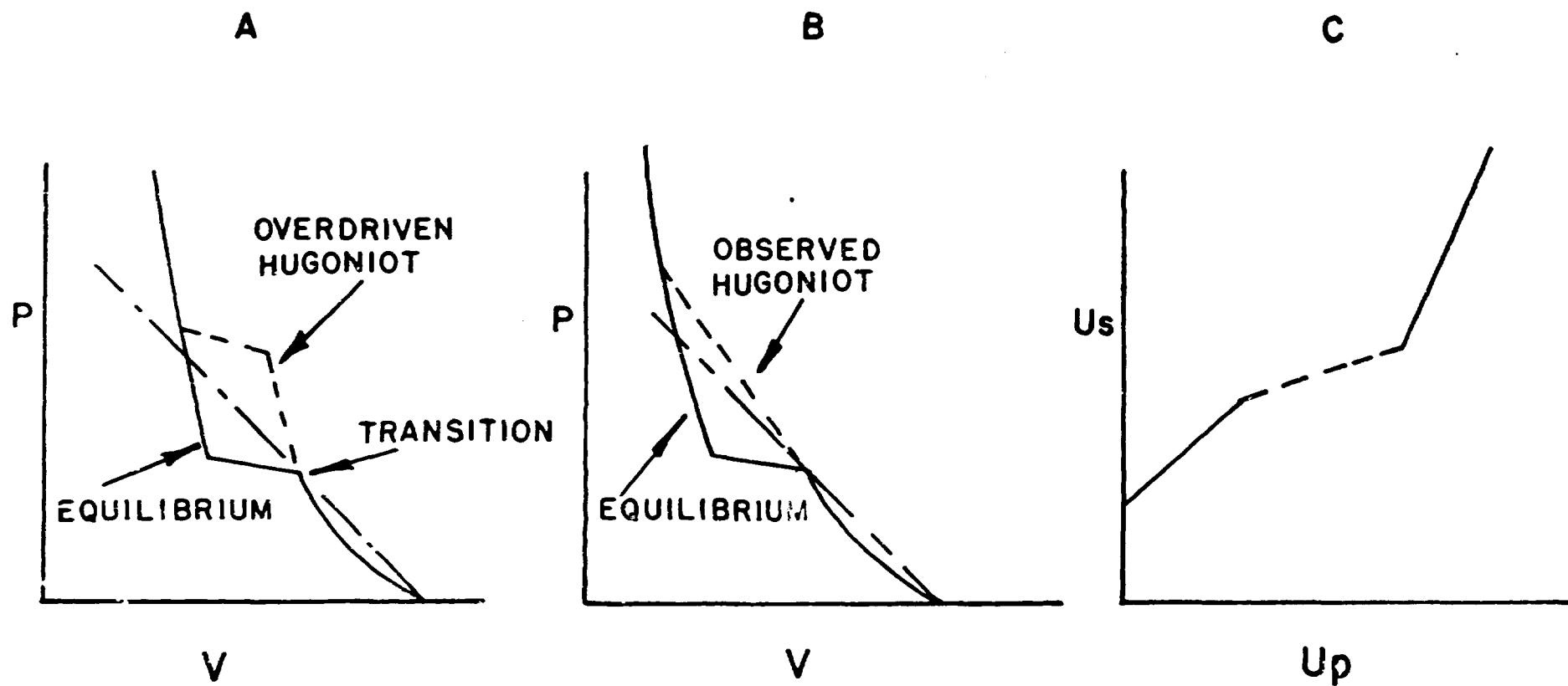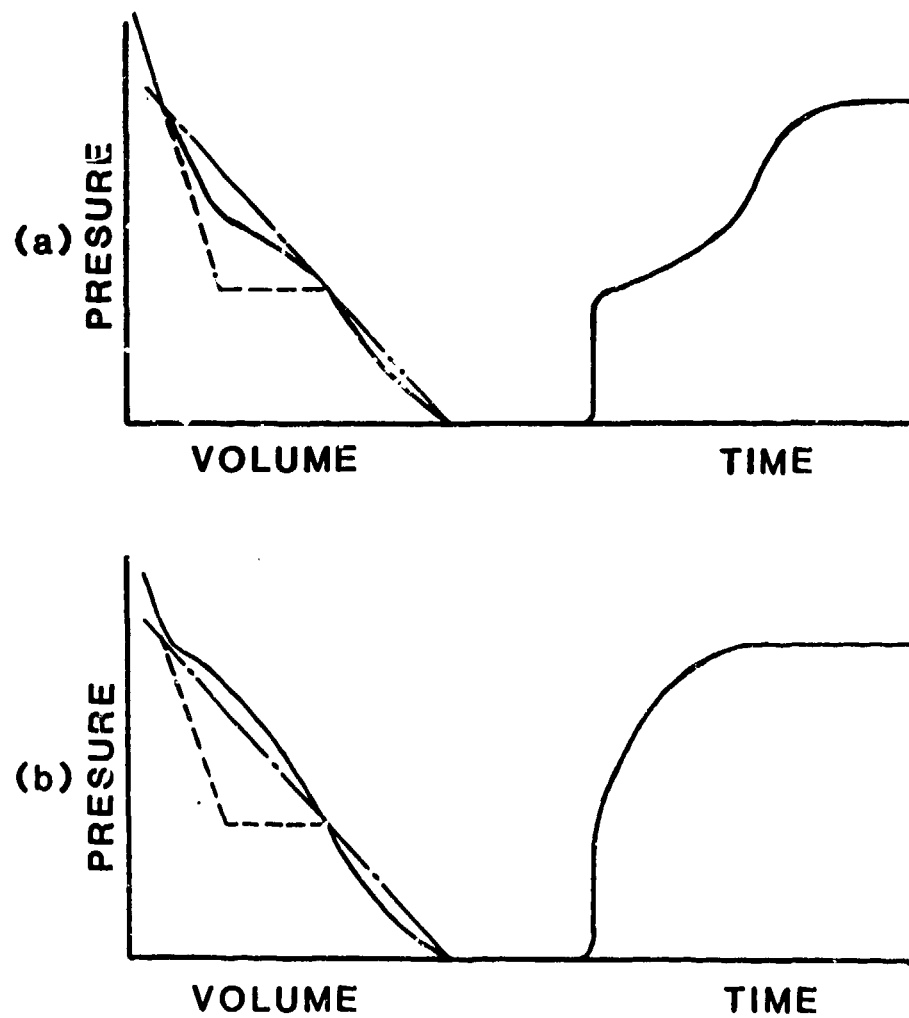
Figure IV.4

Figure IV.5

Figure IV.6

Figure IV.7

HUGONIOT C

TRANSITION POINT
ON
HUGONIOT A

CALCULATED
ISENTROPE
THAT SATISFIES
TEMPERATURE
AT TRANSITION

2S   ΔV   I

2H

HUGONIOT B

V_{OB} V_{OA}

V
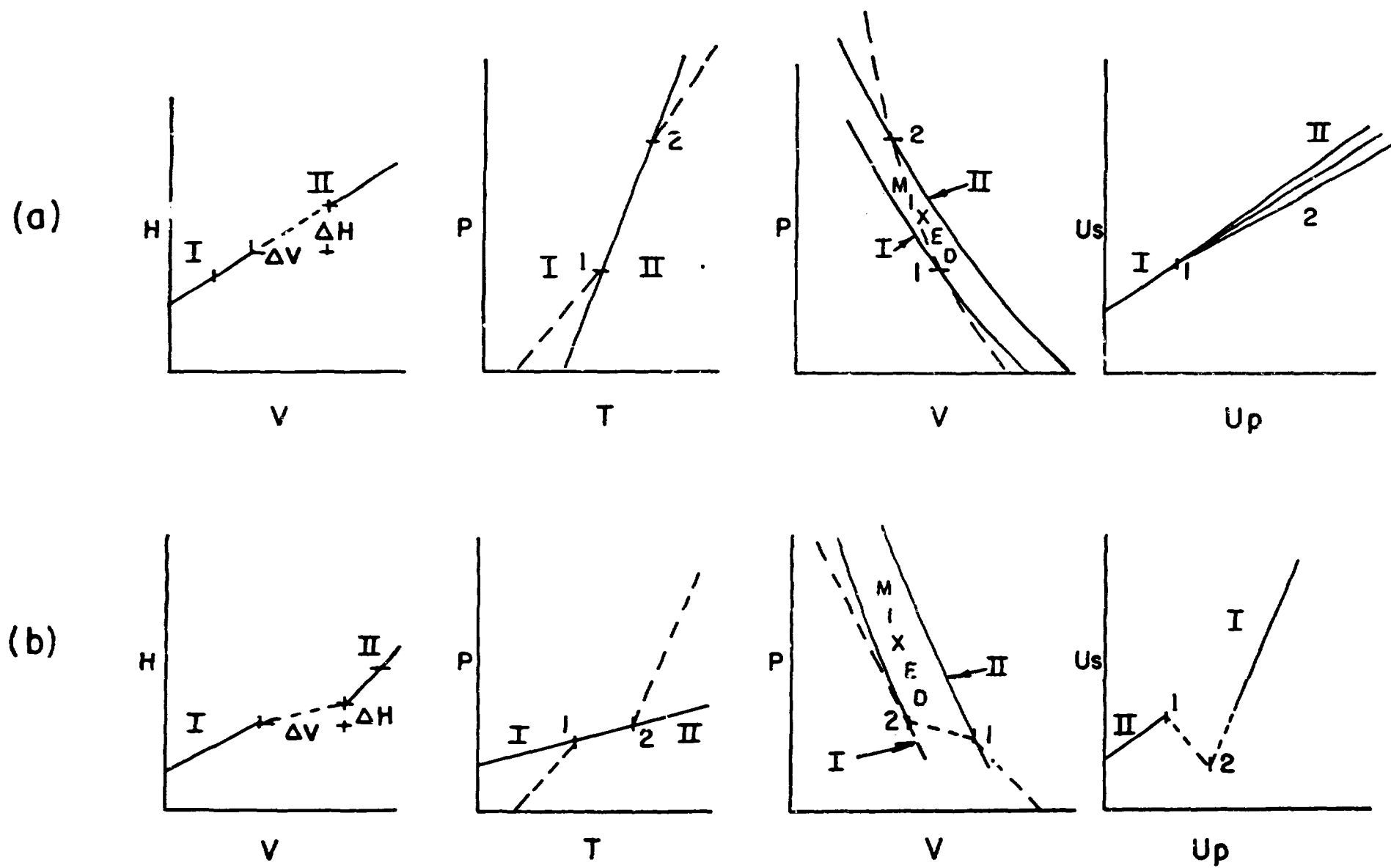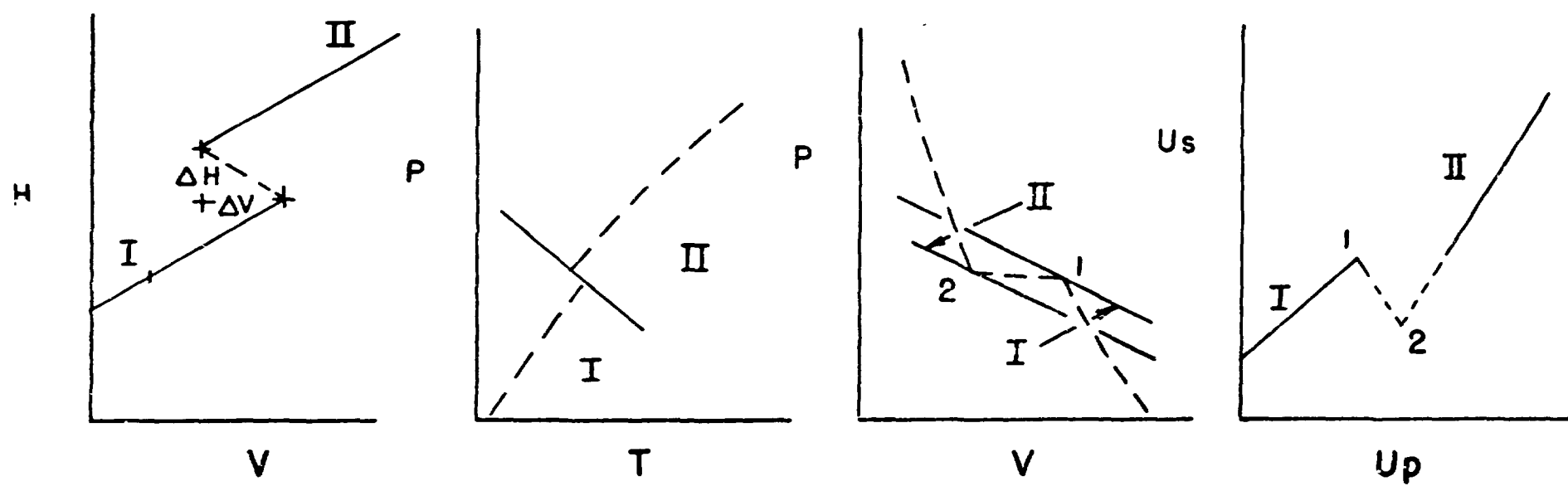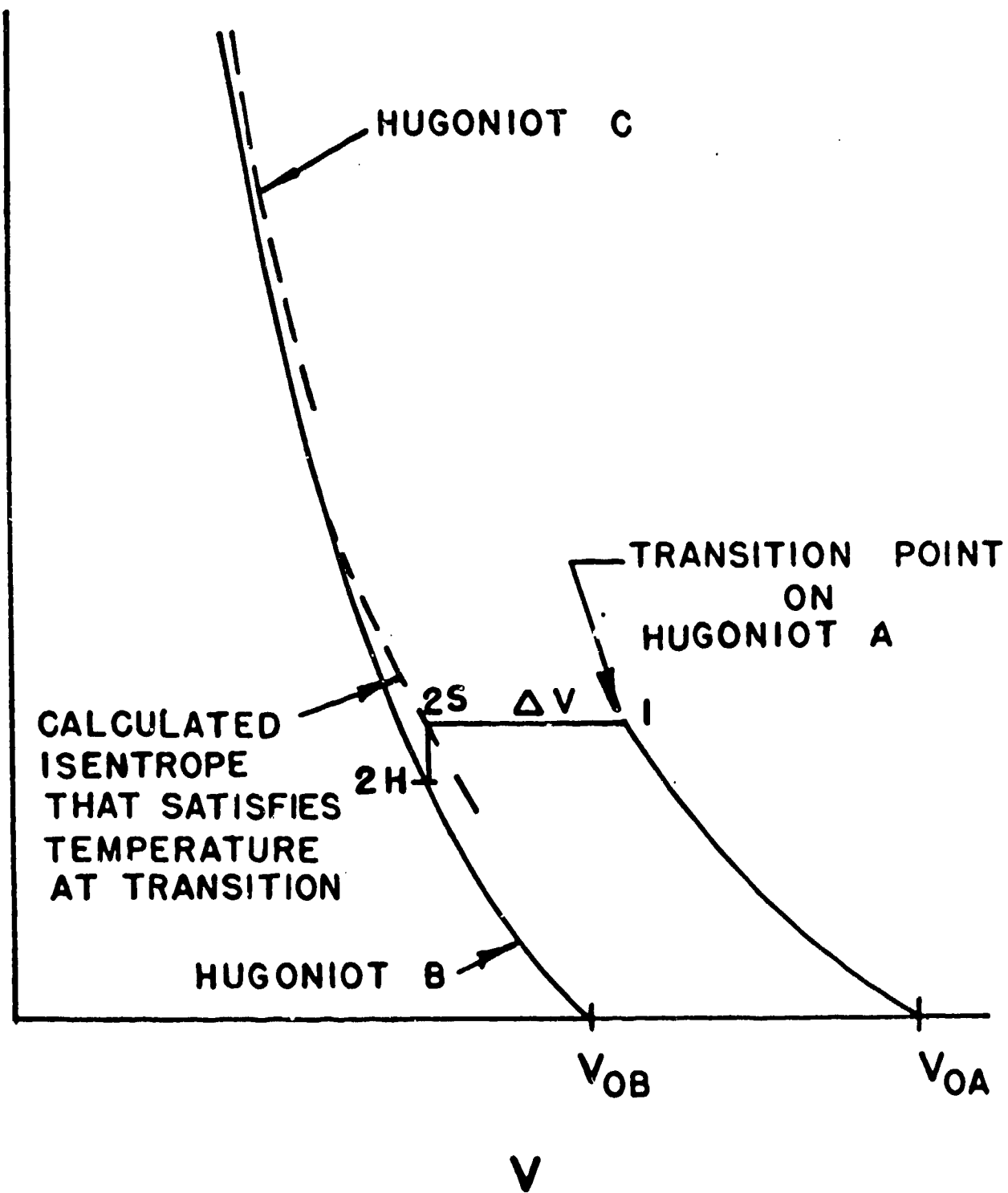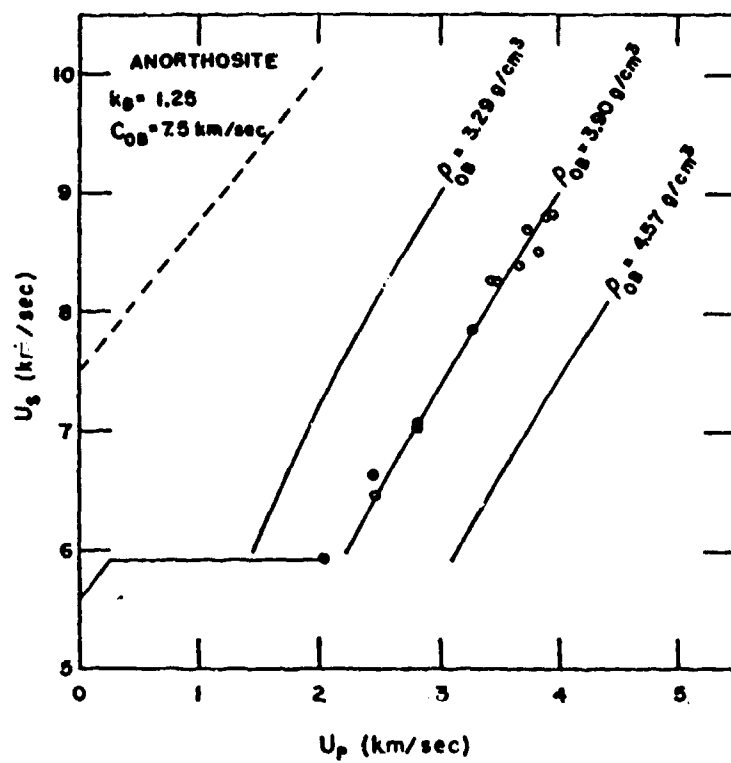
Figure IV.8
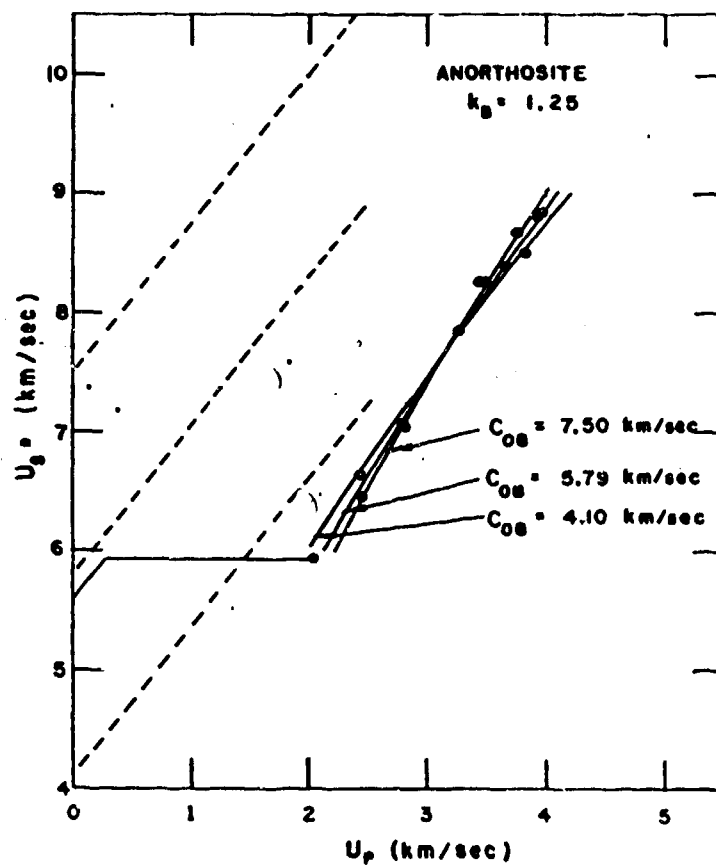
Figure IV.9

Figure IV.10
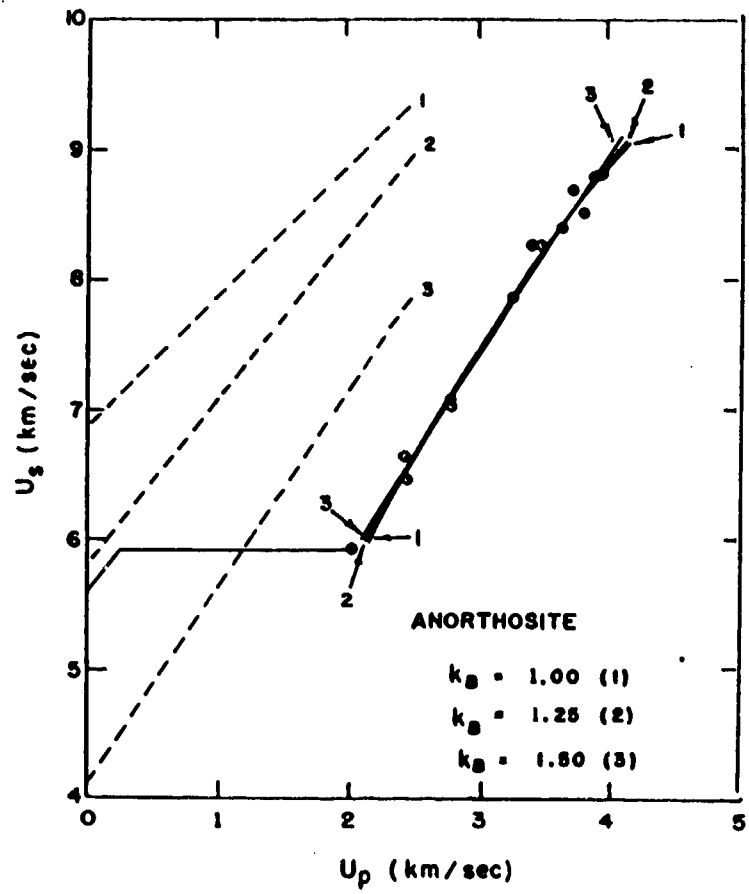
Figure IV.11

Figure IV.13

Figure V.1

ANNEALED ARMCO IRON
24.74 MM THICK

$D_{10} = 6.04$ MM/μ SEC.
$D_{21} = 5.08$ MM/μ SEC.
$D_{32} = 3.08$ MM/μ SEC.
$P_1 = 6.7$ KILOBARS
$P_2 = 131$ KILOBARS
$P_3 = 167$ KILOBARS

$2u_3 = 0.930$ MM/μ SEC.

$2u_2 = 0.654$ MM/μ SEC.

$2u_1 = 0.0285$ MM/μ SEC.

F_1

$+F_2$

DISPLACEMENT OF PINS FROM FREE SURFACE, MM

ARRIVAL TIMES AT PINS IN μ SEC t=0 AT H E-TARGET PLATE INTERFACE

Figure V.3

Figure V.4

MYLAR 6 μ m THICK

ELECT. PINS
(Typical of nine)

COAX
CONNECTOR
TO P.F.N.

50 ohms

TA
BASE

Cu GROUND PLANE

PIN CAP

SAMPLE

TARGET END VIEW

Figure V.5

(a)

←—6.4mm

PLASTIC SABOT

IMPACTOR PLATE

(b)

1st Pulse

5μsec

2nd Pulse

(c)

←100 nsec

FIDUCIAL   DELAYED DOWN PIN   UP PIN

(d)

Figure V.6

FLASH BLOCK TRANSPARENT

(a)   (b)   (c)

BASE PLATE

GAP   SAMPLE   SHIM   GAP

Figure V.7

ACRYLIC FLASH BLOCKS

VIEWING SLITS

ACRYLIC FLASH BLOCKS

SLIT PLATE

0.75 CM

0.2 CM

0.2 CM

0.75 CM

0.5 CM

Figure V.8

Figure V.9

Figure V.10

HUGONIOT DATA FROM SHOCK-PARTICLE VELOCITY EXPERIMENTS

Figure V.11

Figure V.12

MULTIPLE SLITS
OVER EACH SET

GAS BOX

A

B   B

BASE PLATE

A

SECTION AA

SLIT PLATE

LUCITE
FLASH-GAP
BLOCKS

SECTION BB

Figure V.13

AI   H

D   J

F   AI

K   A

1 μ sec
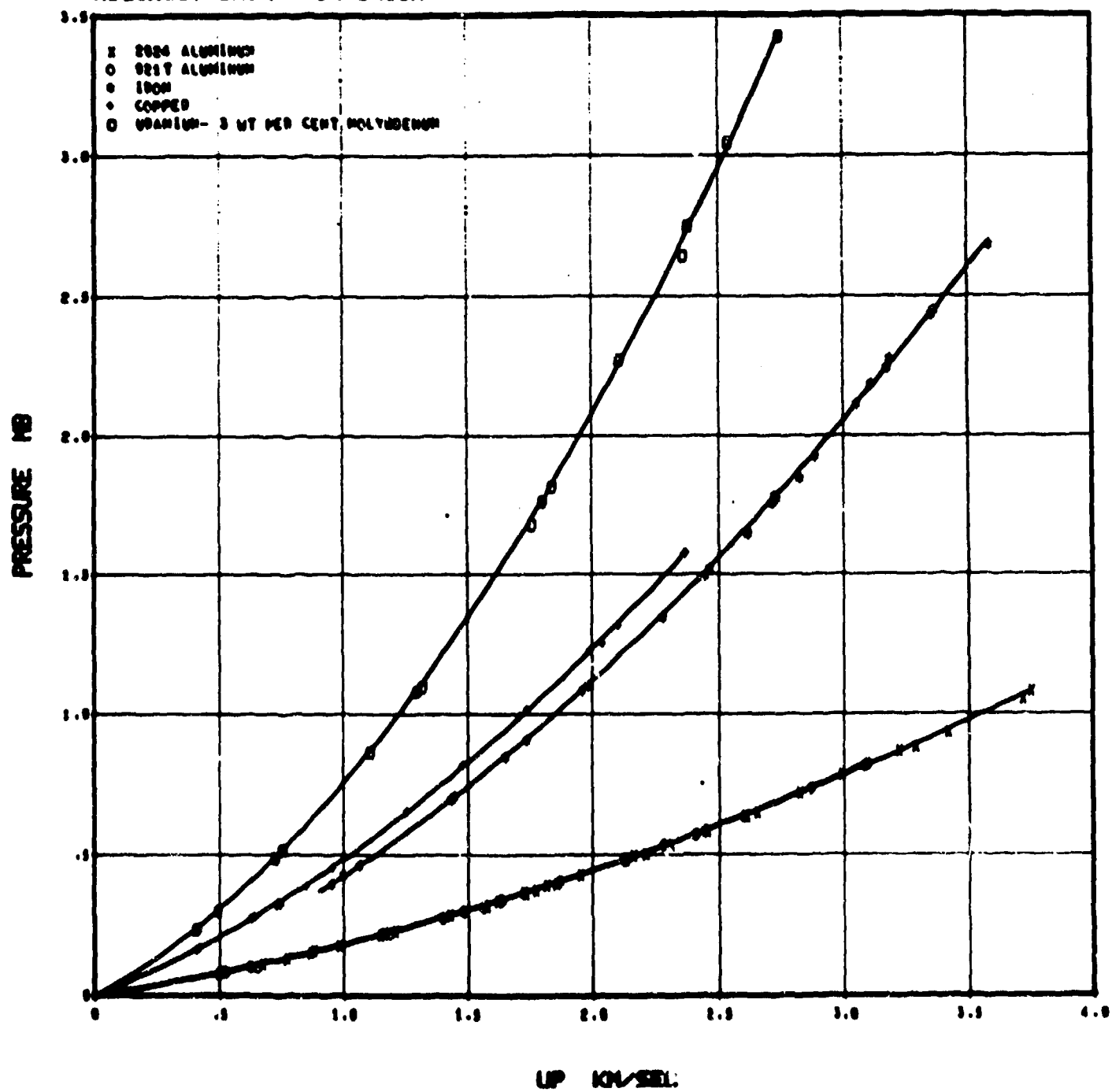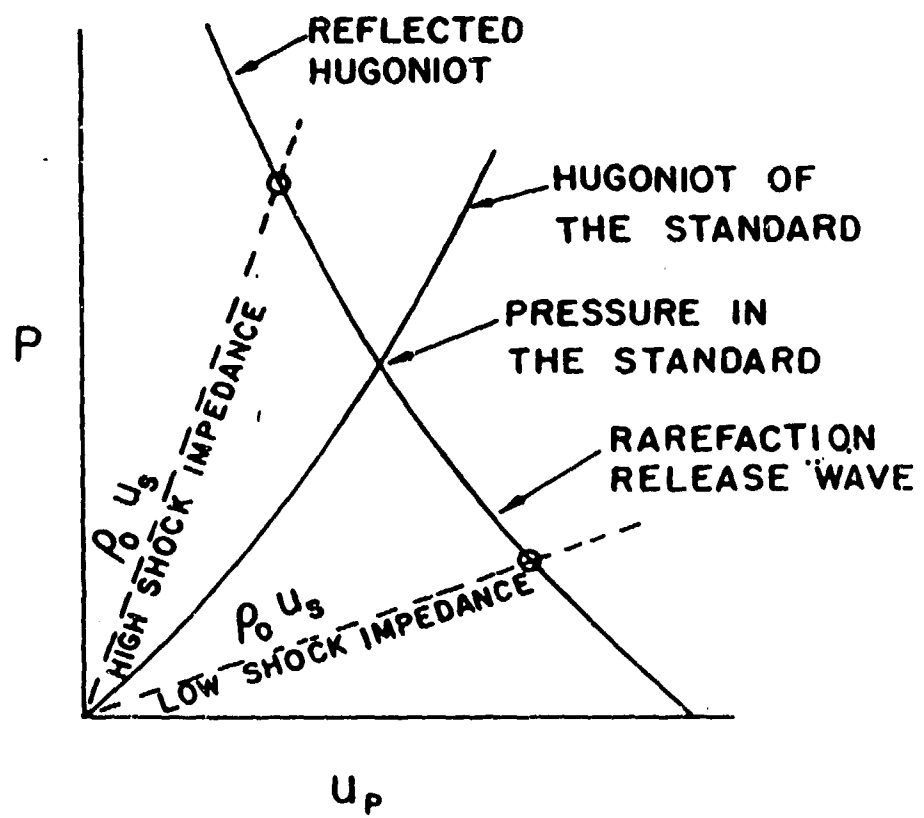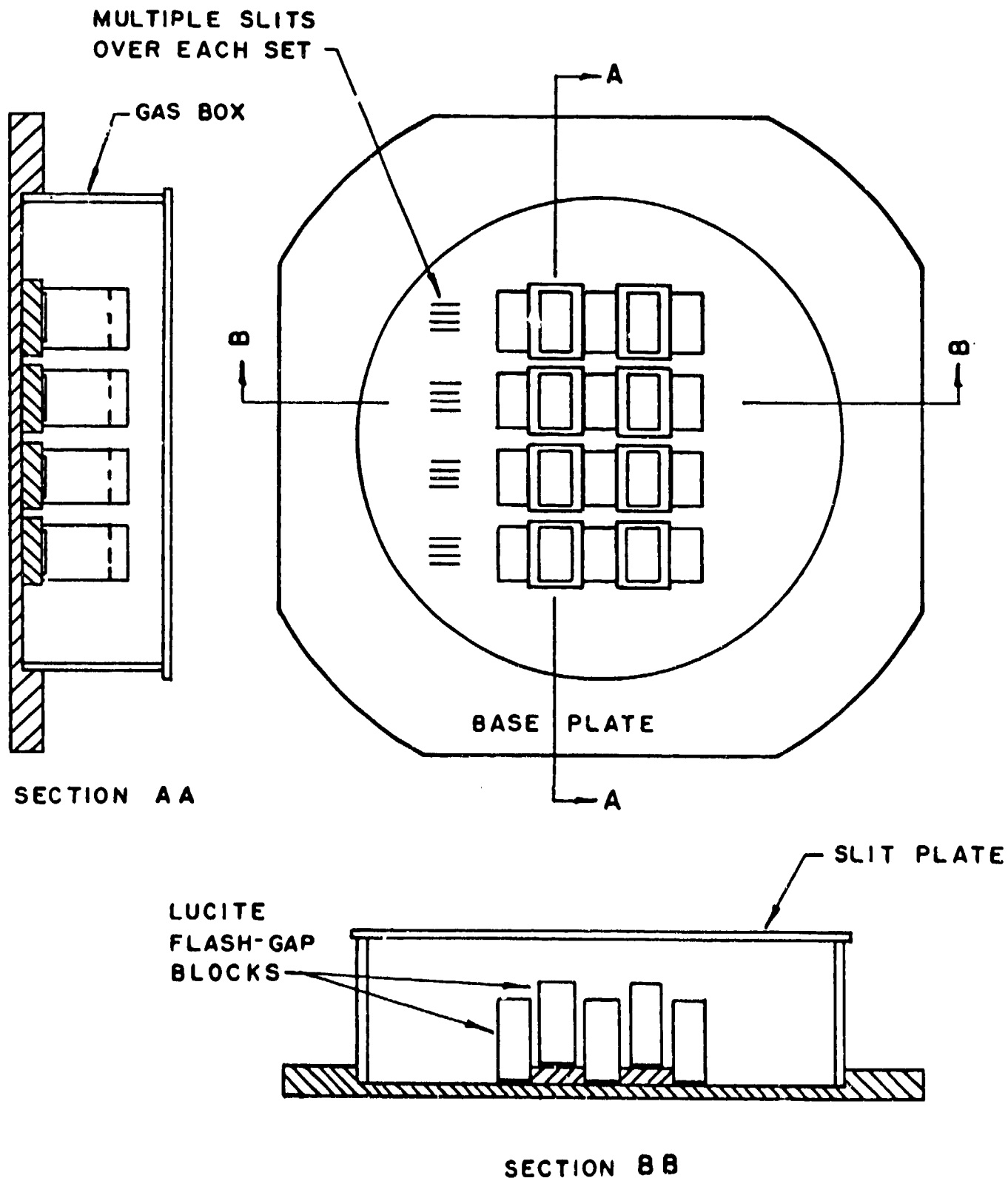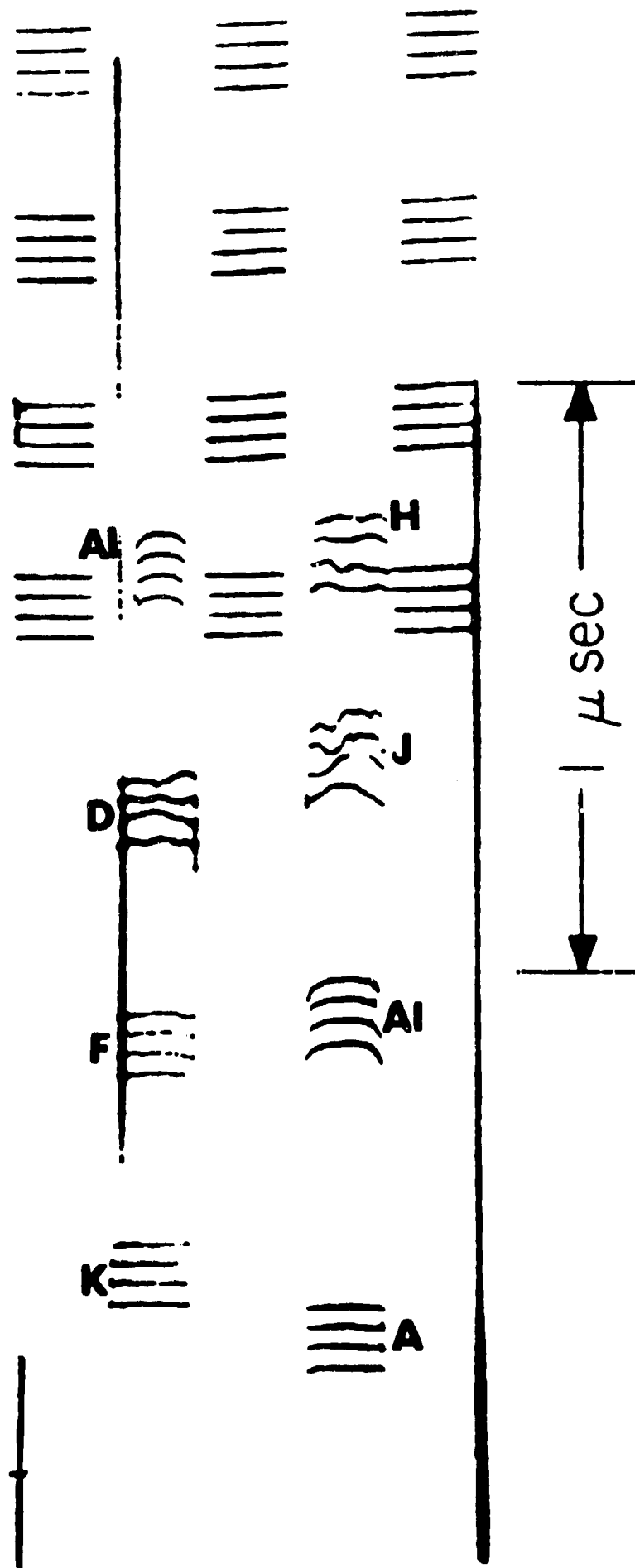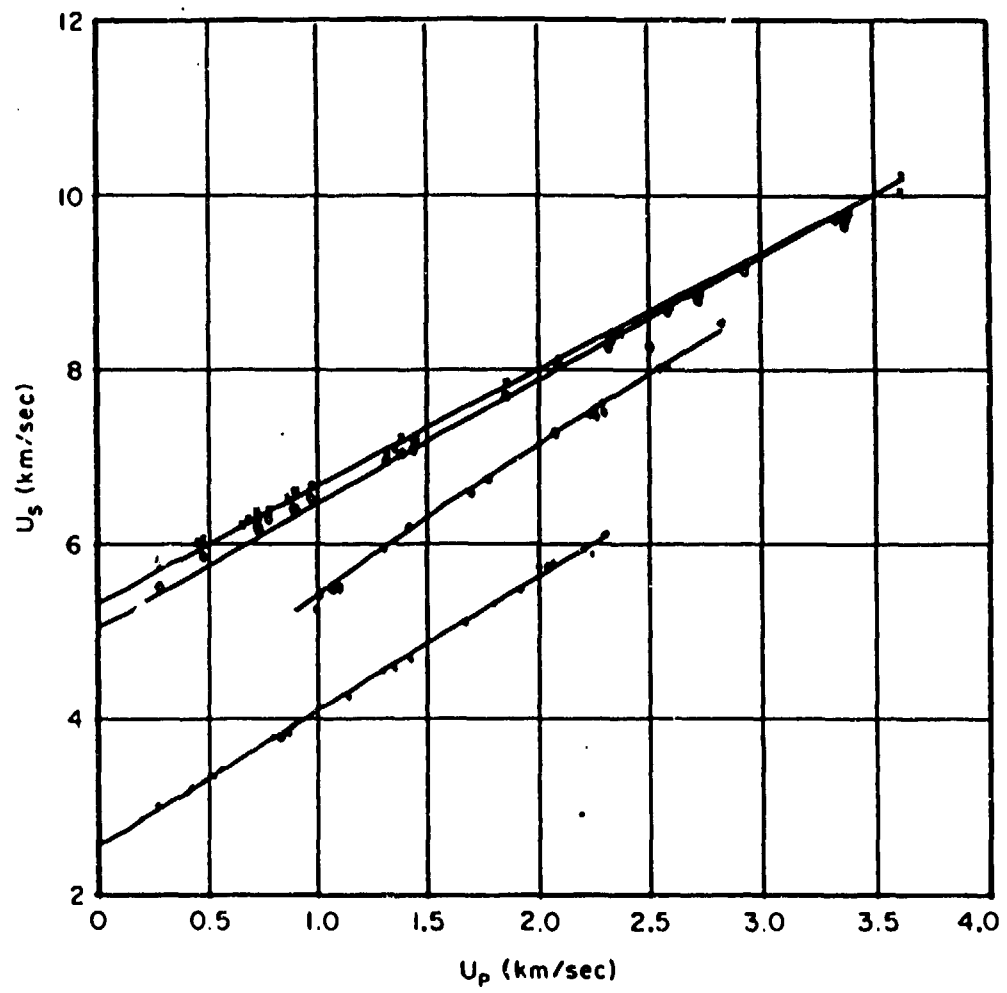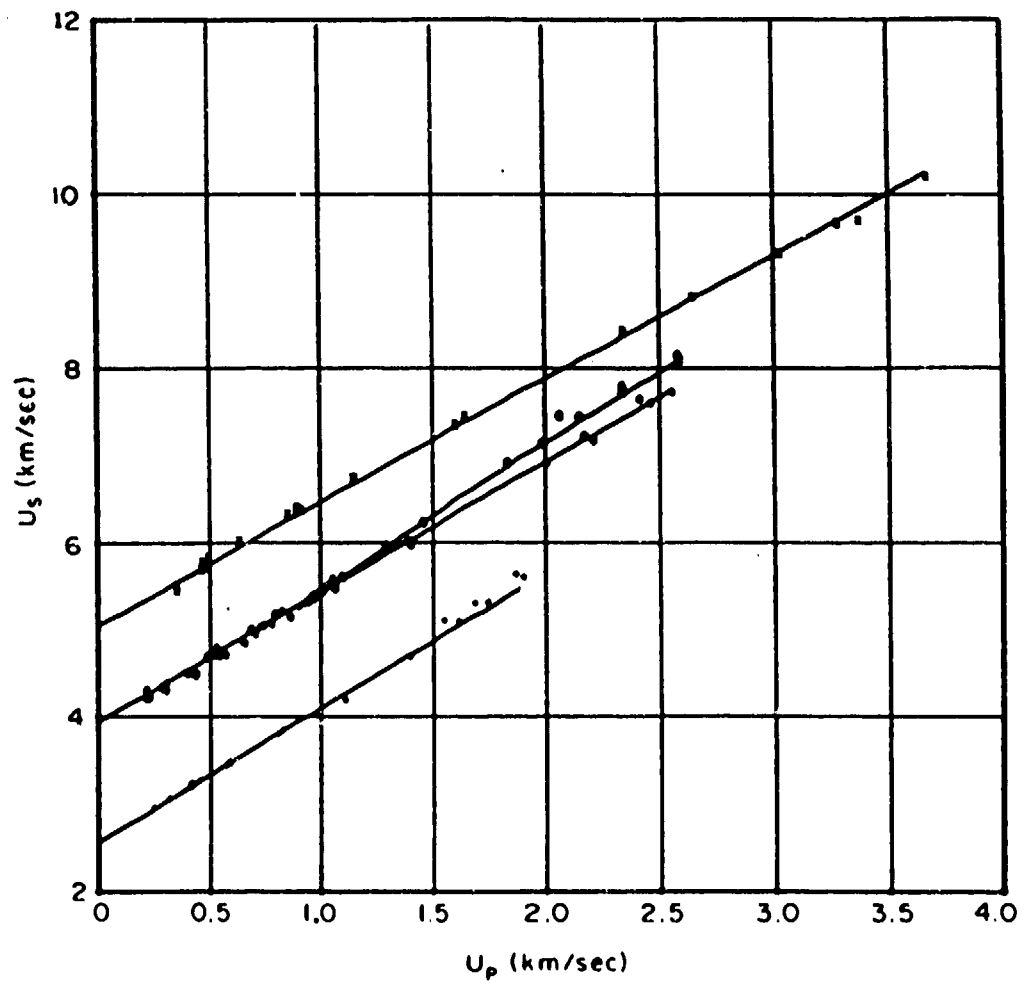
Figure V.15
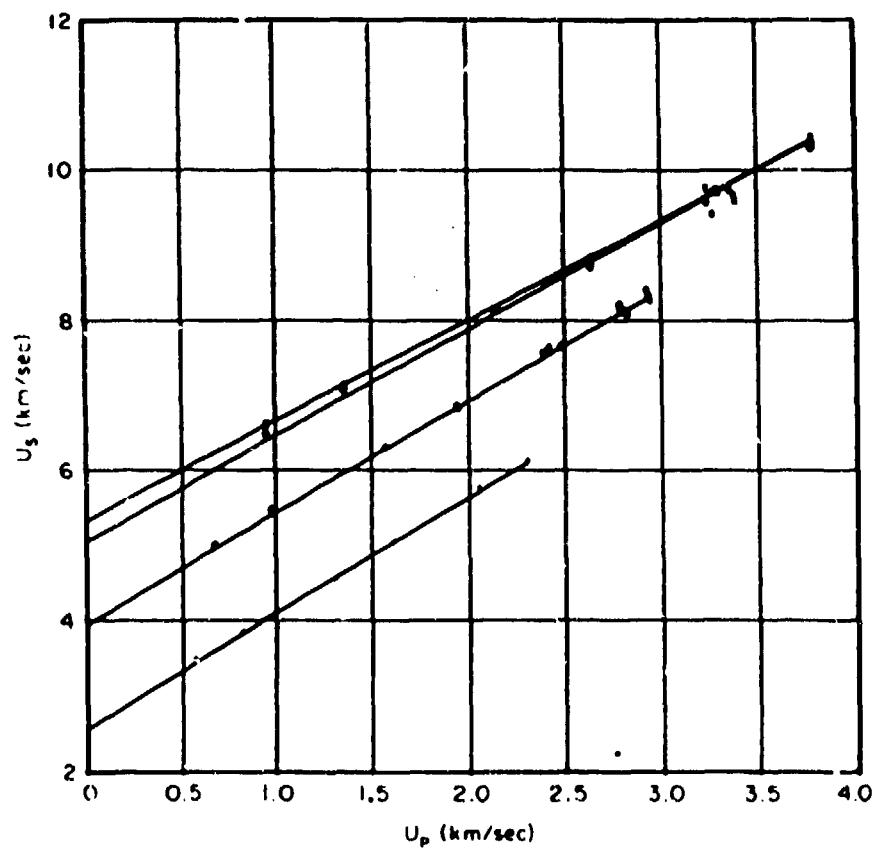
Figure V.16

Figure V.17
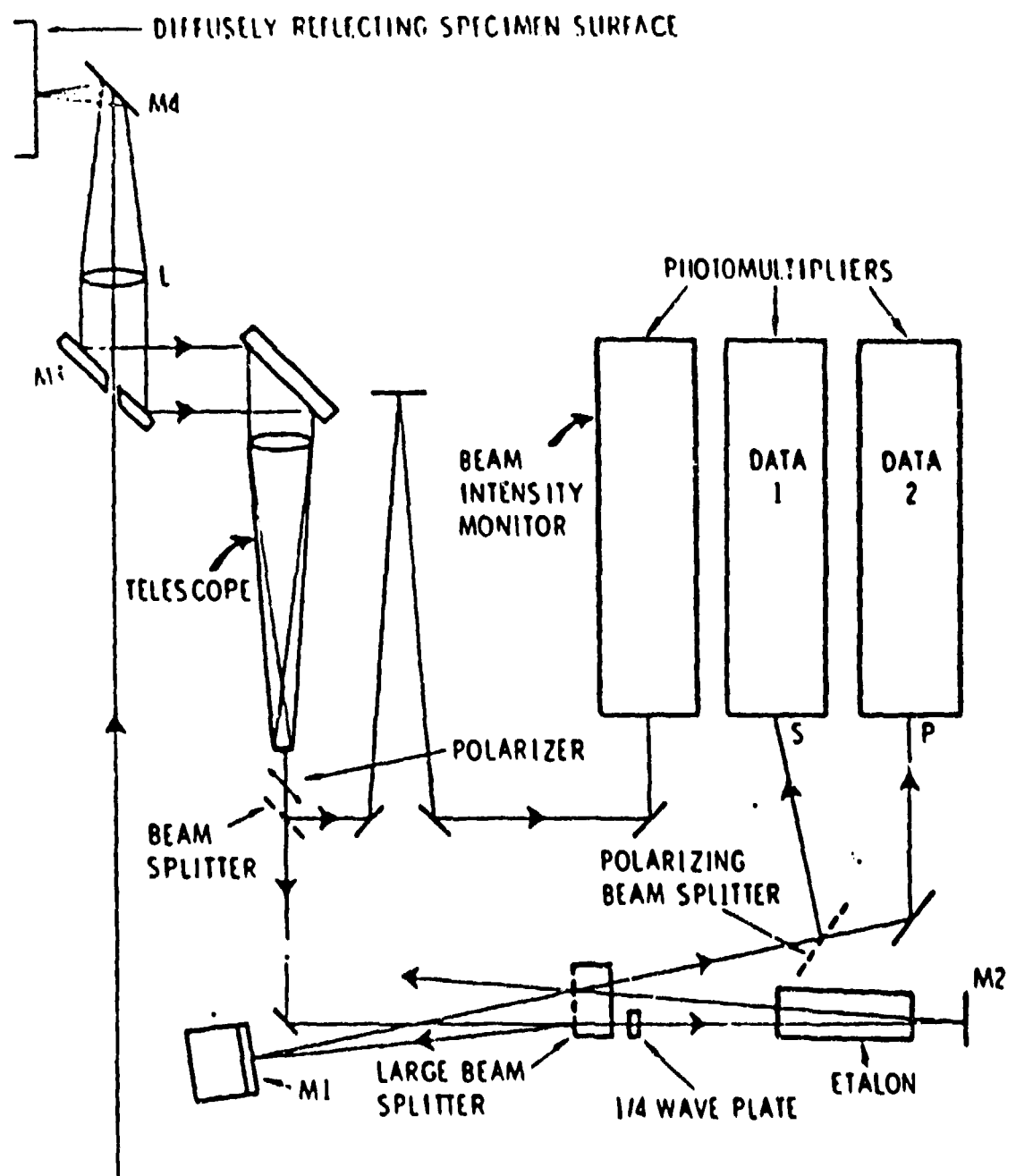
Figure V.18
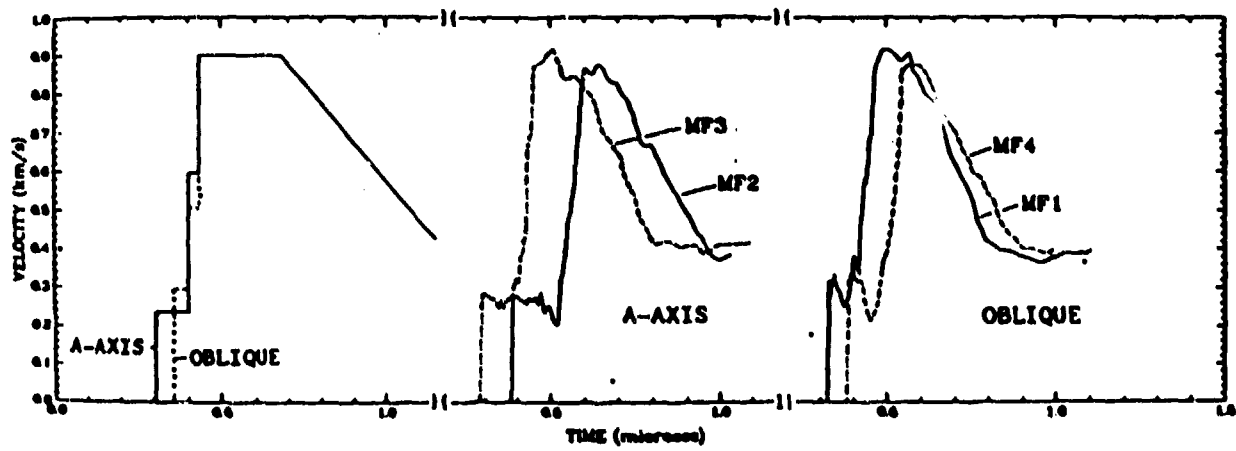
Figure V.19
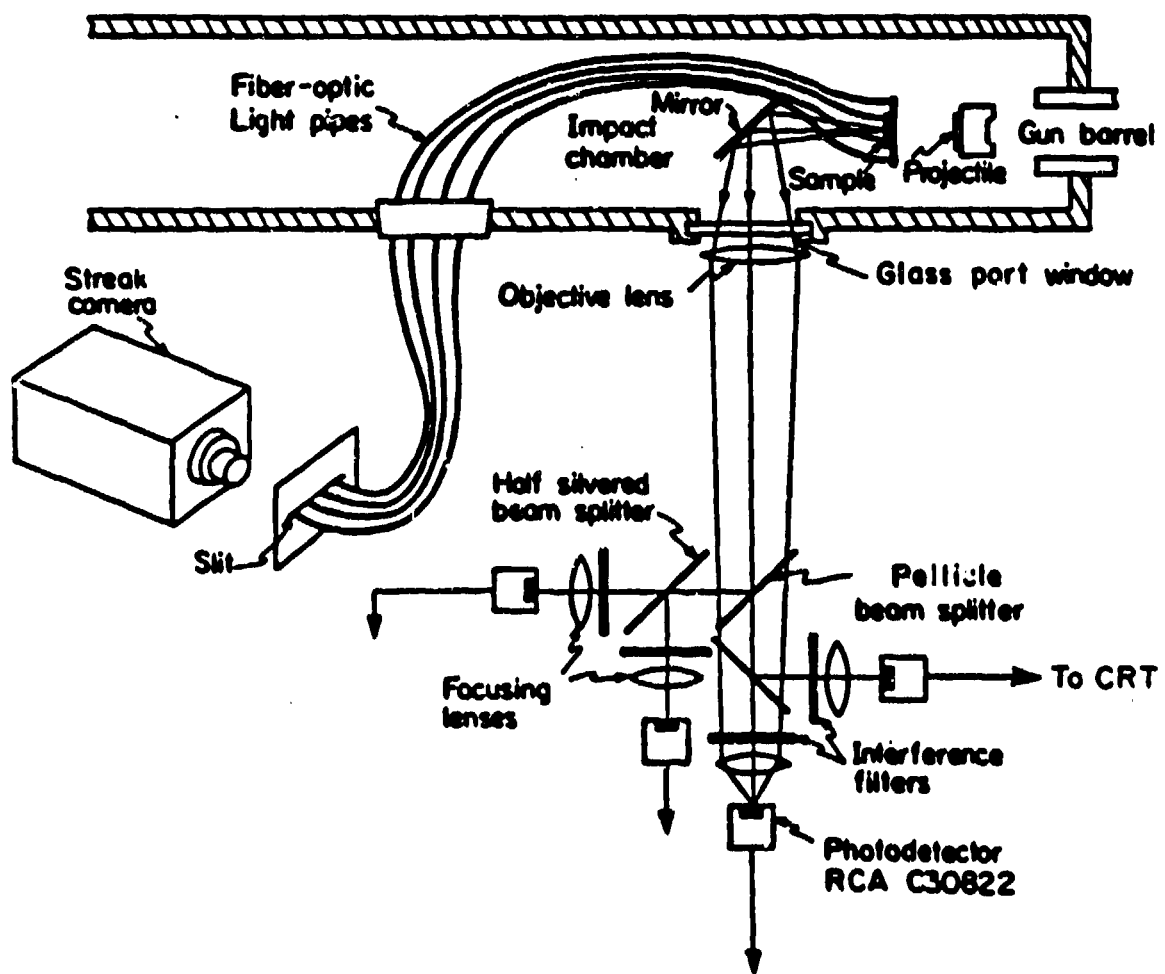
Figure V.20
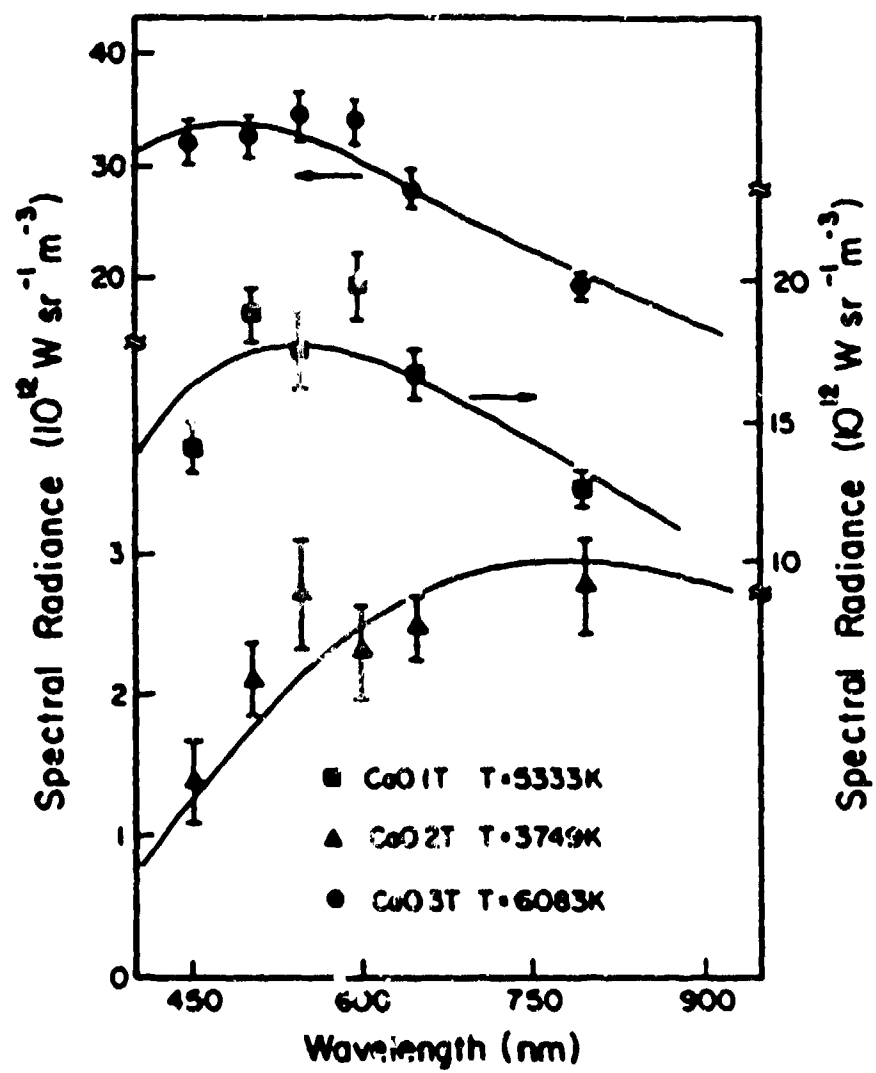
Figure V.21
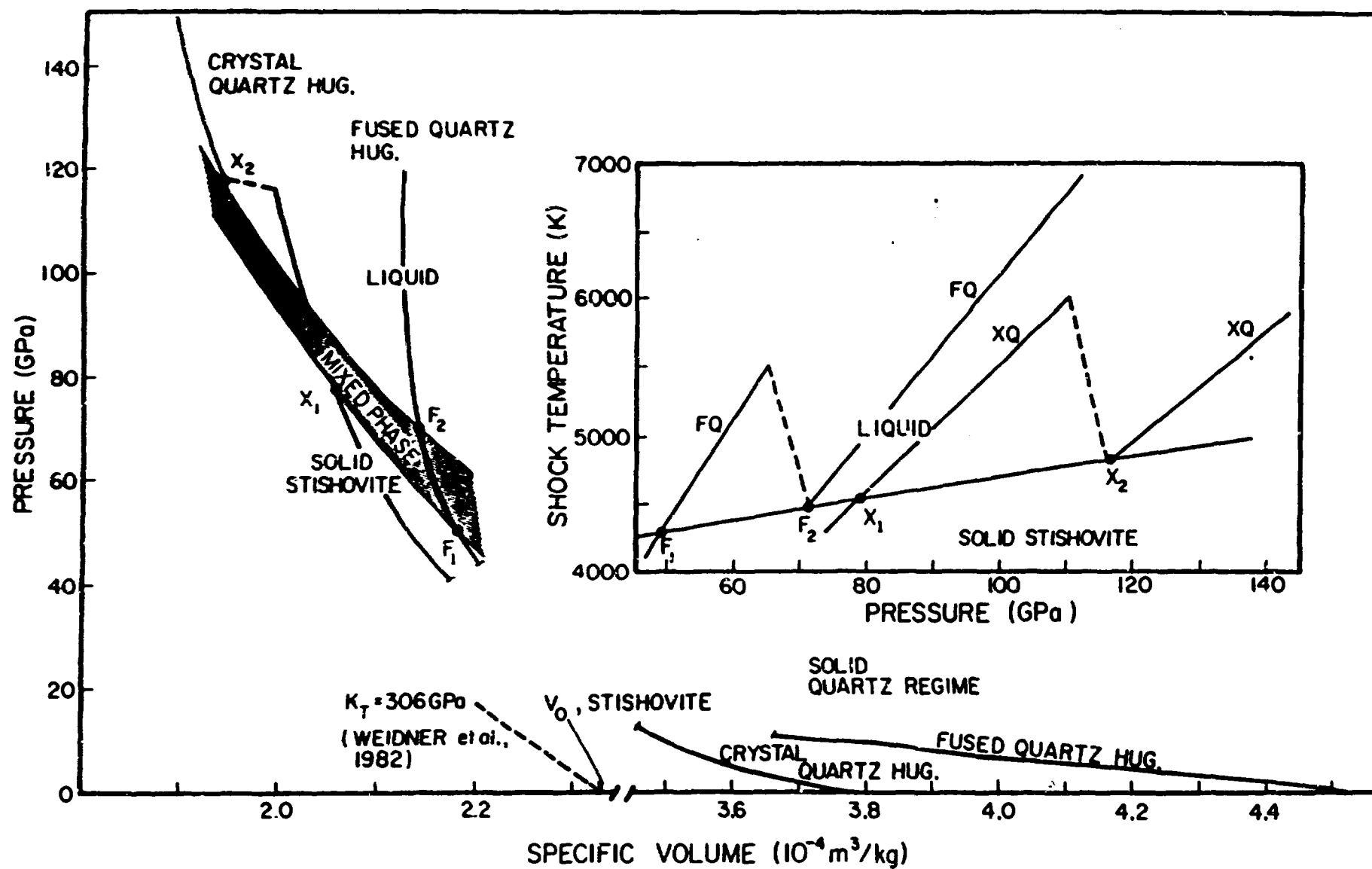
Figure V.22
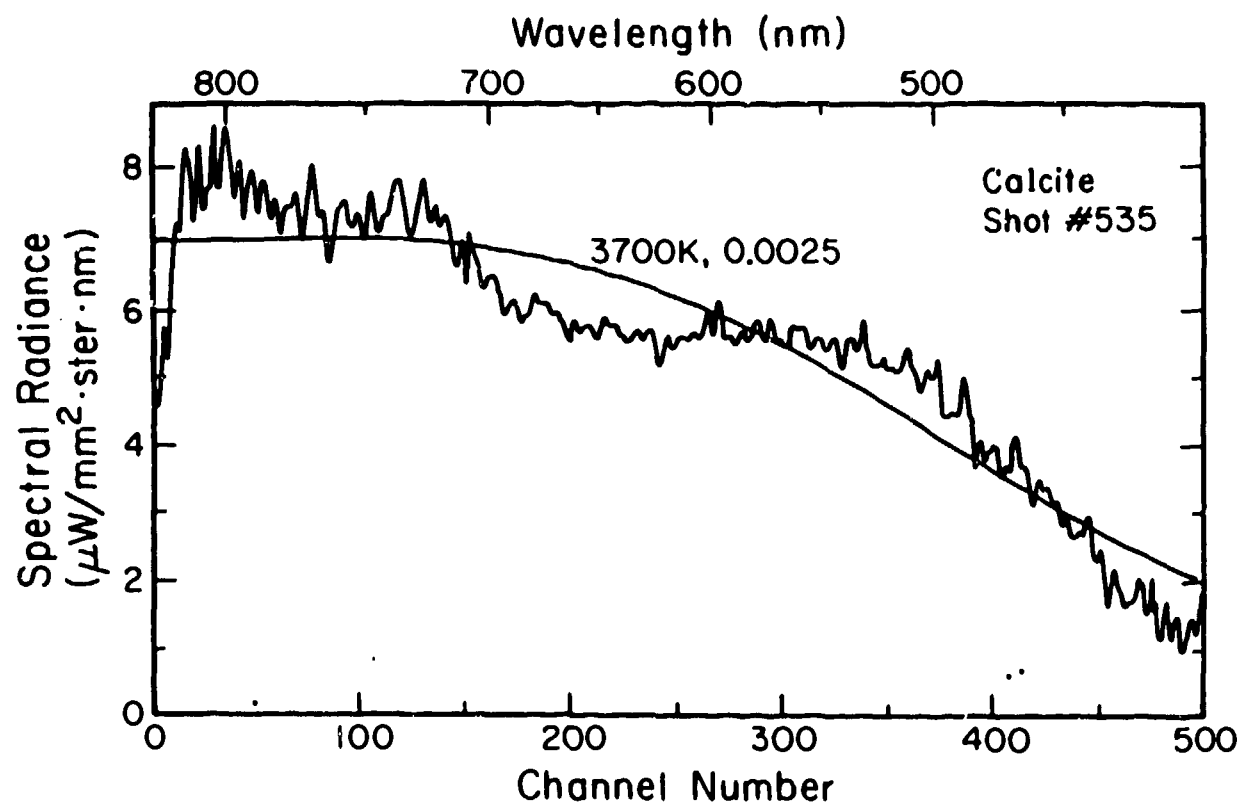
Figure V.23
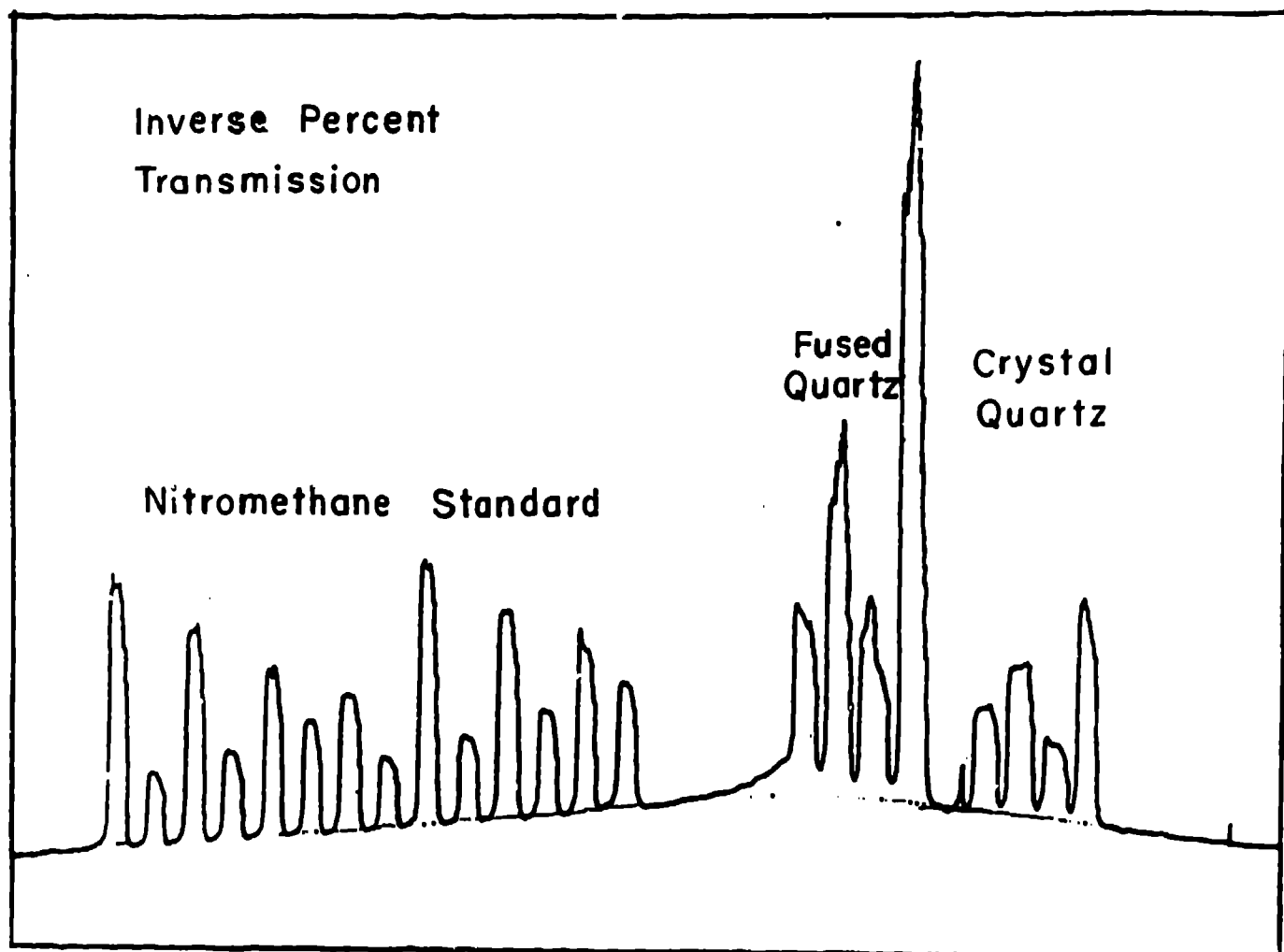
Figure V.24
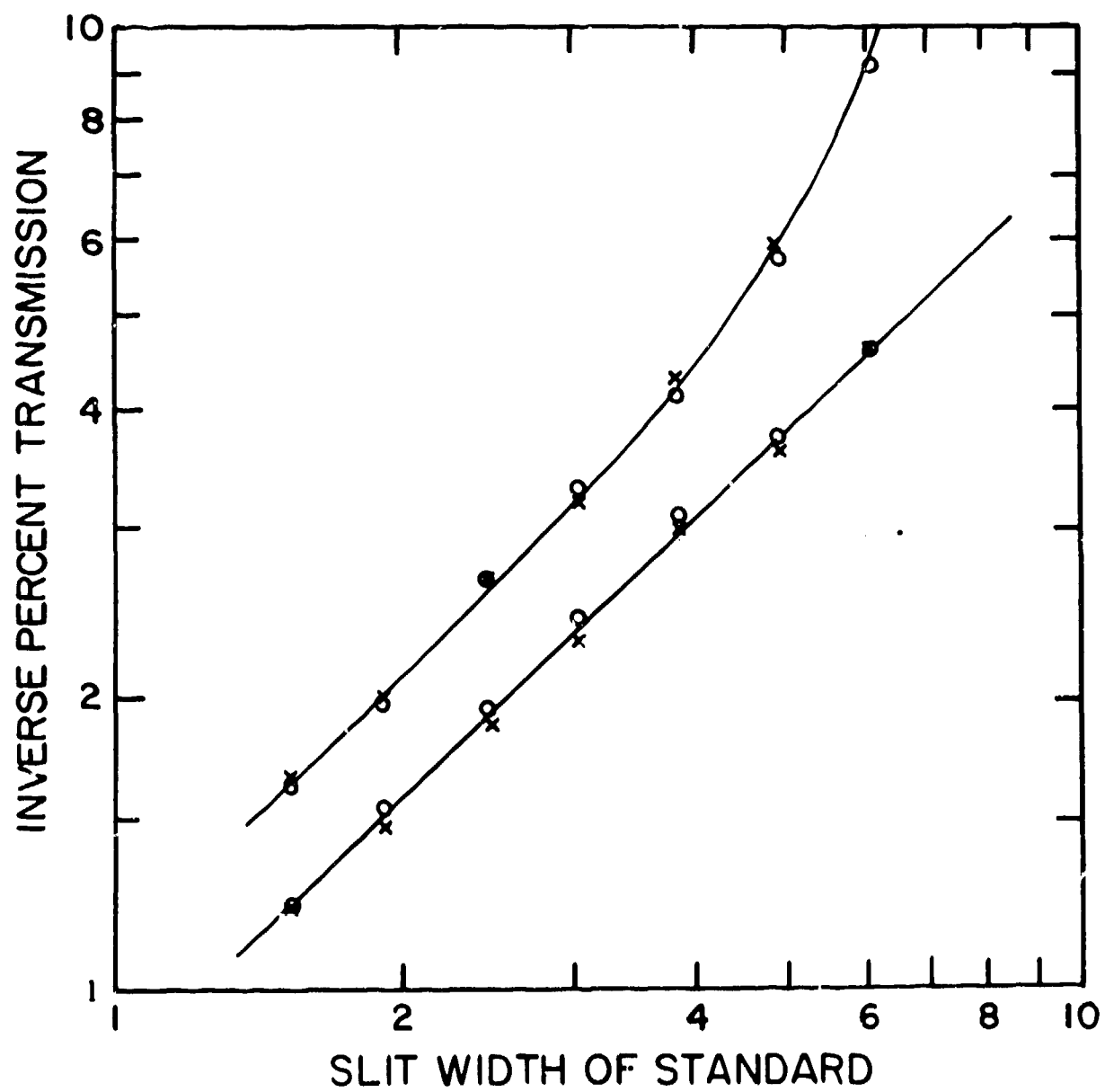
Figure V.25
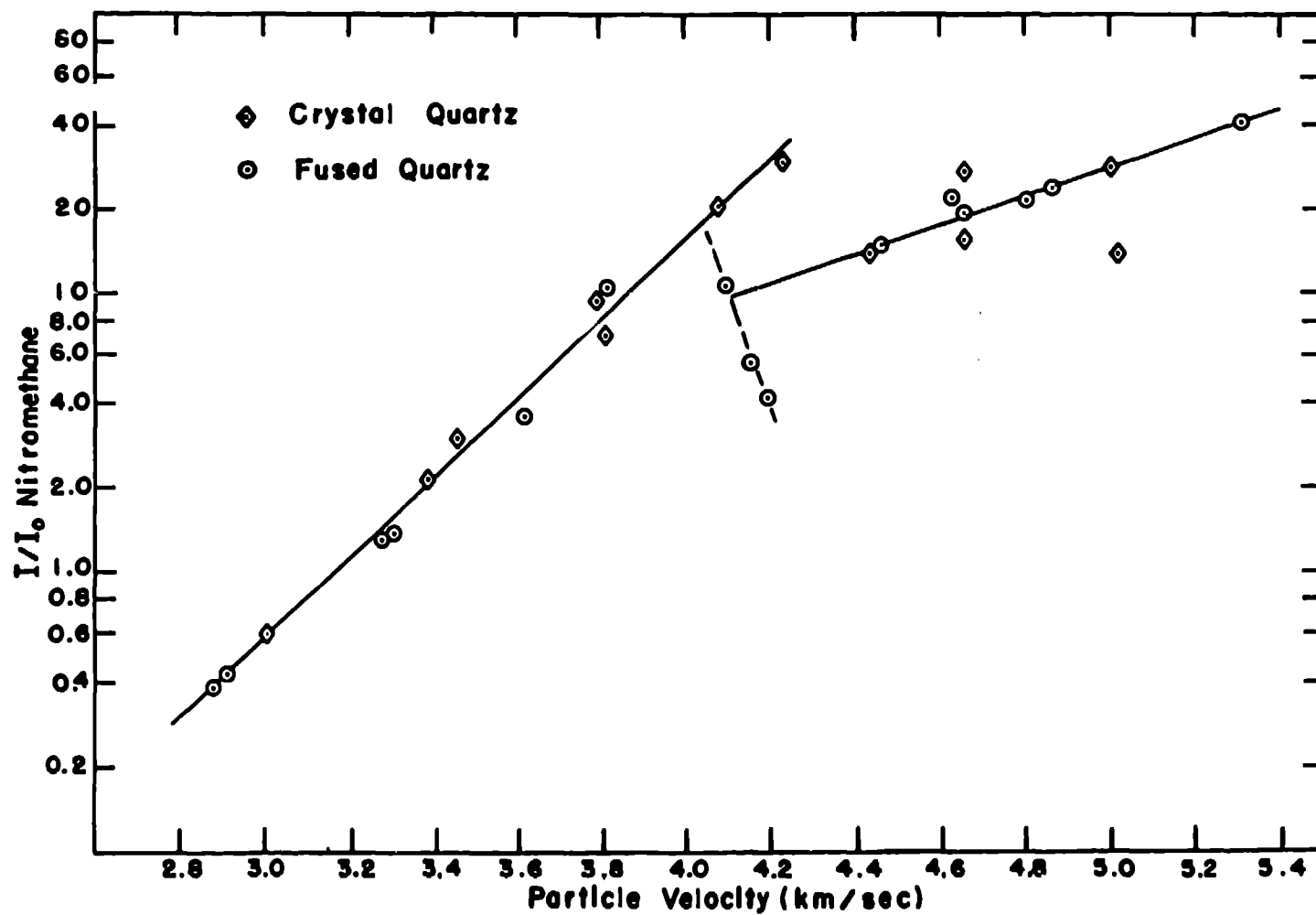
Figure V.26
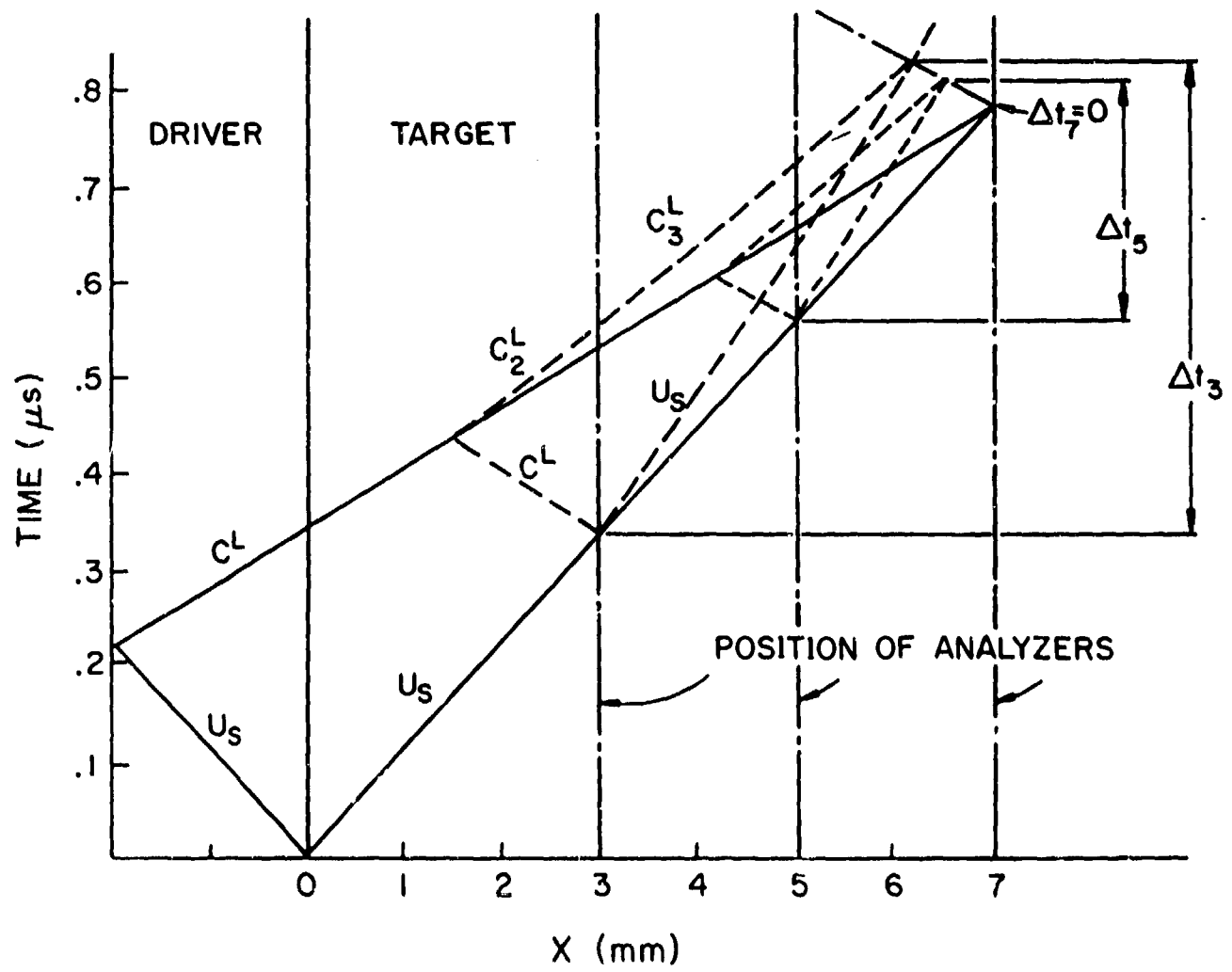
Figure V. 27
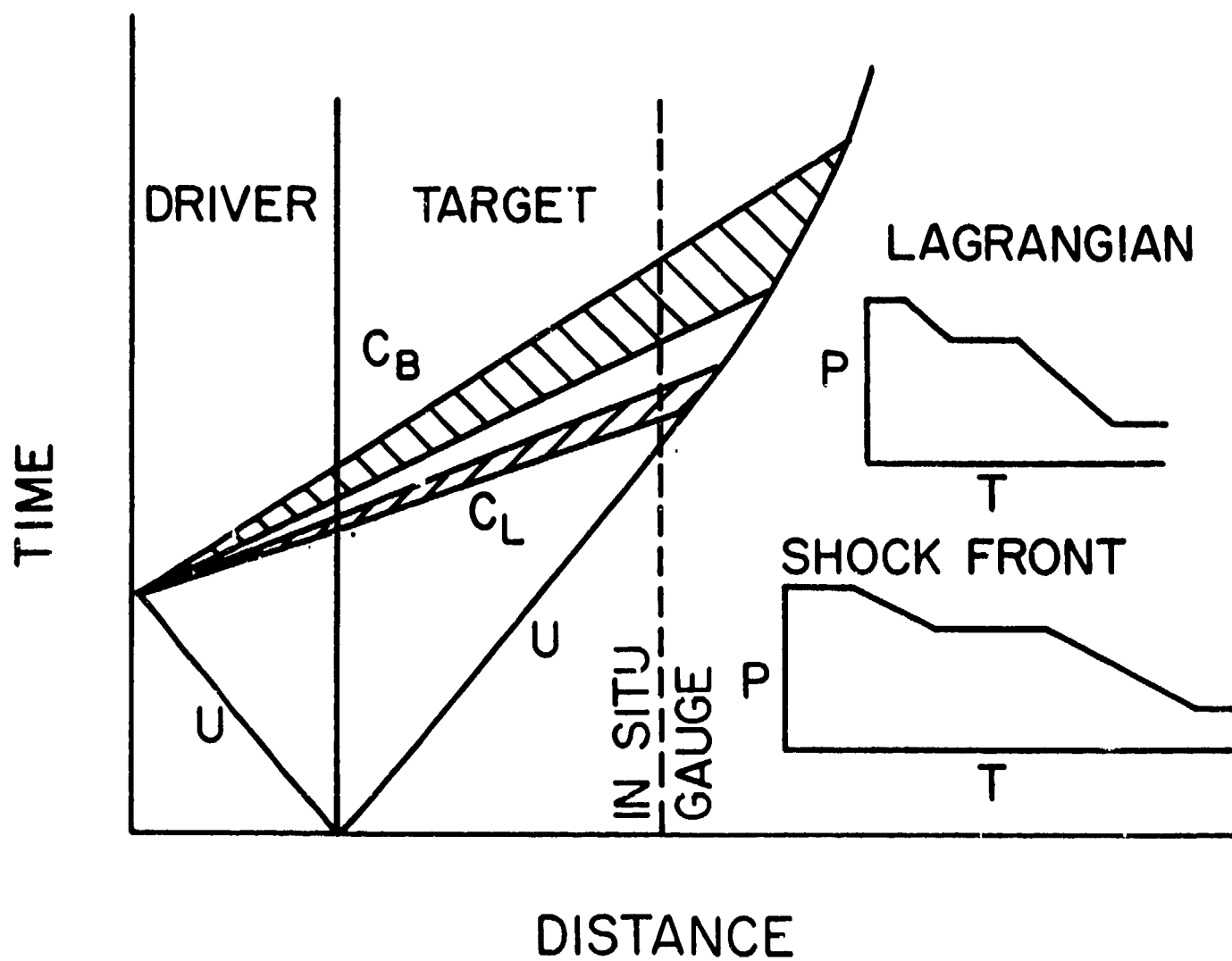
Figure V.28

347 STAINLESS STEEL

X = 6.0 mm   X = 9.6 mm
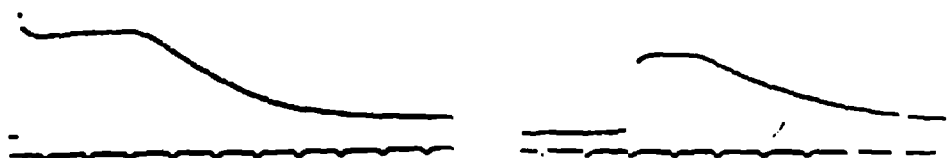
FUSED QUARTZ
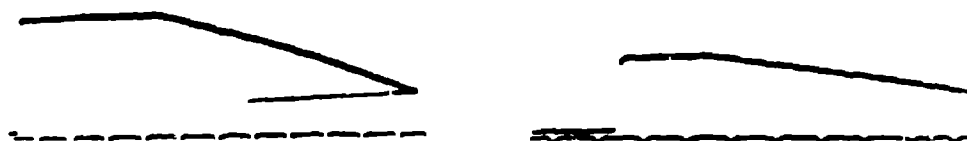
BROMOFORM
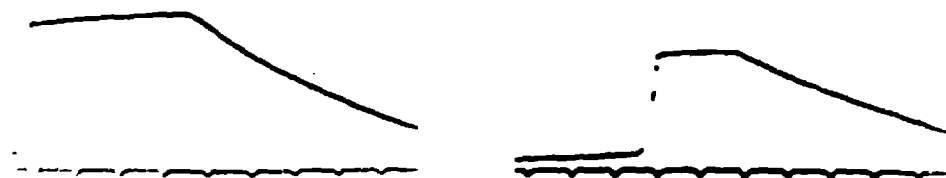
HIGH DENSITY GLASS

Figure V.29

LONGITUDINAL WAVE
CATCH UP 2024 AL
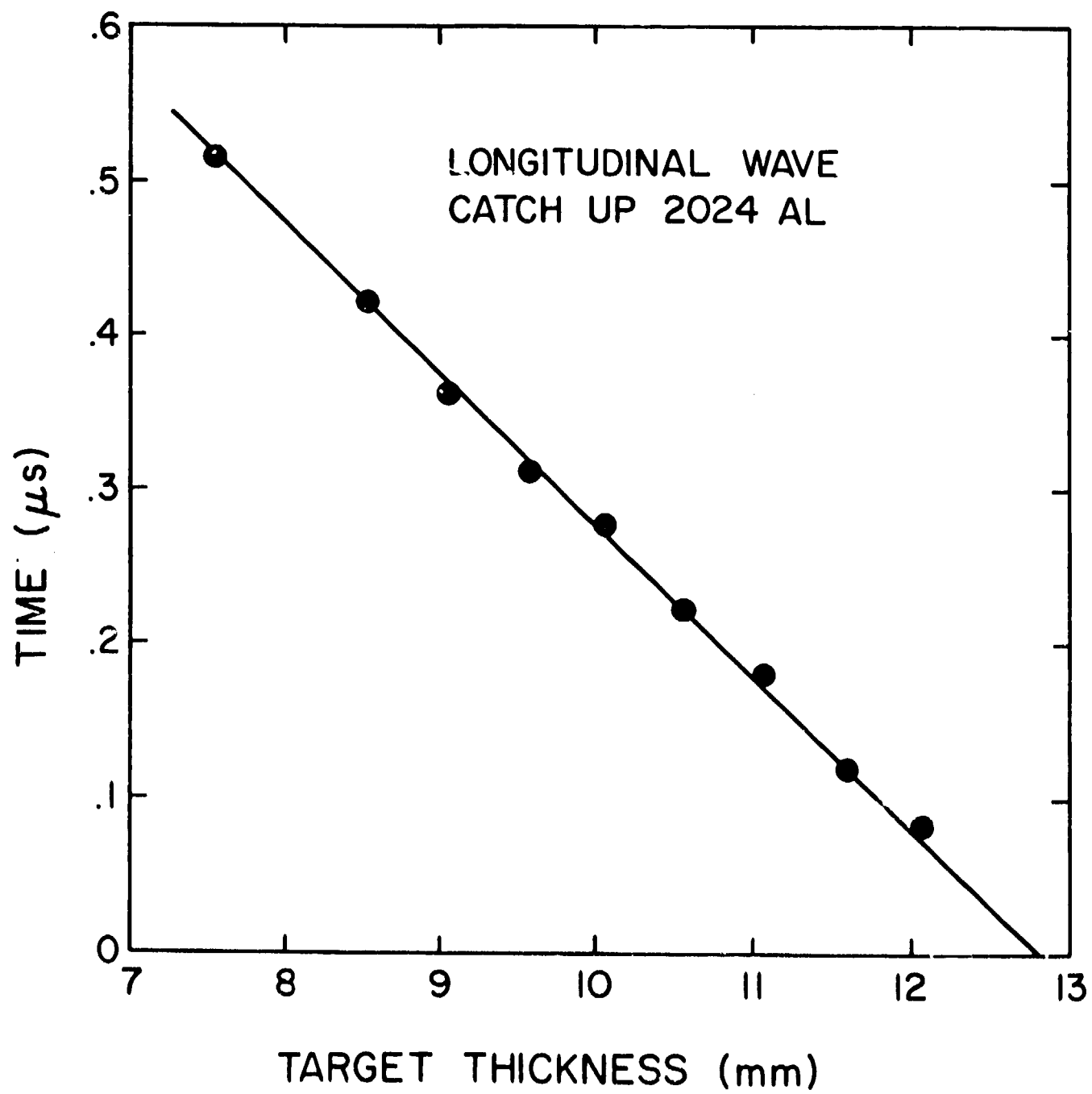
Figure V.30

Figure V.31

Figure V.32

LINE WAVE GENERATOR

DETONATOR

1/4" SHEET EXPLOSIVE

1/8" STAINLESS STEEL

6° 35'

COMPOSITION "B" EXPLOSIVE

4"

10"

3/8" IRON

WOOD BLOCK

1-5/8" RUN

SIDE SPALL RING

SPECIMEN

2"

FORWARD SPALL PLATES

1-1/4"

1-5/8" AIR

WOOD BLOCK

WATER

PLAN OF SPECIMEN AND SIDE SPALL RING

12"   6"
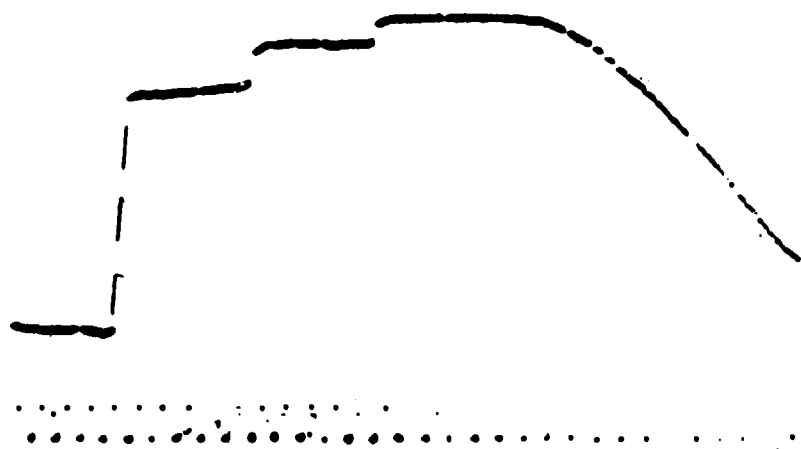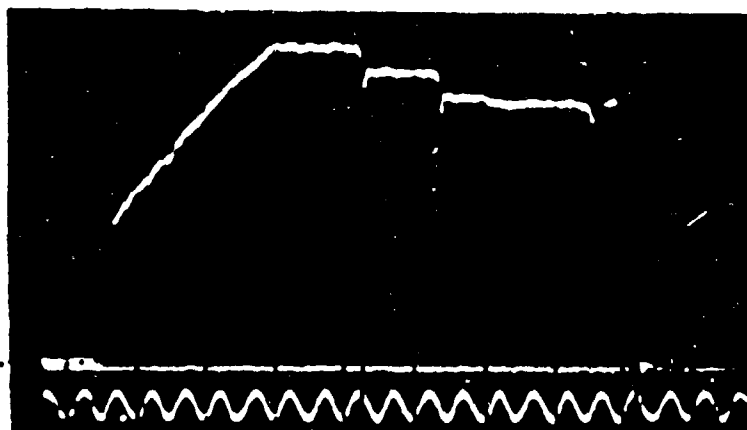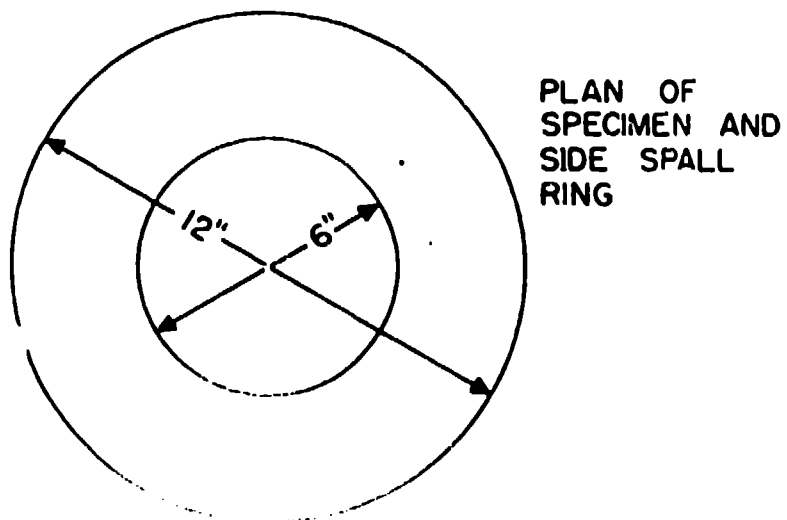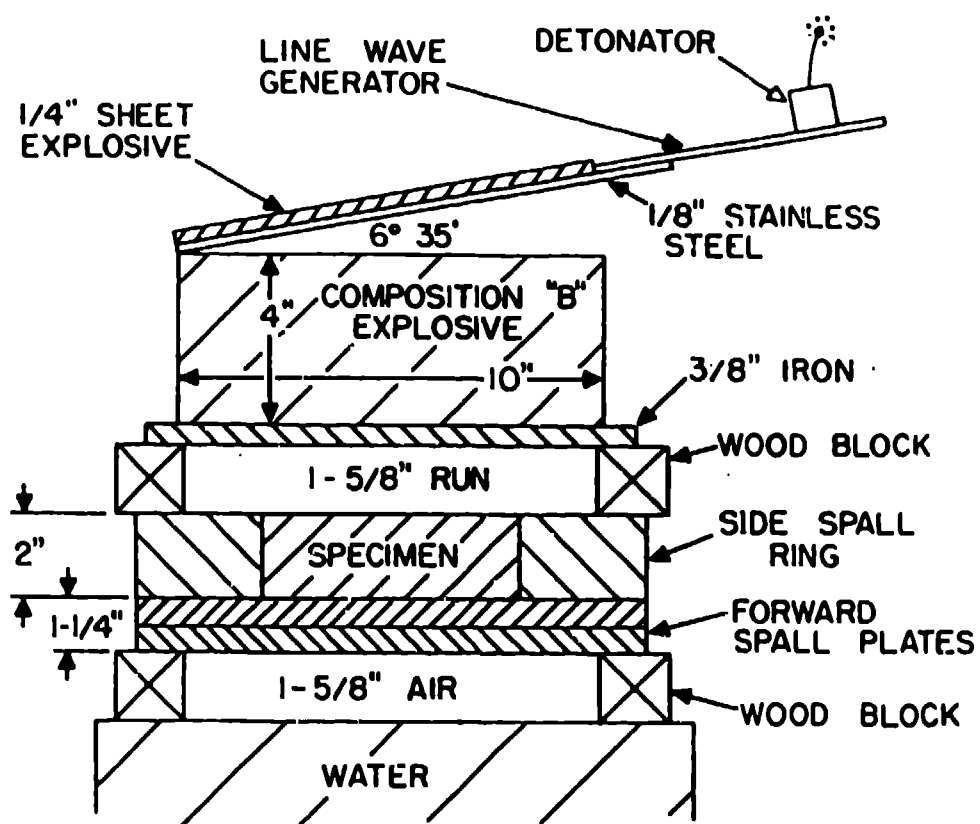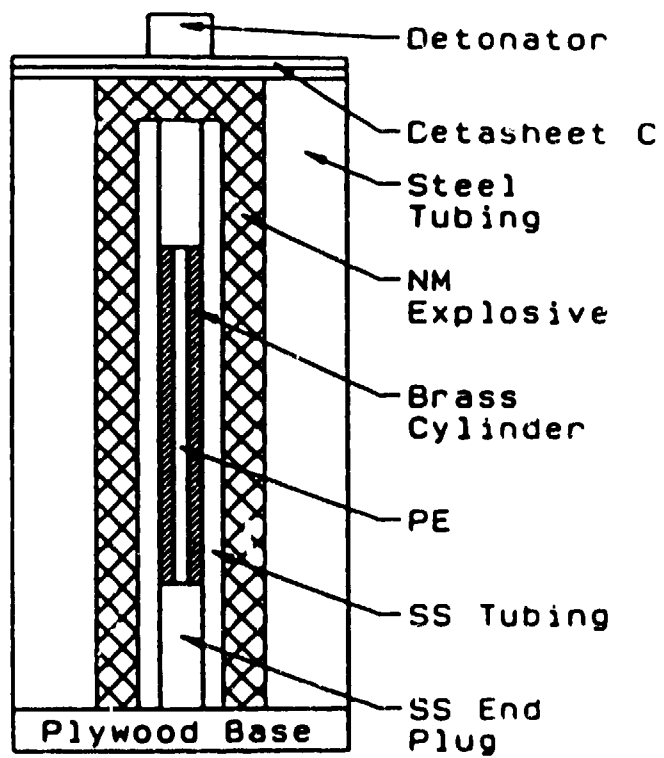
Figure V.33
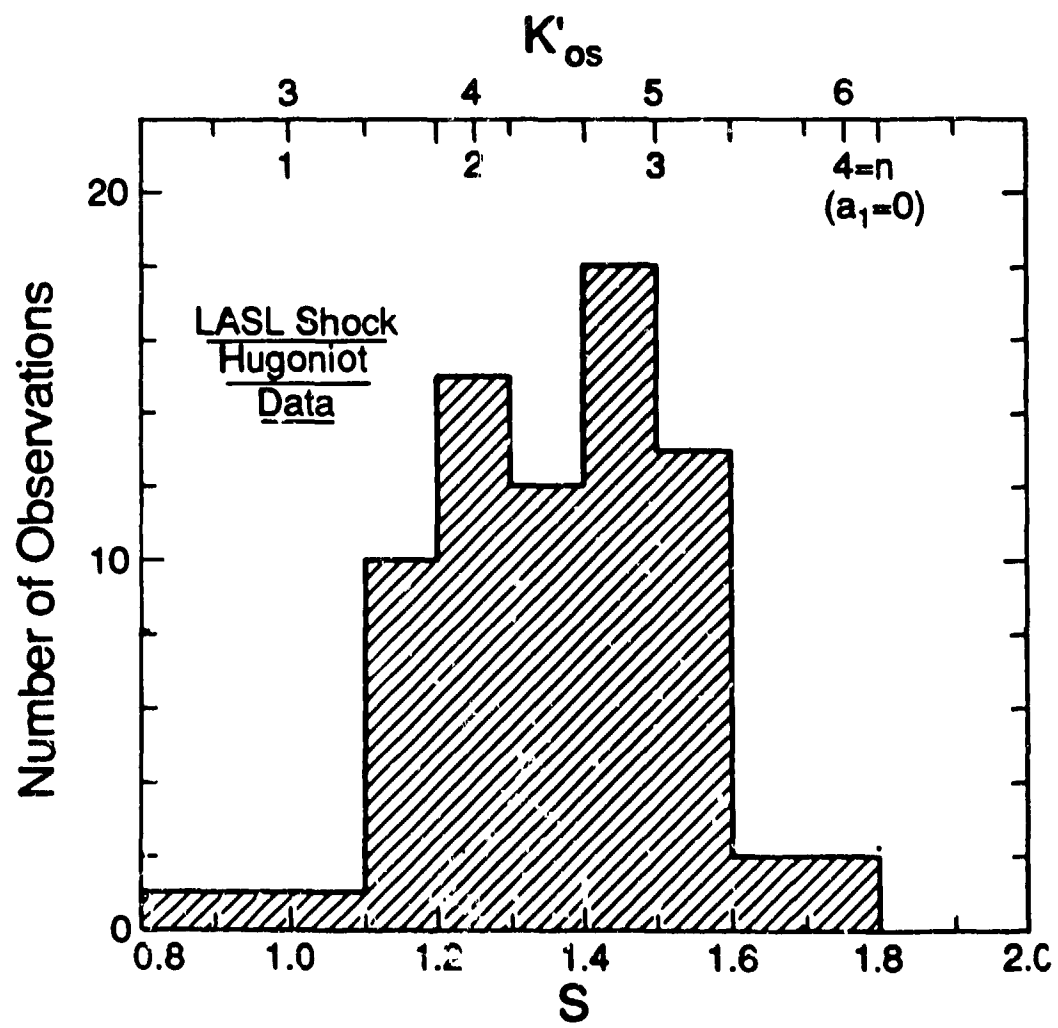
Figure V.34
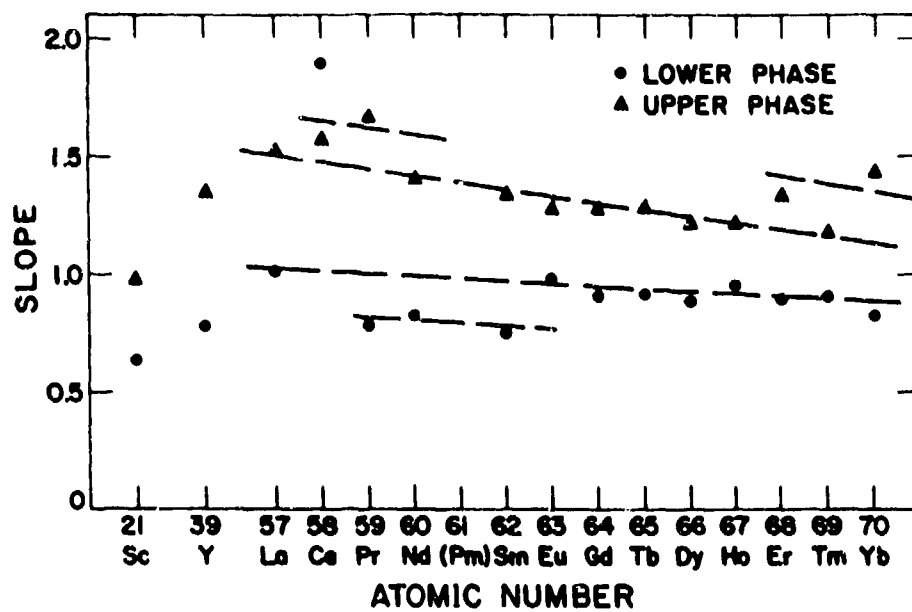
Figure VI.1

Figure VI.2
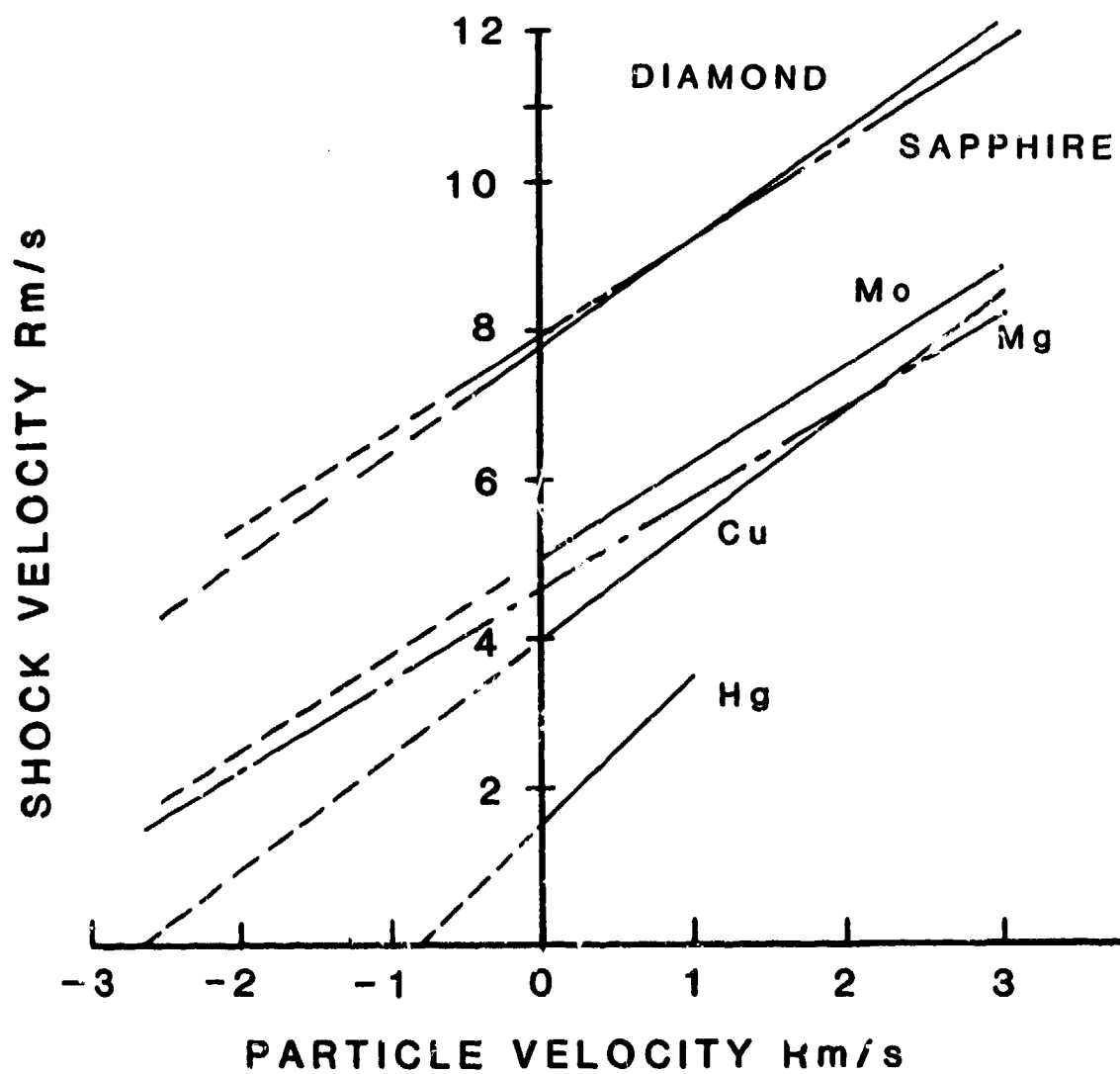
Figure VI.3
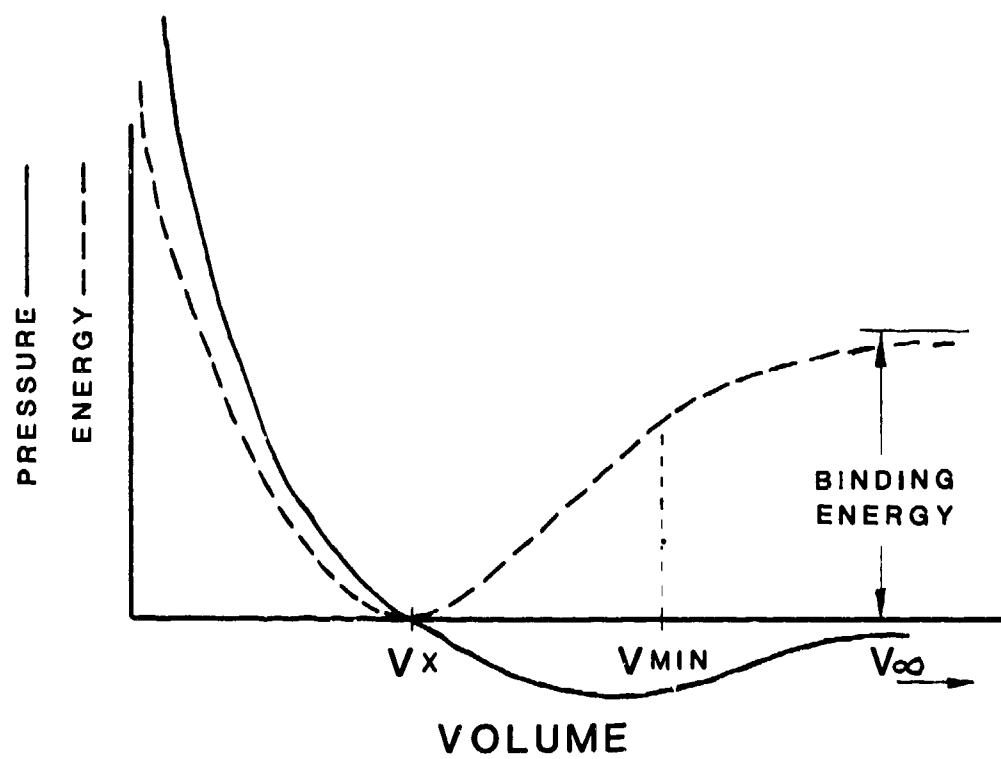
Figure VI.4

Figure VI.5

Figure VI.6

Figure VII.1
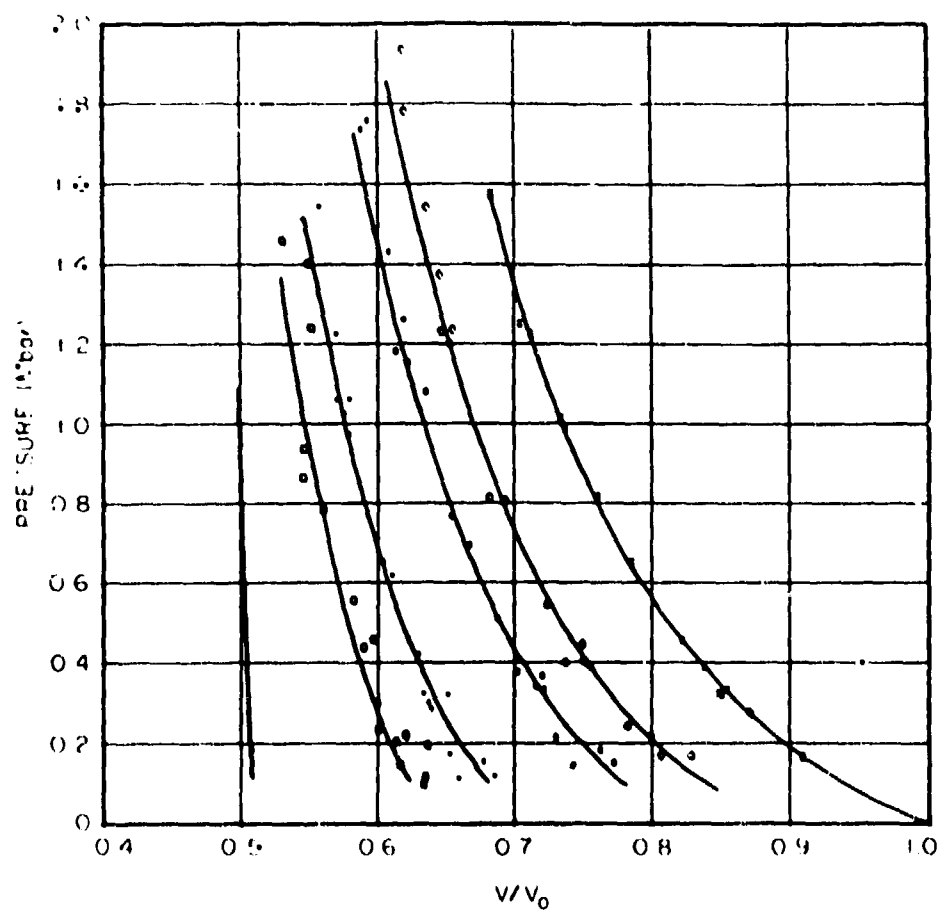
Figure VII.2
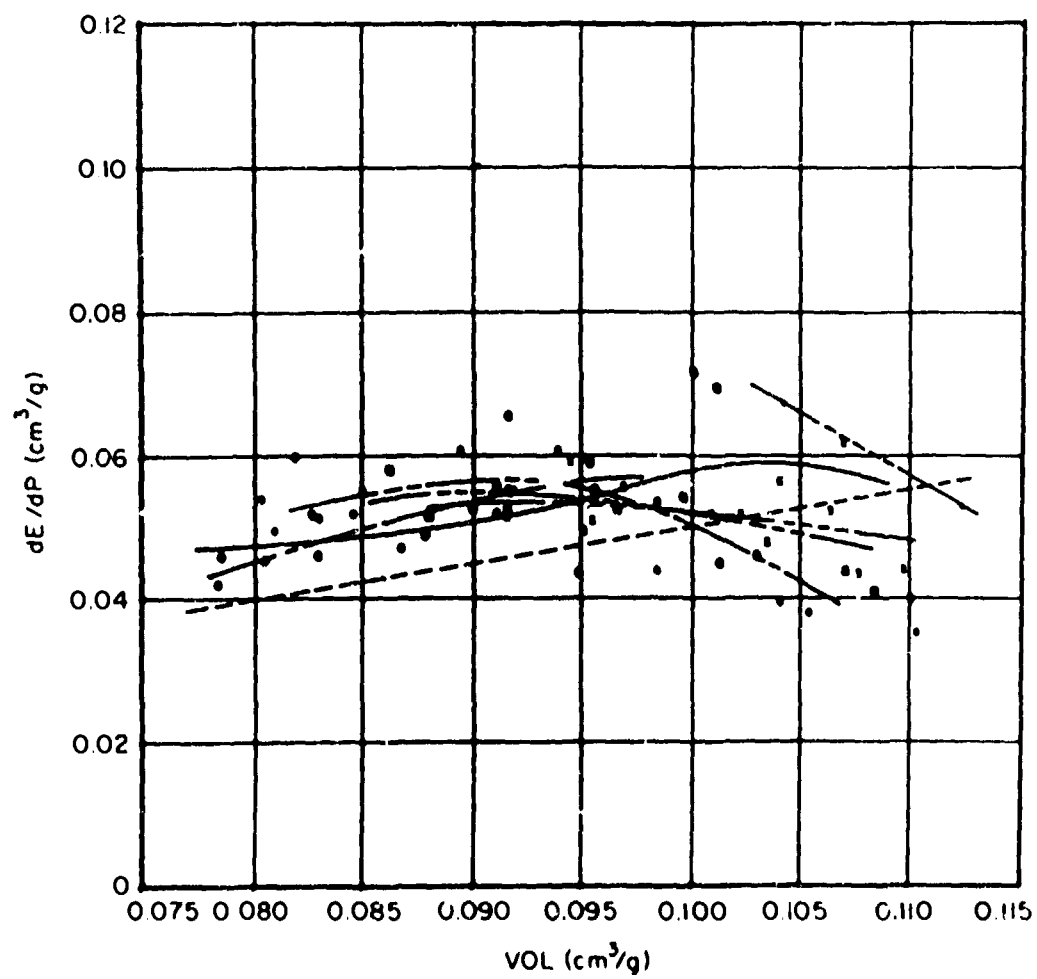
Figure VII.3
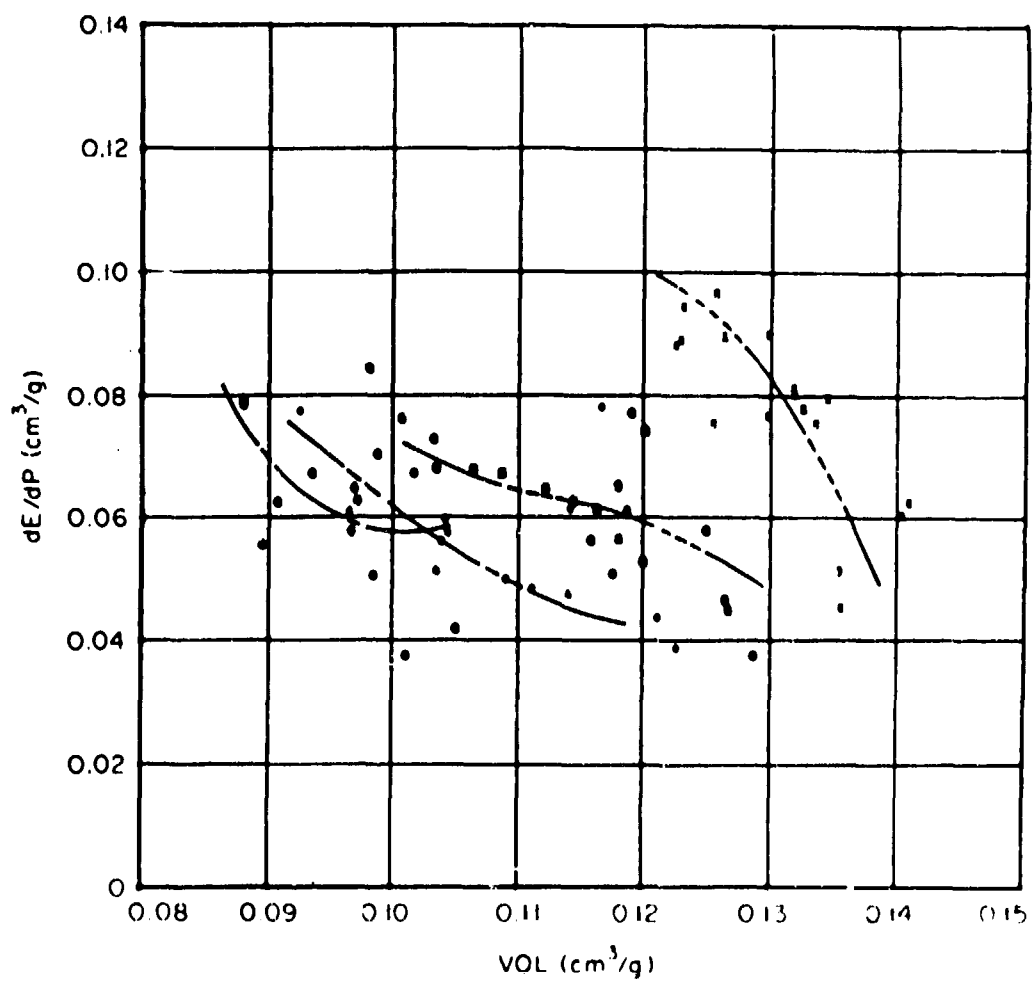
Figure VII.4
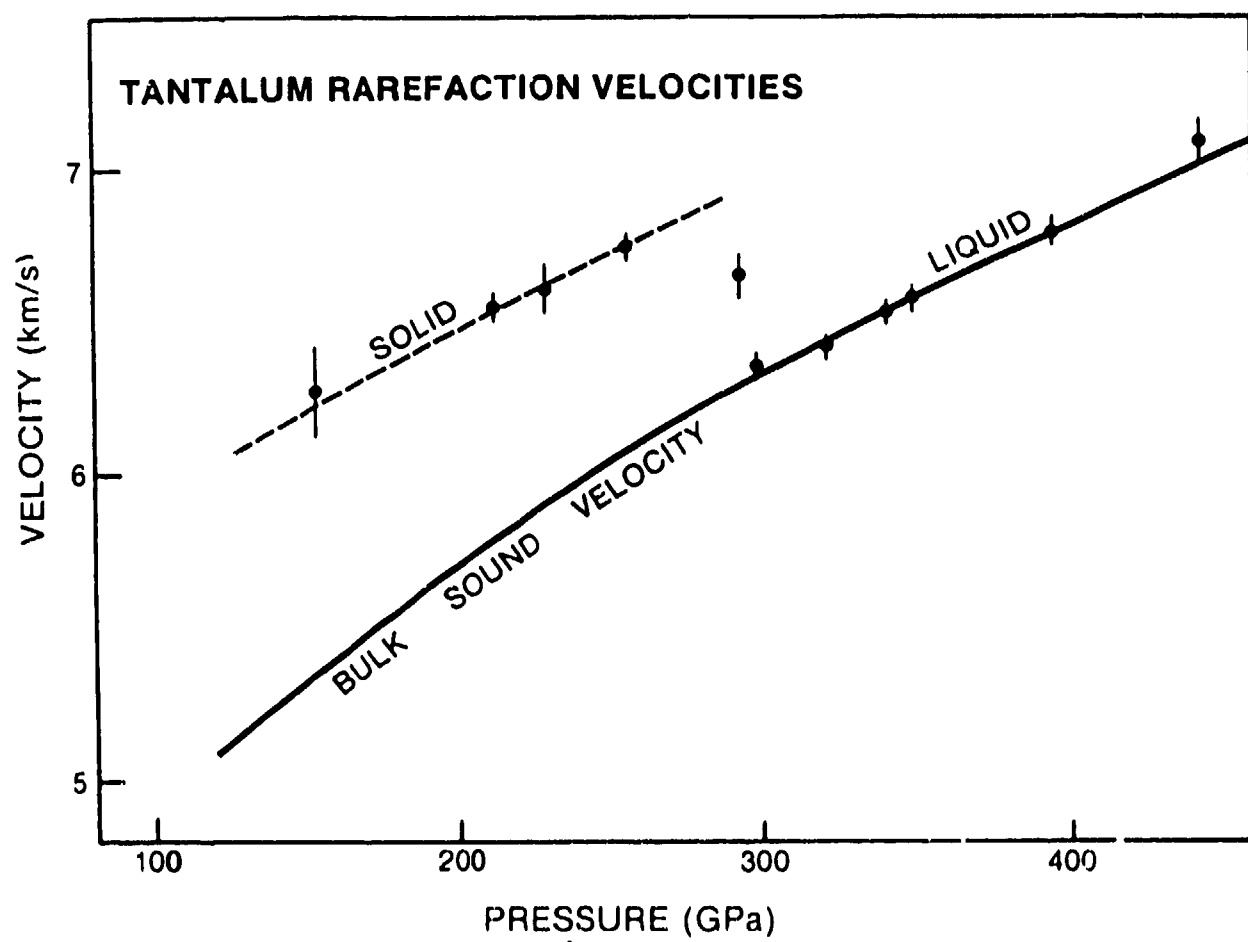
Figure VII.5
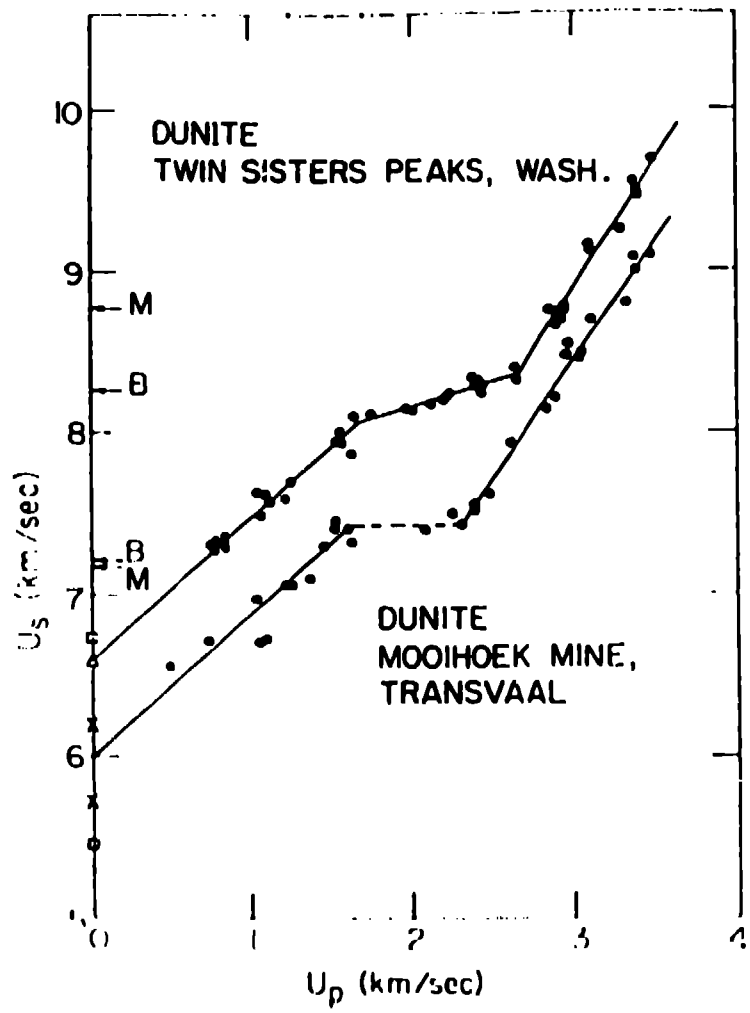
Figure VIII.1
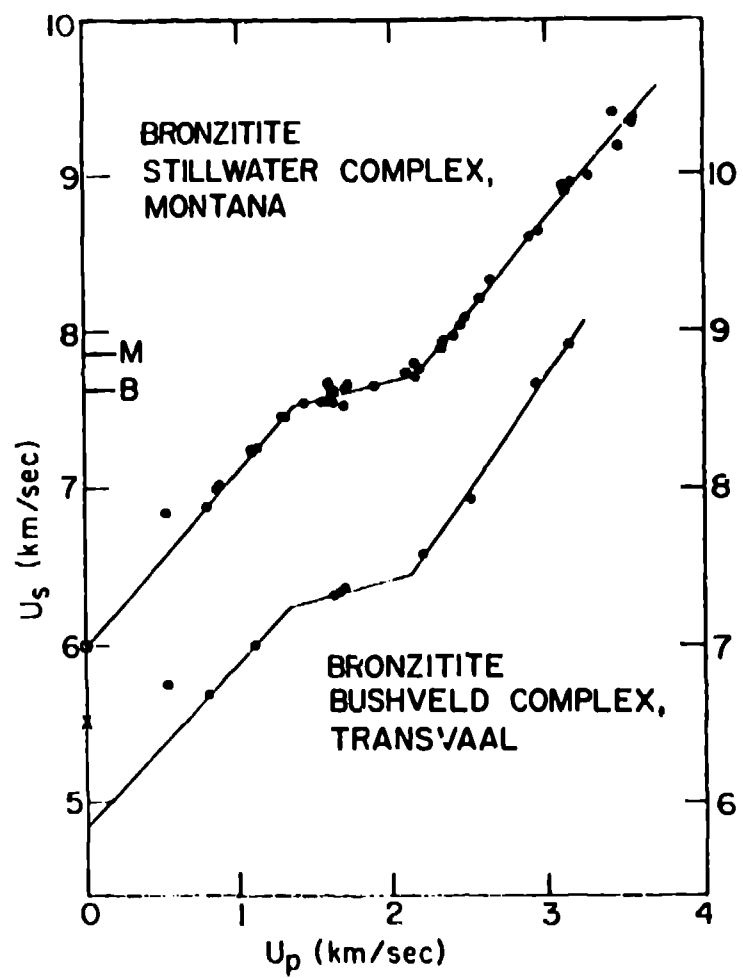
Figure VIII.2
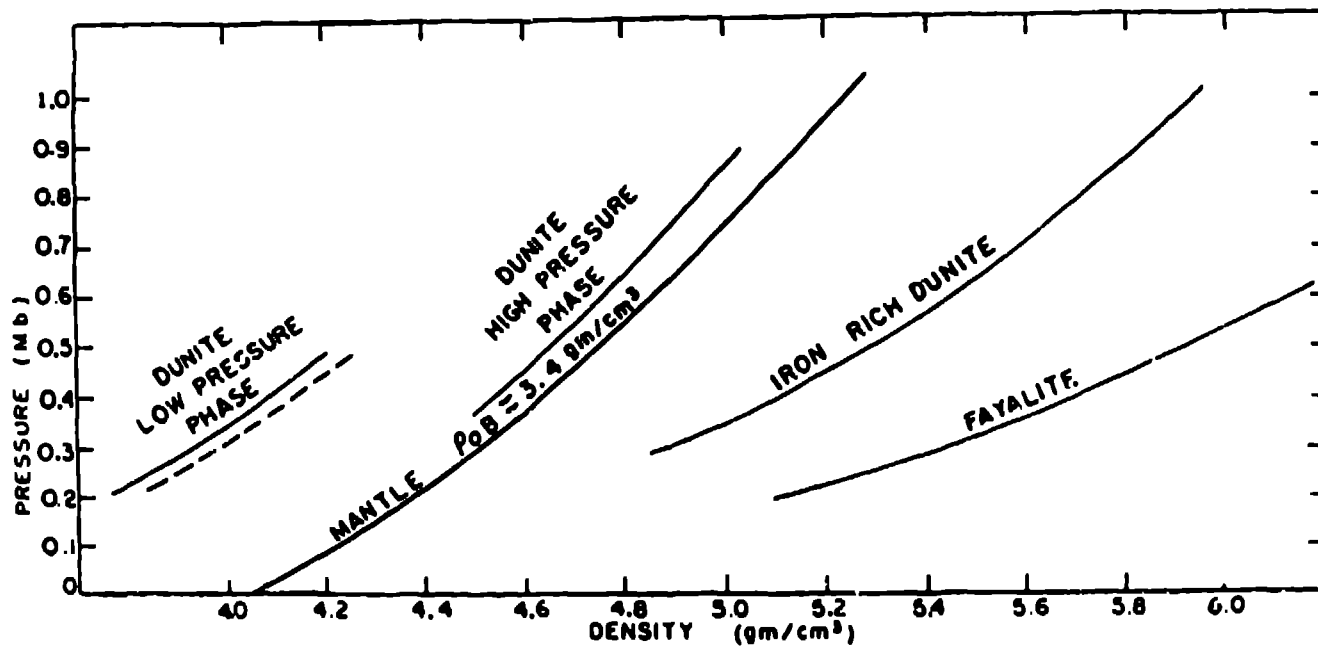
Figure VIII.3
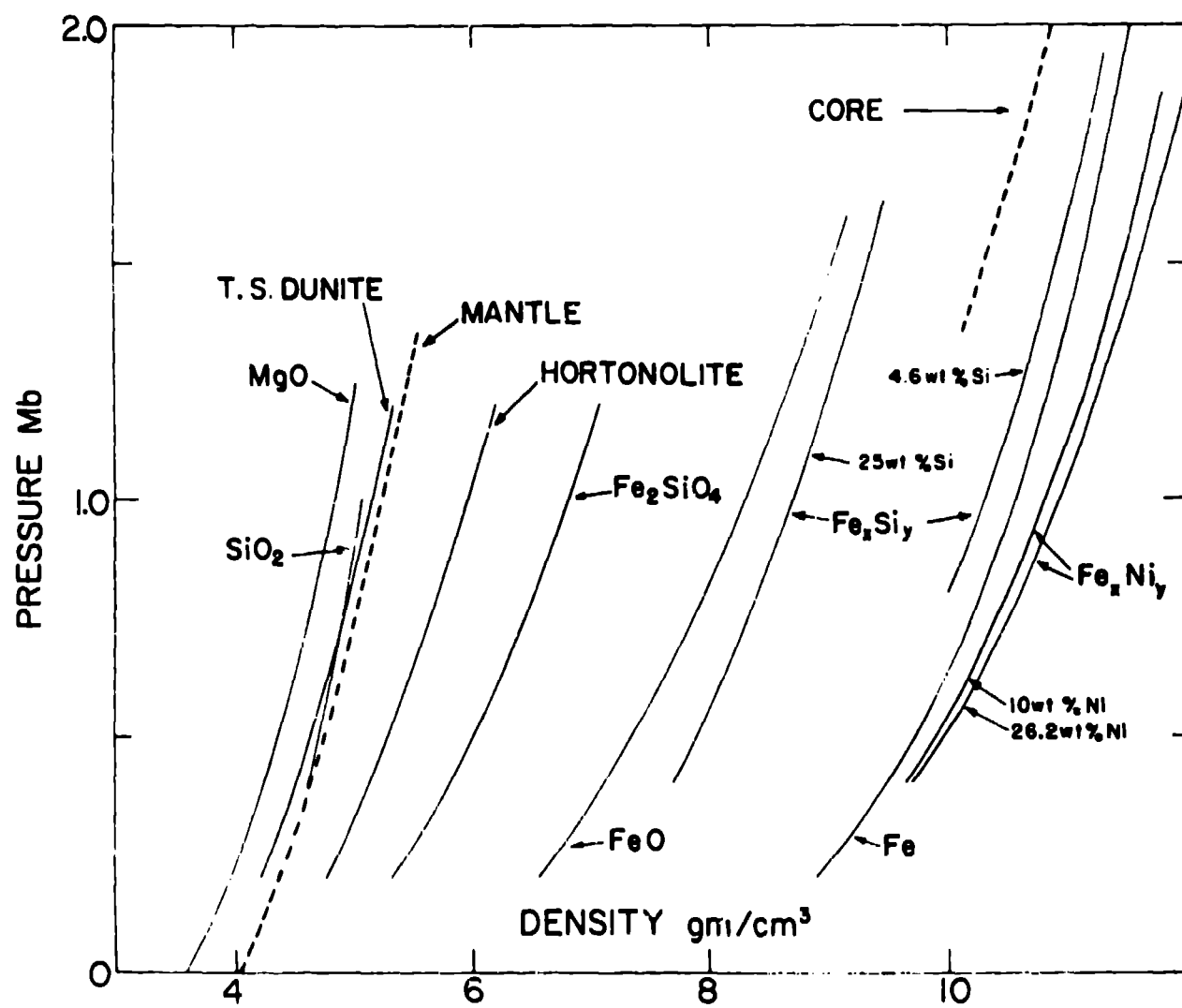
Figure VIII.4
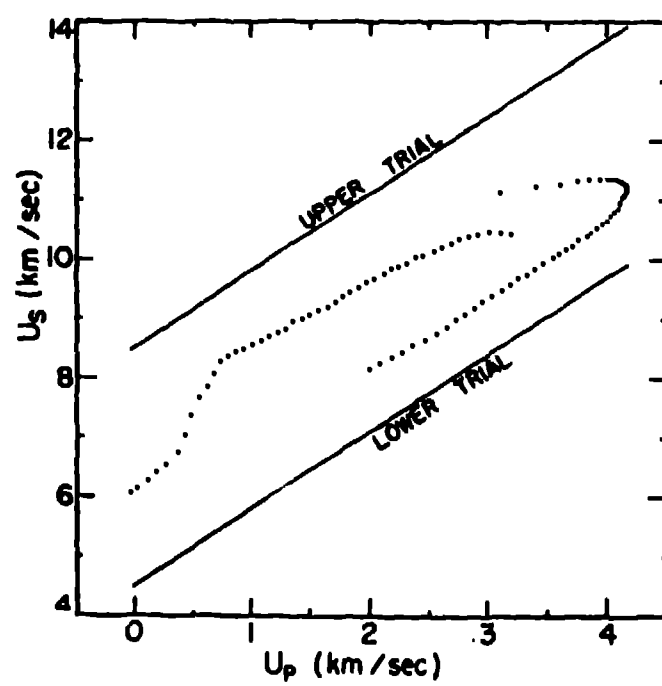
Figure VIII.5
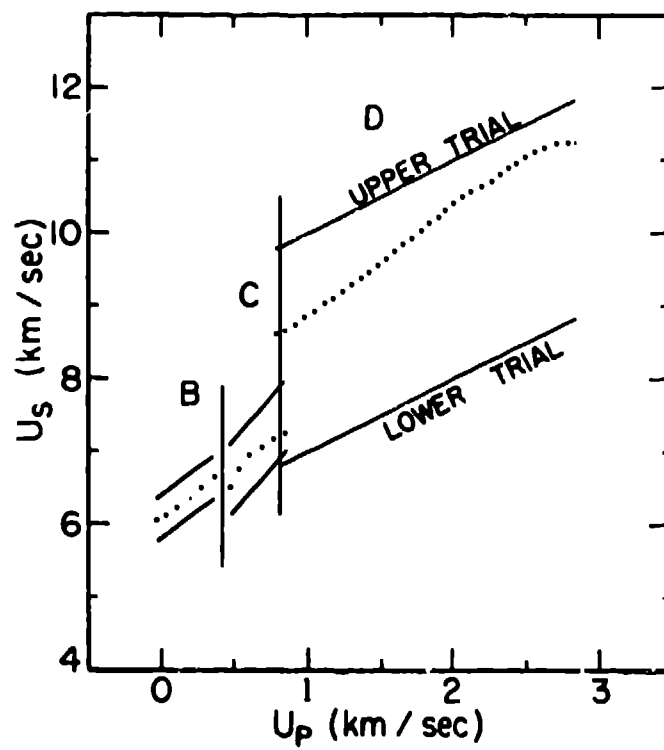
Figure VIII.6
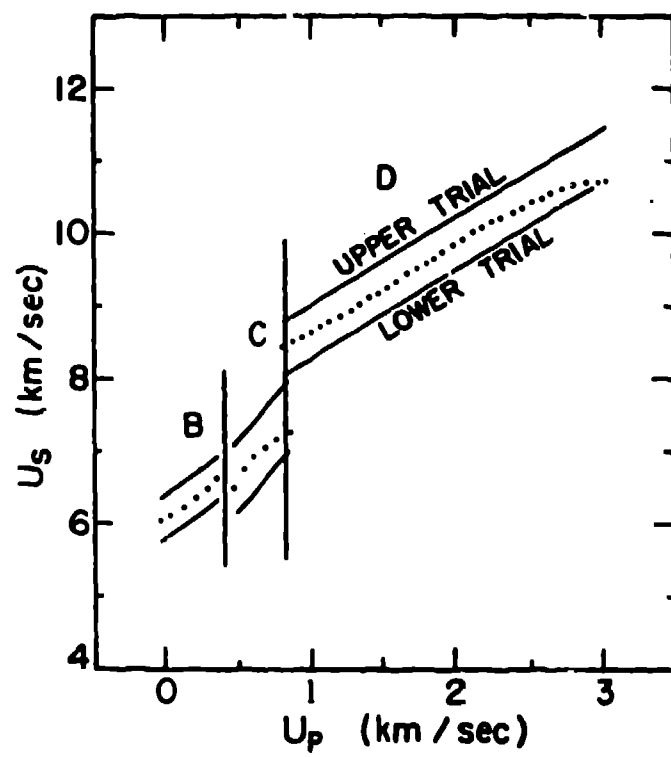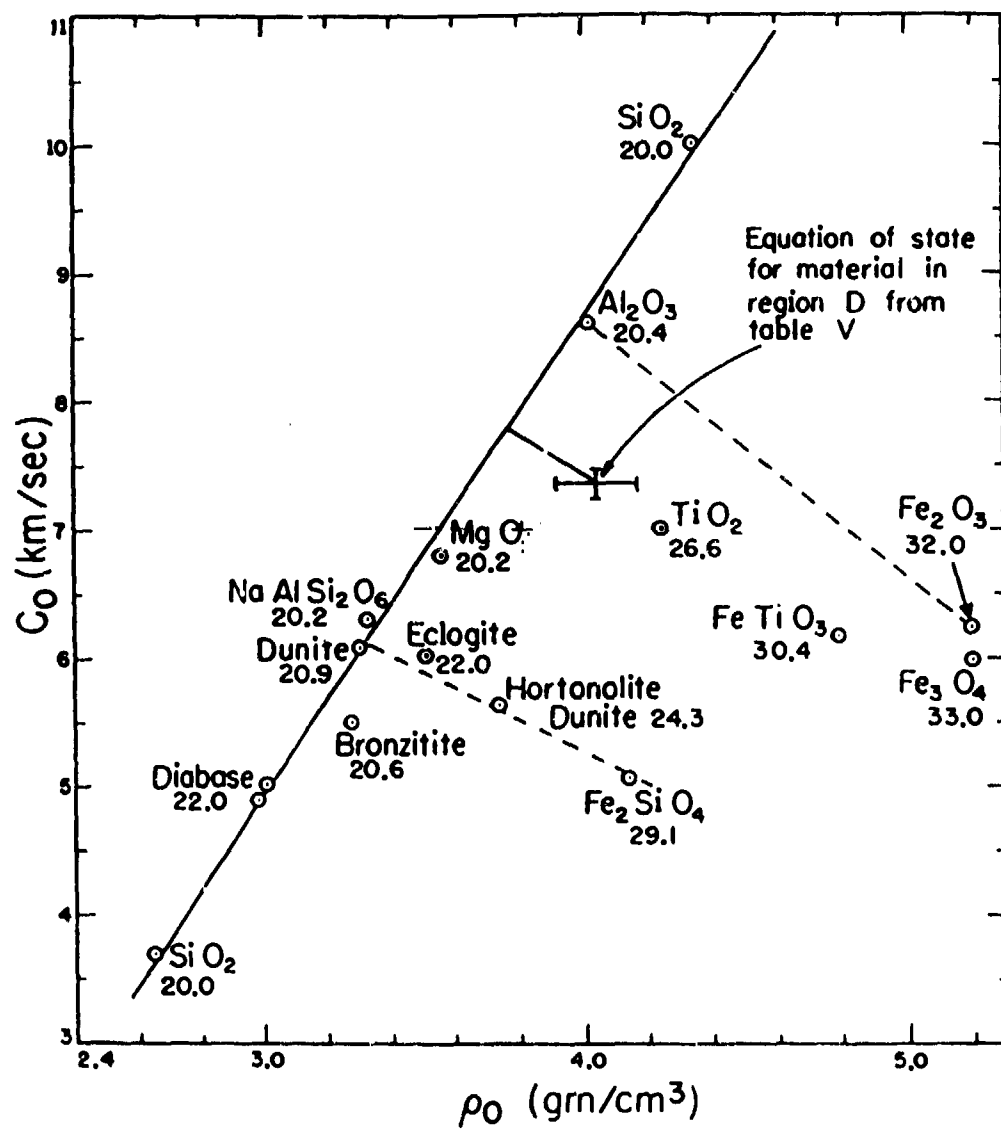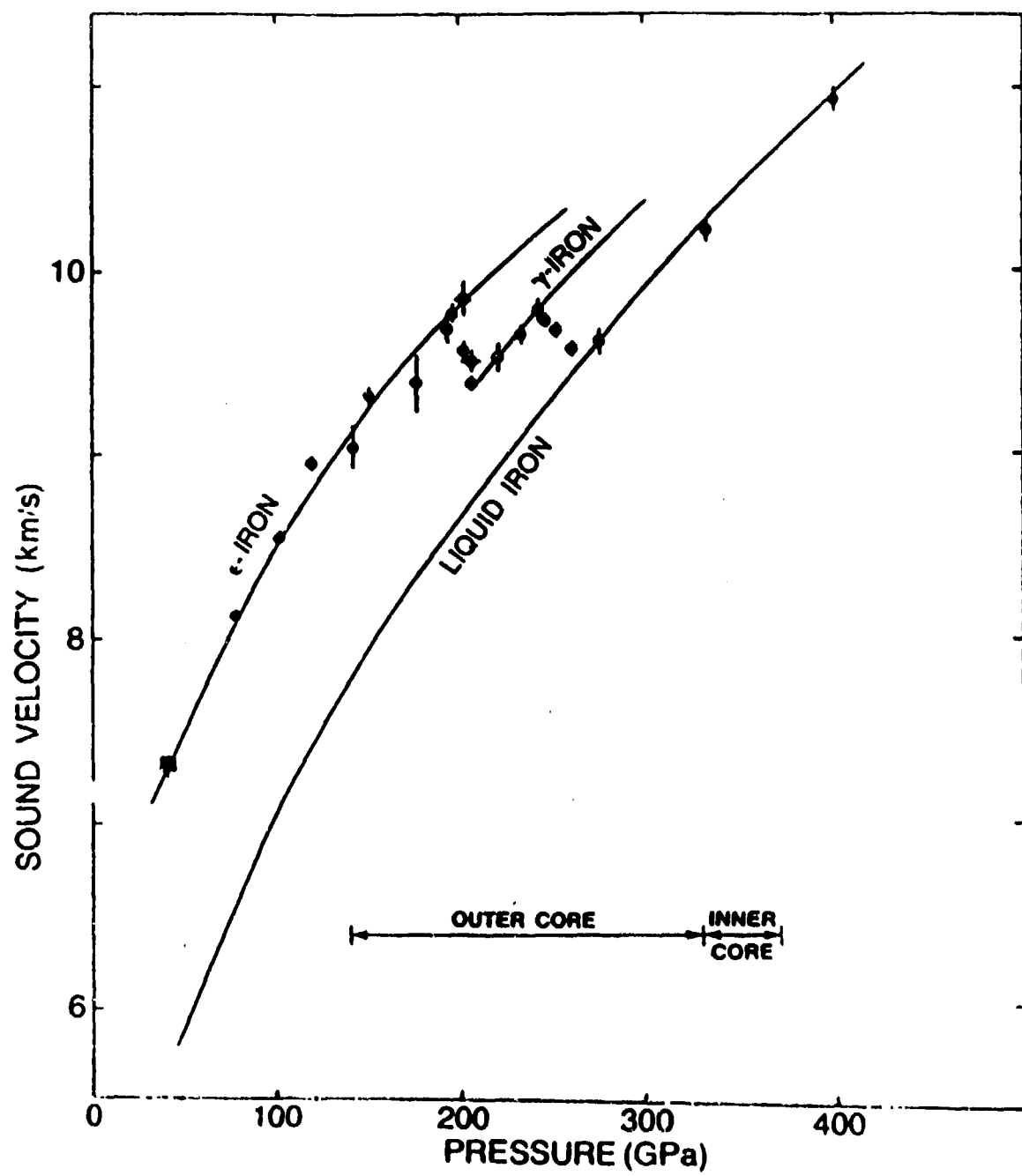
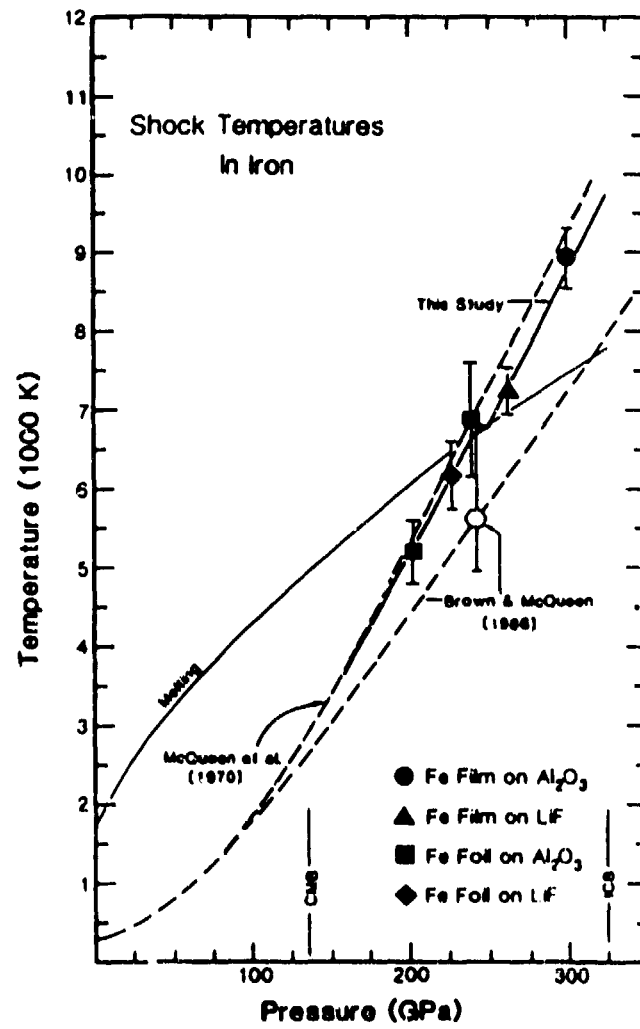Figure VIII.7
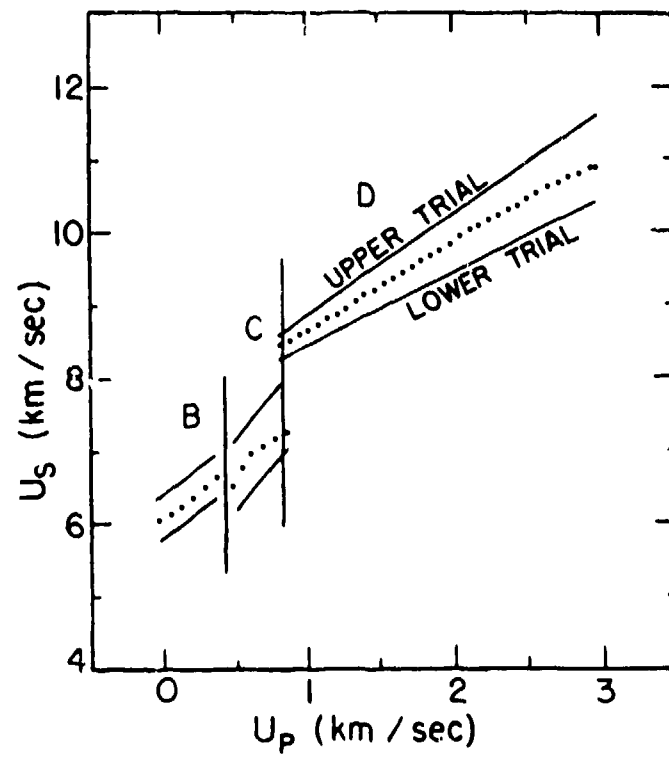
Figure VIII.8
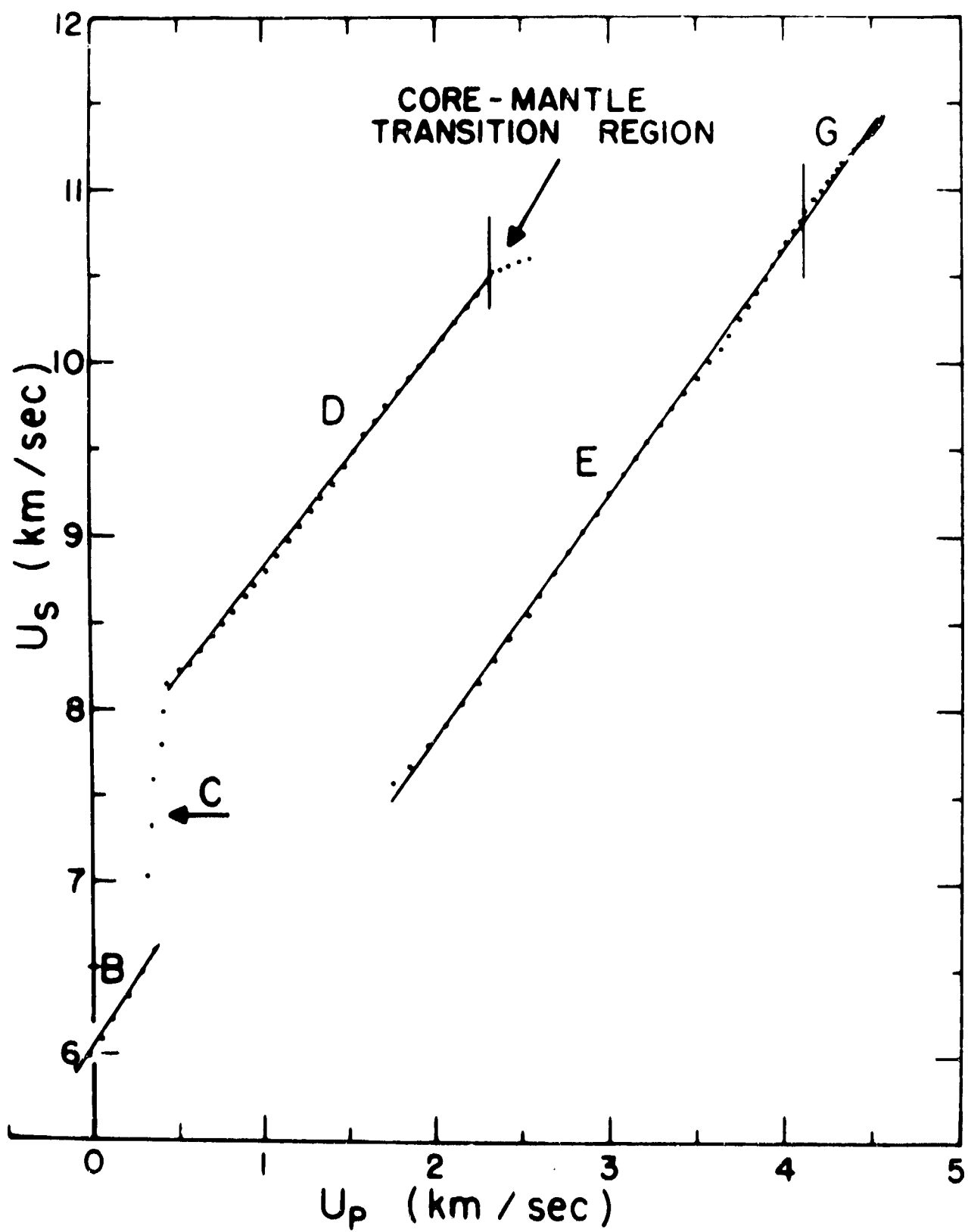
Figure VIII.9
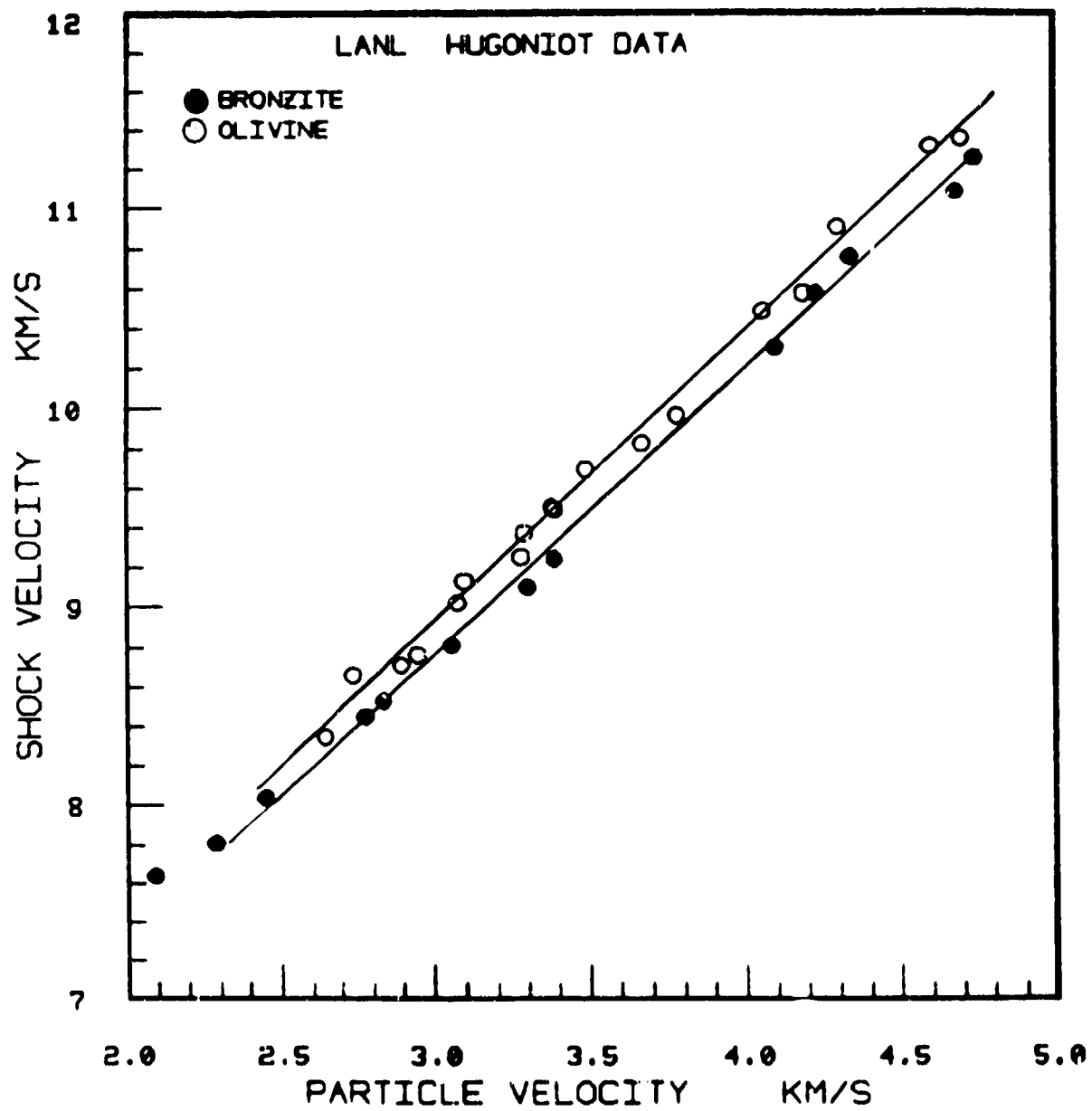
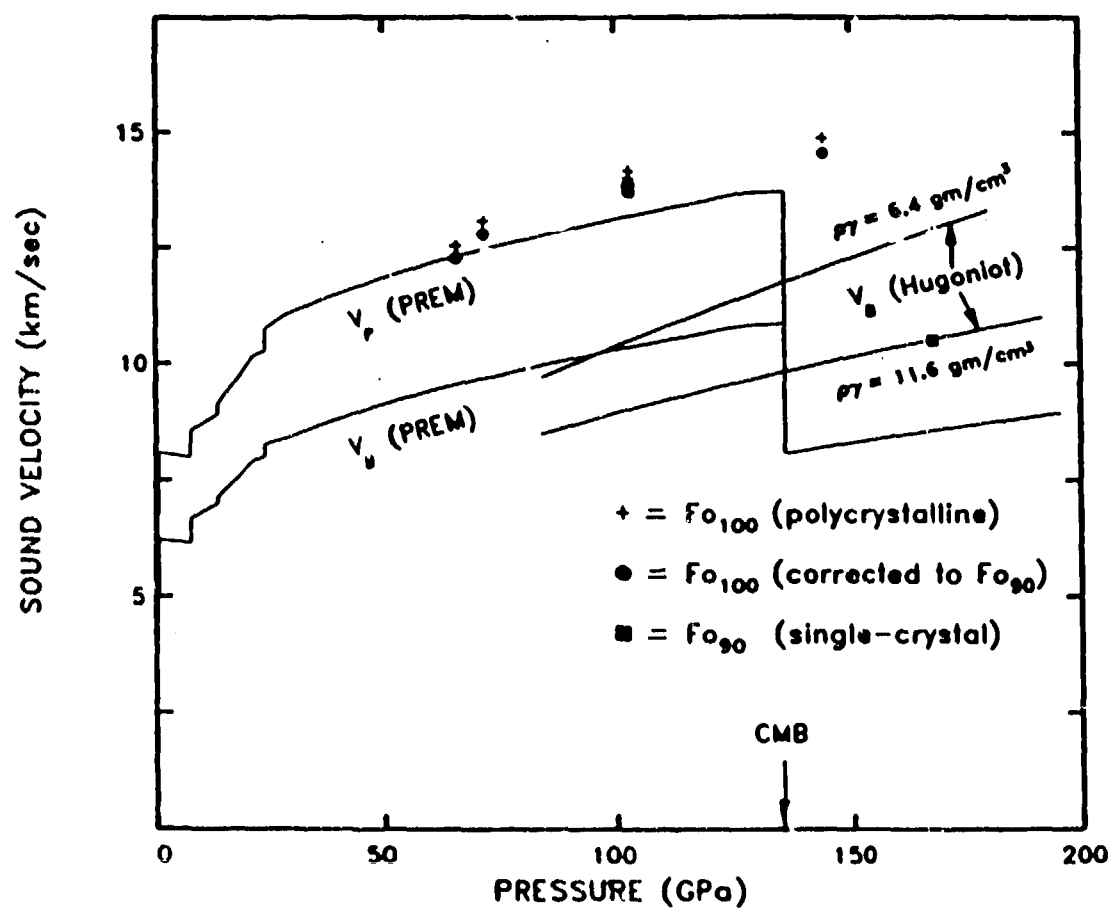Figure VIII.10

Figure VIII.11

Figure VIII.12

Figure VIII.13

Figure VIII.14